Politecnico di Torino

ScuDo
Scuola di Dottorato ~ Doctoral School
WHAT YOU ARE, TAKES YOU FAR

Doctoral Dissertation
Doctoral Program in Chemical Engineering (38^{th}cycle)

Multiscale Modelling of Complex Fluids

By

Francesco De Roma

******

Supervisor(s):
Prof. Antonio Buffo, Supervisor
Prof. Daniele Marchisio, Co-Supervisor

Doctoral Examination Committee:
Prof. Alexandra Komrakova, Referee, University of Alberta
Prof. Martin Lísal, Referee, Institute of Chemical Process Fundamentals

Politecnico di Torino
2026

Declaration

I hereby declare that, the contents and organization of this dissertation constitute my own original work and does not compromise in any way the rights of third parties, including those relating to the security of personal data.

Francesco De Roma
2026

* This dissertation is presented in partial fulfillment of the requirements for **Ph.D. degree** in the Graduate School of Politecnico di Torino (ScuDo).

I would like to dedicate this thesis to my family, for their love and support.

Abstract

This thesis develops and assesses a multiscale strategy to predict the flow of complex fluids in mixing equipment by linking microstructure-dependent rheology to process-scale performance. The framework combines Dissipative Particle Dynamics (DPD) as a microscale computational rheometer, Computational Fluid Dynamics (CFD) as the equipment-scale solver, and Gaussian Process Regression (GPR) as a surrogate layer between scales. An automated coupling loop is proposed in which an initial CFD solution identifies the rate-of-strain window explored in the device. DPD simulations are then selected adaptively, and the GPR viscosity model is refined by launching new microscale simulations only where the surrogate predictive uncertainty is highest, until a prescribed uncertainty threshold is reached.

The workflow is demonstrated on an industrial surfactant blend, Miraspec UB75, flowing through a Sulzer SMX static mixer. A DPD model for SLES/water is adopted from the literature and extended to include CMEA through a parameterisation based on water–octanol partition coefficients. The model qualitatively reproduces microstructures consistent with reported SLES/water phase behaviour, including micellar, hexagonal, and lamellar regions, and predicts a lamellar morphology for the UB75 formulation. Non-equilibrium DPD rheometry is used to obtain a shear-thinning viscosity curve, which is then used to train a GPR model embedded in OpenFOAM. This enables process-scale predictions over heterogeneous strain-rate fields and gives realistic pressure-drop levels when compared with similar blends in the same type of mixing device.

To address the poor signal-to-noise ratio of standard non-equilibrium DPD rheometry at low imposed shear rates, the thesis adapts the Transient Time Correlation Function (TTCF) formalism to DPD. It is shown that standard TTCF mappings are not compatible with DPD, because dissipative and random forces break the symmetry required to enforce zero initial dissipation. A covariance-corrected TTCF expression,

combined with bootstrap-based uncertainty estimation, provides a practical workflow for DPD without mappings. For the simple DPD fluid investigated here, this approach enables viscosity estimation down to very low shear rates without loss of precision as the shear rate decreases, unlike direct averaging.

Finally, CFD models of unbaffled stirred tanks operating with Newtonian and non-Newtonian Pluronic L64/water mixtures are developed and compared with power-consumption and PIV measurements. A steady laminar Multiple Reference Frame workflow reproduces power-number trends and the main flow structures well at low and intermediate Reynolds numbers, while deviations at higher Reynolds numbers highlight transitional effects and the limits of laminar modelling. A composition-dependent GPR viscosity model is also coupled to CFD for transient mixing simulations. This demonstrates the feasibility of producing spatially varying viscosity fields driven by local composition and shear rate, while revealing the additional challenge of locally changing flow regimes as composition evolves.

Contents

List of Figures

List of Tables

Nomenclature

Italic Symbols – Scalars

α	Power index in the Bird–Carreau model
Δt	Computational timestep
$\dot{\gamma}_{\mathrm{DPD}}$	Shear rate imposed to DPD simulations in the coupled approach
ϵ	Average viscous energy dissipation rate
ϵ_{lim}	Maximum acceptable relative difference for the shear rate convergence criterion
$\epsilon_{\mathrm{max,\,rel}}$	Relative difference for the maximum shear rate convergence criterion
$\epsilon_{\mathrm{min,\,rel}}$	Relative difference for the minimum shear rate convergence criterion
η	Non-Newtonian dynamic viscosity
γ	DPD dissipative force parameter
Λ	Velocity predictor blending parameter for the modified velocity-Verlet algorithm
λ	Time constant in the Bird–Carreau model
$\mathcal{D}$	Binary diffusion coefficient
$\mathcal{E}$	Thermal energy scale
μ	Newtonian dynamic viscosity
μ_0	Zero-shear dynamic viscosity

μ_∞	Infinite-shear dynamic viscosity
μ_{app}	Apparent dynamic viscosity for a fixed shear rate
ν	Kinematic viscosity
Ω	Dissipation function
ω	Rotational speed
ρ	Density
ρ^*	Lennard–Jones reduced density
ρ_{DPD}	DPD bead number density
σ	DPD random force parameter
σ_f^2	Signal variance for the RBF kernel
σ^{gpr}	Standard deviation for the GPR coupling
$\sigma_{\text{lim}}^{\text{gpr}}$	Maximum acceptable standard deviation for the GPR-DPD coupling
σ_{LJ}	Lennard–Jones zero potential distance
θ	Angle between two adjacent bonds
θ_0	Equilibrium angle between two adjacent bonds
ε	Lennard–Jones potential well depth
ε_{r}	Relative dielectric constant
ξ_{ij}	DPD random number
ζ	Decay length for the electrostatic interaction potential
A_i	Surface of the i-th face of a computational cell
a_{ij}	DPD conservative force parameter
B	Generic phase variable
b	Electrostatic interaction potential constant

B_d Depth of the elliptical bottom of the stirred tank

C Concentration of a species (Chapter 2)

C Pluronic L64 concentration (Chapter 5)

C_d Clearance between the impeller and the end of the cylindrical part of the stirred tank

$c_{k,i}$ i component of the peculiar velocity of bead k

D Diameter of SMX static mixer (Chapter 3)

D Impeller diameter (Chapter 5)

E_{angle} Angle interaction potential

E_{bond} Bonded interaction potential

E_{el} Electrostatic interaction potential

$f_{ij,\beta}$ Force component along the β direction between the i-th and the j-th DPD beads

H Height of the cylindrical part of the stirred tank

K Metzner–Otto constant

k Consistency index in the power-law model

k_{angle} Constant for angle potential

$k_{B,DPD}$ Boltzmann constant for DPD simulations

k_{bond} Spring constant for bond harmonic potential

k_B Boltzmann constant

L Length of the side of a DPD simulation box

l Characteristic length-scale for the RBF kernel

L_{fz} Length of the inlet section of the CFD domain for the static mixer

L_i Length of the section containing the mixing elements

L_t	Total tube length of the CFD domain for the static mixer
m_i	Mass of the i-th DPD bead
M_z	Moment acting on the impeller in the axial direction
N	Number of particles in an MD or DPD simulation
n	Flow behaviour index in the power-law model
N_b	Number of bars per mixing element in the static mixer
N_e	Number of mixing elements in the static mixer
N_r	Impeller speed in revolutions per second
P	Power drawn at the impeller
p	Pressure
$P_{\alpha\beta}$	Element of the pressure tensor, where α and β refer to the Cartesian components
$p_{x,i}$	x-component of the momentum of the i-th DPD bead
P_{xy}	Shear component of the pressure tensor
$p_{y,i}$	y-component of the momentum of the i-th DPD bead
P_{yx}	Shear component of the pressure tensor
$p_{z,i}$	z-component of the momentum of the i-th DPD bead
q_i	Charge of the i-th bead
r_0	Equilibrium distance for bond harmonic potential
r_c	Cutoff radius for DPD interactions
$r_\mathrm{c,el}$	Cutoff radius for electrostatic interaction treatment
r_{ij}	Distance between two DPD beads
T	Temperature

T^* Lennard–Jones reduced temperature

T_{DPD} Temperature in DPD reduced units

T_{d} Stirred tank diameter

V Volume of the system

v_{tip} Impeller's tip velocity

$v_{i,\alpha}$ velocity component along the α direction of the i-th DPD bead

$v_{x|y|z}$ Velocity components in the Cartesian directions

w_{ij}^{D} DPD dissipative force weight function

w_{ij}^{R} DPD random force weight function

Bold Lowercase Roman Symbols – Vectors

$\dot{\mathbf{p}}_i$ Time derivative of the momentum for a DPD bead

$\dot{\mathbf{r}}_i$ Time derivative of the position vector for a DPD bead

$\hat{\mathbf{n}}_i$ Normal unit vector of the i-th face of a computational cell

$\hat{\mathbf{r}}_{ij}$ Unit vector for the relative position between two DPD beads

$\mathbf{c}_k$ Peculiar velocity of bead k

$\mathbf{f}_{ij}^{C}$ DPD conservative force

$\mathbf{f}_{ij}^{D}$ DPD dissipative force

$\mathbf{f}_{ij}^{R}$ DPD random force

$\mathbf{f}_i$ Total force acting on a DPD bead

$\mathbf{p}_i$ Momentum of a DPD bead

$\mathbf{r}_i$ Position vector for a DPD bead

$\mathbf{r}_{ij}$ Relative position vector between two DPD beads

$\mathbf{s}$ Axis of rotation

$\mathbf{u}_k$ Streaming velocity of bead k

$\mathbf{v}$ Velocity vector in a continuum fluid

$\mathbf{v}_\mathrm{r}$ Velocity relative to the axis of rotation

$\mathbf{v}_i$ Velocity vector for a DPD bead

$\mathbf{v}_{ij}$ Relative velocity vector between two DPD beads

$\mathbf{w}$ Vector of rotation

Bold Italic Uppercase Roman Symbols – Tensors

$\boldsymbol{P}$ Pressure tensor

Bold Italic Lowercase Greek Symbols – Tensors

$\dot{\boldsymbol{\gamma}}$ Rate-of-strain tensor

$\boldsymbol{\tau}$ Stress tensor

Uppercase Greek Symbols

$\mathbf{\Gamma}_i$ Vector identifying a point in the phase space

Superscripts

$^\mathsf{T}$ Transpose operator

Subscripts

cf Conversion factor

Other Symbols

$\mathcal{K}$ Kernel function for Gaussian Process Regression

$\mathrm{N_p}$ Power number

$\mathrm{Re_{MR}}$ Generalised Metzner–Reed Reynolds number

Re Reynolds number

Acronyms / Abbreviations

CFD Computational Fluid Dynamics

CG Coarse-graining

CMEA Cocamide Monoethanolamine

DAV Direct averaging

DPD Dissipative Particle Dynamics

EO Ethoxyl group

EoM Equations of Motion

GPR Gaussian Process Regression

LEBC Lees-Edwards boundary conditions

LRBC Lagrangian rhomboid boundary conditions

MD Molecular Dynamics

MRF Multiple Reference Frame

NH Nosé–Hoover

PEO Polyethylene oxide

PIV Particle Image Velocimetry

PL64 Pluronic L64

PPO Polypropylene oxide

RBF Radial Basis Function

RZ Rotating zone

SLES Sodium Lauryl Ether Sulfate

SNR Signal-to-noise ratio

STL Standard Tessellation Language

TTCF Transient-time correlation function

Chapter 1

Introduction

Complex fluids encompass a wide range of systems, including emulsions, suspensions, surfactant solutions, polymer solutions, and polymer melts. In general, a complex fluid can be distinguished from a simple fluid by its mechanical properties and its response to applied stresses. Simple fluids are characterised by Newtonian behaviour, meaning that they exhibit constant viscosity under conditions of constant temperature and pressure.

In contrast, the viscosity of complex fluids depends on the characteristics of the imposed deformation (Larson, 1999). The simplest non-Newtonian behaviour shows dependence on the magnitude of the deformation, but for many fluids the timescale and deformation history also play a role. These kinds of fluids are ubiquitous in everyday life and are involved in numerous industrial processes and operations. The food industry makes extensive use of emulsions, such as mayonnaise (Štern et al., 2001), as well as foams (Kilara & Sharkasi, 1994) and suspensions. Personal care cosmetic products are often complex fluids by design, in which the viscosity is tuned to support the function of the fluid (Klein & Palefsky, 2007; Laba, 1993). Viscosity modifiers are used to facilitate dispensing from toothpaste tubes, while thickeners improve the consistency of soaps and shampoos during application. Many pigments added to varnishes and paints to control colour form suspensions, whose rheology is tuned to improve applicability (Cohu & Magnin, 1995). Complex fluids are also increasingly employed in pharmaceutical formulations for the production of creams, gels, and foams with suitable rheological properties and interactions with active ingredients (Di Spirito et al., 2024; Kabanov et al., 2002).

All the applications described above refer to the macroscopic behaviour of fluids, but their description relies on microscopic properties. The shear thinning rheology of a polymer melt depends on the extent to which deformation can disentangle, orient, or stretch polymer chains (Doi & Edwards, 1988). The viscosity of a colloidal suspension is influenced by particle–particle interactions, which depend on how the flow field and strain modify the separation distance between particles (Mewis & Wagner, 2011). The structures formed during the self-assembly of surfactants in aqueous solutions can create anisotropy at the microscale, thereby altering the mechanical properties of these fluids. Because the microstructure of complex fluids strongly influences their behaviour, they are also referred to as structured fluids (Larson, 1999). The separation of scales between microscopic characteristics and macroscopic properties in industrial contexts motivates the use of multiscale models to link these descriptions. In addition, strain rate, composition and temperature may vary in space and time within industrial equipment. This leads to an even more complex scenario due to microstructural reconfiguration.

In this context, there is significant potential for the development of computational models. Various simulation techniques allow reproduction of fluid behaviour at different scales, from microstructures to macroscopic fluid dynamics in industrial equipment. Despite the complexity of the task, the development of accurate models offers two main benefits for the study of complex fluids. The first is the prediction of macroscale variables related to operating conditions in industrial processes. A computational approach would enable optimisation of design and process without the costs associated with industrial-scale experiments. The second is the insight into phenomena occurring at the micro- and molecular scales, which helps to understand the mechanisms underlying structured fluid behaviour.

Mixing processes are an interesting test case for a multiscale simulation framework. They are an essential operation in the production of many structured fluids, and many types of equipment and operating conditions are explored during mixing processes. This is reflected in a wide range of fluid dynamics conditions explored and, of course, relevant variation in local composition.

Among the available methods for microscale description, Dissipative Particle Dynamics (DPD) has attracted considerable attention due to its coarse-grained molecular representation. The coarse-grained description reduces computational requirements compared to atomistic techniques such as Molecular Dynamics (MD).

Because DPD preserves hydrodynamic interactions, its ability to predict transport properties has been a focus since its introduction (Groot & Warren, 1997). Early studies considered the method promising for a range of systems, from colloids (Boek et al., 1996, 1997) to polymer solutions (Kong et al., 1997). DPD has already been used to study the microstructure of complex fluids in equilibrium conditions for surfactant solutions (Panoukidou et al., 2019) and gel-coated nanoparticles (Li et al., 2019). In this light, the use of DPD as a computational rheometer is particularly interesting, as it can also provide important information on the response of the microstructures under stress (Hendrikse et al., 2023; Santo et al., 2018). Over the years, transport properties of DPD fluids have been investigated from both theoretical (Marsh et al., 1997) and computational perspectives. When studying the rheology of many realistic fluids, it is more interesting to analyse the shear-dependent behaviour, which requires a non-equilibrium method (Prhashanna et al., 2016; Santo et al., 2018). This is the case for complex fluids, whose rheology has been explored by different works (Hendrikse et al., 2023; Nafar Sefiddashti et al., 2020) with generally satisfactory results, although some limitations remain. In particular, these methods exhibit high uncertainty in viscosity values at low shear rate values (Meng et al., 2015; Prhashanna et al., 2016). It is also documented that high shear rates can cause unexpected results, such as shear thickening in simple fluids (Boromand et al., 2015; Droghetti et al., 2018), or the disruption of microstructures in complex fluids (Hendrikse et al., 2023).

While particle-based methods are helpful in calculating the viscosity of fluids, other techniques are instead suited to reproduce the macroscale system at the process scale. Among these, Computational Fluid Dynamics (CFD) has been used to simulate a great variety of applications, including mixing in different types of equipment, from static mixers (Liu et al., 2006), to high shear mixers (Ferrari et al., 2023a), to stirred tanks (Montante et al., 2001). Static mixers have been simulated to investigate the fluid dynamics and pressure drops in laminar conditions (Liu et al., 2006; Nyande et al., 2021), turbulent conditions for multiphase flow (Pianko-Oprych & Jaworski, 2009), and to improve the geometrical design of the equipment (Hirschberg et al., 2009). Stirred tanks have been studied computationally for a long time (Brucato et al., 1998), studying the effect of numerics and turbulence models (Alcamo et al., 2005; Aubin et al., 2004), with greater interest on the more industrially common baffled systems. While less common, because of their lower mixing efficiency (Scargiali et al., 2013), there are also early computational studies on unbaffled stirred tanks, in

both laminar (Lamberto et al., 1999) and turbulent regimes (Ciofalo et al., 1996). A renewed interest in unbaffled configurations has been observed in the last decade, due to their advantages in solid-liquid mixing, and processes involving sensitive biofluids (Scargiali et al., 2017). At the same time, a specific aerated regime has been identified in which mixing efficiency is comparable to baffled systems (Busciglio et al., 2014). Consequently, recent works have started to focus on the comparison between baffled and unbaffled systems, from creeping flow (Tamburini et al., 2018) to fully turbulent conditions (Tamburini et al., 2019).

The multiscale problem is not easily solved, even once the tools to analyse the system at different scales are available. Within the same piece of equipment, local values of strain rate and composition can vary significantly, leading the fluid to experience a wide range of operating conditions. Since a DPD simulation would be required for each combination of strain rate and composition, simulating all possible conditions is not feasible due to the associated computational cost. A different coupling strategy is therefore required, and Gaussian Process Regression (GPR) has been proposed in the literature (Zhao et al., 2018) as a linking step between the microstructure scale and the process scale. GPR belongs to the class of machine learning methods and is well suited to regression problems involving relatively small datasets. The development of a GPR-based viscosity model would thus allow a significant reduction in the number of microscale simulations required to achieve accurate macroscale predictions.

The application of the multiscale approach described here to real mixing processes requires careful consideration of several aspects that are specific to DPD simulations. An appropriate DPD parametrisation is essential in order to correctly reproduce the fluid microstructure and its response to applied stresses, yet the identification of suitable interaction parameters is often system dependent. As a coarse-grained model, DPD is formulated in reduced units, which necessitates the identification of conversion factors to relate simulation results to meaningful physical quantities. The derivation of such mappings is well established for equilibrium simulations and depends on the characteristics of the system (Lauriello et al., 2021); however, their extension to non-equilibrium conditions remains far from consolidated. In particular, applying equilibrium-based conversion strategies to non-equilibrium simulations may lead to non-physical results, such as unrealistically high shear rates (Droghetti et al., 2018). At the same time, the accurate determination of shear-dependent properties requires the imposition of relatively high shear rates in DPD simulations

to overcome statistical noise, which may in turn influence the measured rheological response. As a consequence, *ad hoc* conversion factors are often introduced under non-equilibrium conditions, although these are not always directly related to the physical characteristics of the system. Additional complexity may also arise at the macroscale, depending on the operating conditions and the typology of the mixing equipment.

1.1 Aim of the study and thesis outline

The aim of this work is to develop and assess a multiscale simulation framework for the description of mixing processes involving complex fluids, with a particular focus on linking microscale rheological information to macroscale flow predictions. The study seeks to combine Dissipative Particle Dynamics simulations with Computational Fluid Dynamics through a data-driven surrogate model, in order to capture the dependence of viscosity on local composition and deformation rate while maintaining a feasible computational cost. Special attention is devoted to challenges that are specific to DPD simulations, including the use of model parameters for realistic fluids and the exploration of low shear conditions, with the aim of using conversion factors based on system characteristics also under non-equilibrium conditions. By addressing these aspects, this work aims to improve the robustness and applicability of multiscale approaches for realistic processing conditions, while keeping the macroscale modelling framework sufficiently general.

The dissertation is structured into six chapters. This introductory chapter sets the context of the work, highlighting the relevance of complex fluids, the need for multiscale modelling strategies, and the challenges associated with coupling simulations across different length and time scales.

Chapter 2 provides a general description of the techniques used throughout this work and outlines the assumptions adopted for the system studied. The governing equations of the macroscale model are presented, focusing on the key features of the Computational Fluid Dynamics technique. The use of the Multiple Reference Frame (MRF) to address the simulation of rotating impellers is described and discussed in the context of stirred-tank modelling. Dissipative Particle Dynamics is presented from a theoretical perspective, with a specific discussion on the computation of viscosity using non-equilibrium simulations. Finally, Gaussian Process Regression

(GPR) is introduced, highlighting its basic features and its role within the proposed multiscale framework.

In Chapter 3, the rheological behaviour of an industrial blend, made of a highly concentrated solution of Sodium Lauryl Ether Sulfate (SLES) in water, is reproduced using an automated multiscale approach. The rheological information is extracted by means of DPD simulations and is used to build a rheology model. This is implemented through GPR in a CFD simulation of the mixing equipment used for the blend production, *i.e.* the Sulzer SMX static mixer [1]. The DPD model of the fluid is assessed through a qualitative reproduction of the SLES/water phase diagram. The CFD simulaton is used to evaluate fluid dynamics details of the flow inside the static mixer, including local strain rate and pressure drop across the device. The calculated values are plausible when compared with results obtained for similar blends in the same piece of equipment.

In Chapter 4, the applicability of the transient–time correlation function (TTCF) formalism to a DPD system is investigated to allow high precision simulations at low shear rates. The objective is to standardise the use of TTCF for studying the shear-dependent rheology of DPD fluids under simple shear flow. The work illustrates the adaptations required by the peculiarities of the DPD force field. The results presented in this work refer to a simple DPD fluid to demonstrate the effectiveness of the method in a controlled Newtonian case. The main advantage of using TTCF is the possibility to simulate the fluid system at very low shear rates, while retaining a high signal-to-noise ratio. In this way, the approach is intended to make it possible to link the DPD conversion factors to the characteristics of the system and to obtain results that can be compared with experimental data. A successful method for simulating low shear rates is expected to yield more insightful results when applied to complex fluids. In such systems, a weaker external field is expected to produce a more realistic deformation of the microstructures.

Chapter 5 presents the macroscale modelling of unbaffled stirred tanks and compares CFD results with experimental measurements. The rheology of a specific Poloxamer, Pluronic L64, is described using rheometry experiments to identify suitable viscosity models. The power number and velocity field produced by the CFD model are compared with experimental data, showing good agreement only for low Reynolds numbers. In parallel, a GPR model is developed to describe the

[1] Sulzer SMX: https://www.sulzer.com/en/shared/products/static-mixer-smx-plus

dependence of viscosity on composition and shear rate for mixing simulations. The proposed multiscale coupling strategy is discussed, together with the computational costs associated with the transient nature of the problem, which restrict the present analysis to a qualitative assessment.

Finally, Chapter 6 summarises the main results of the work, highlighting its contributions and looking at the questions that remain open.

Chapter 2

Theoretical background

This chapter introduces the theoretical tools employed throughout this work to develop the proposed multiscale framework. The macroscale description is based on Computational Fluid Dynamics, with particular attention to the treatment of non-Newtonian rheology and rotating equipment through a Multiple Reference Frame approach. At the microscale, the fundamentals of Dissipative Particle Dynamics are presented together with the non-equilibrium methods used to evaluate shear-dependent viscosity and the issue of reduced units and conversion factors. Finally, Gaussian Process Regression is introduced as the statistical learning technique adopted to construct surrogate viscosity models bridging microscale simulations and macroscale predictions.

2.1 Macroscale model

The microscopic features of structured fluids are fundamental for understanding their macroscopic behaviour in industrial systems. Nonetheless, microscale models are not sufficient to obtain information on the results at the scale of a piece of equipment. The results of the study at the microscale can then be fed to macroscale models of industrial equipment to predict the system's response in different operating conditions. In this way, besides gaining new insights on the functioning of the system, it is possible to optimise a process or even the design of the equipment itself.

Computational Fluid Dynamics (CFD) is used in this work to develop numerical models of the studied industrial equipment. A computational domain is generated

and discretised, and the flow equations are solved using the finite volume method. All CFD simulations were conducted using OpenFOAM (www.openfoam.org). Version 8 was employed for the work described in Chapter 3 and Chapter 5, while version 9 was used for some simulations reported in Chapter 5. The systems studied are isothermal and in laminar conditions, hence two main equations are solved to calculate the flow field in the CFD domains. The governing equations are reported in their general transient form. For the steady-state simulations discussed in Sections 3.5, 5.3.1 and 5.3.2, the temporal derivative is equal to zero and the solution corresponds to a time-independent flow field. The transient form is retained only for the simulations involving the GPR-based viscosity model in Section 5.3.3, where the scalar concentration evolves in time and modifies the local viscosity. The first one is the continuity equation, which can be written in the following form

$$\nabla \cdot \mathbf{v} = 0, \tag{2.1}$$

since all the simulated fluids can be considered incompressible. The second one is the momentum balance equation

$$\rho \frac{\partial \mathbf{v}}{\partial t} = -\rho \nabla \cdot (\mathbf{v}\mathbf{v}) - \nabla p + \nabla \cdot \boldsymbol{\tau}, \tag{2.2}$$

where $\mathbf{v}$ is the velocity vector, p is the pressure, $\boldsymbol{\tau}$ is the stress tensor, and ρ is the fluid density, constant for incompressible fluids. By the generalisation of Newton's law of viscosity, it is possible to define the stress tensor $\boldsymbol{\tau}$ as

$$\boldsymbol{\tau} = \mu \left[\nabla \mathbf{v} + (\nabla \mathbf{v})^{\mathsf{T}} \right] = 2\mu \dot{\boldsymbol{\gamma}}, \tag{2.3}$$

valid for Newtonian fluids, which have constant dynamic viscosity μ. Hence, for a Newtonian incompressible fluid, Equation (2.2) reduces to the Navier-Stokes equation:

$$\rho \frac{\partial \mathbf{v}}{\partial t} = -\rho \mathbf{v} \cdot \nabla \mathbf{v} - \nabla p + \mu \nabla^2 \mathbf{v}. \tag{2.4}$$

Most of the fluids analysed in this work with CFD do not have a constant viscosity, hence a non-Newtonian model is required to correctly predict their flow behaviour. In these cases, a generalised Newtonian model is employed, in which the stress tensor is still defined as

$$\boldsymbol{\tau} = \eta \left[\nabla \mathbf{v} + (\nabla \mathbf{v})^{\mathsf{T}} \right] = 2\eta \dot{\boldsymbol{\gamma}}, \tag{2.5}$$

where η is the non-Newtonian dynamic viscosity. This is non-constant and depends on the magnitude of the rate-of-strain tensor $\dot{\boldsymbol{\gamma}}$, which has been introduced in Equation (2.3) and Equation (2.5) and is equal to

$$\dot{\boldsymbol{\gamma}} = \frac{1}{2}\left[\nabla \mathbf{v} + (\nabla \mathbf{v})^{\mathsf{T}}\right]. \tag{2.6}$$

Its magnitude is simply called strain rate $\dot{\gamma}$ and can be calculated as

$$\dot{\gamma} = \sqrt{2\dot{\boldsymbol{\gamma}} : \dot{\boldsymbol{\gamma}}}. \tag{2.7}$$

Since the fluid is still considered incompressible, the momentum balance equation for a generalised Newtonian fluid becomes

$$\rho \frac{\partial \mathbf{v}}{\partial t} = -\rho \mathbf{v} \cdot \nabla \mathbf{v} - \nabla p + \nabla \cdot \left[2\eta(\dot{\gamma})\dot{\boldsymbol{\gamma}}\right]. \tag{2.8}$$

In general, the viscosity η depends on other variables besides the strain rate, such as temperature or fluid composition. In this work, all the CFD simulations performed reproduce isothermal systems, removing the dependence of η on the temperature. Moreover, almost all the systems are evaluated with homogeneous composition at the steady state. The only exception is in Section 5.3.3, where the mixing of two initially segregated fluids is examined. Such simulation shows the initial evolution of a transient system, when large variations of the local composition are observed. For this case, the dependence of the mixture viscosity η on composition cannot be neglected and the viscosity model must take into account this additional independent variable. Being the system binary, the simplest way to keep track of its composition is through the transport of a scalar, C. In addition to the continuity and the momentum balance, the advection-diffusion equation for C is solved:

$$\frac{\partial C}{\partial t} = -\mathbf{v} \cdot \nabla C + \mathcal{D}\nabla^2 C, \tag{2.9}$$

where C is the concentration of one of the two species, and $\mathcal{D}$ is the binary diffusion coefficient. Hence, the non-Newtonian viscosity in Equation (2.8) becomes $\eta = \eta(\dot{\gamma}, C)$, a function of two variables.

2.1.1 Multiple Reference Frame

The equipment studied in Chapter 5 is a stirred tank, which requires a model to correctly treat the rotating impeller. Among the different approaches that can be employed in this case, a multiple reference frame (MRF) was chosen for these simulations. The method consists of isolating a portion of the domain, to which is applied a rotating reference frame. After identifying the axis of rotation through its unit vector $\hat{\mathbf{s}}$, knowing the rotational speed ω, which is a scalar, it is possible to calculate the rotation vector $\mathbf{w}$:

$$\mathbf{w} = \omega\hat{\mathbf{s}} \tag{2.10}$$

At this point, it is possible to define the global or inertial velocity $\mathbf{v}$ as function of the velocity relative to the motion of the blade $\mathbf{v}_\mathrm{r}$ and the vector of rotation $\mathbf{w}$:

$$\mathbf{v} = \mathbf{v}_\mathrm{r} + \mathbf{w} \times \mathbf{r}, \tag{2.11}$$

where $\mathbf{r}$ is the vector from the origin of the rotation axis, $\mathbf{s}$, to the centre of the computational cell. Substituting Equation (2.11) into Equation (2.2) leads to a Navier-Stokes equation in the rotating frame, where the variable is the relative velocity $\mathbf{v}_\mathrm{r}$:

$$\rho\left(\frac{\partial \mathbf{v}}{\partial t} + \frac{\mathrm{d}\mathbf{w}}{\mathrm{d}t} \times \mathbf{r}\right) = -\rho\Big[\nabla\cdot(\mathbf{v}_\mathrm{r}\mathbf{v}_\mathrm{r}) + 2\mathbf{w}\times\mathbf{v}_\mathrm{r} + \mathbf{w}\times\mathbf{w}\times\mathbf{r}\Big] - \nabla p + \mu\nabla^2\mathbf{v} - \rho\mathbf{w}\times\mathbf{v}, \tag{2.12}$$

which can be coupled with $\nabla \cdot \mathbf{v}_\mathrm{r} = 0$, since the fluid is incompressible. Furthermore, it is possible to rearrange Equation (2.12) to write it in the frame relative to the impeller rotation with the inertial velocity $\mathbf{v}$ as convected velocity:

$$\rho\frac{\partial \mathbf{v}}{\partial t} = -\rho\nabla \cdot (\mathbf{v}_\mathrm{r}\mathbf{v}) - \nabla p + \mu\nabla^2\mathbf{v} - \rho\mathbf{w} \times \mathbf{v}, \tag{2.13}$$

where the source term $-\rho\mathbf{w} \times \mathbf{v}$ appears. From the finite volume method point of view, the term $\nabla \cdot (\mathbf{v}_\mathrm{r}\mathbf{v})$ is instead a flux correction term that is applied to the faces of the cells composing the discretised domain. This is understandable considering the integral formulation of Navier-Stokes equation and using Gauss's divergence theorem. The volume integral of the divergence of a vector field becomes the total flux of that field across the surface that encloses said volume. Applying this to a single computational cell, it is possible to write the total velocity flux across its faces

as

$$\sum_{\text{faces}} \mathbf{v}_i(\mathbf{v}_{\mathrm{r},i} \cdot \hat{\mathbf{n}}_i)A_i = \sum_{\text{faces}} \mathbf{v}_i[(\mathbf{v}_i - \mathbf{w} \times \mathbf{r}) \cdot \hat{\mathbf{n}}_i]A_i, \tag{2.14}$$

where i is the subscript indicating a face, and A_i and $\hat{\mathbf{n}}_i$ are, respectively, the surface and the normal unit vector of said face. Expanding all the terms, the flux becomes

$$\sum_{\text{faces}} \mathbf{v}_i(\mathbf{v}_{\mathrm{r},i} \cdot \hat{\mathbf{n}}_i)A_i = \sum_{\text{faces}} \mathbf{v}_i(\mathbf{v}_i \cdot \hat{\mathbf{n}}_i)A_i - \sum_{\text{faces}} \mathbf{v}_i[(\mathbf{w} \times \mathbf{r}) \cdot \hat{\mathbf{n}}_i]A_i, \tag{2.15}$$

where the first term of the right hand side is the usual momentum flux, and the second term of the right hand side of the equation is the correction term implemented in the code. Thus, OpenFOAM solves the momentum equation for the inertial velocity $\mathbf{v}$ over the entire domain, while the corrections in Equations (2.13) and (2.15) are applied only to cells within the MRF zone.

2.2 Dissipative particle dynamics

Dissipative particle dynamics is a computational method that relies on a coarse-grained description of the molecules, which are grouped in larger particles, called beads. These beads represent the fundamental elements in DPD simulations and can contain a number of atoms or molecules that depends on the chosen level of coarse-graining (CG). The coarse-graining approach allows mesoscopic systems to be studied, enlarges the available spatial and temporal scales, and requires fewer computational resources than all-atom molecular dynamics (MD). After its first introduction by Koelman and Hoogerbrugge (1993), it was further developed by Groot and Warren (1997), while Español and Warren (1995) studied its formalisation from a statistical mechanics point of view. According to the standard DPD model, two beads i and j interact through three pairwise forces, the conservative force $\mathbf{f}_{ij}^C$, the dissipative force $\mathbf{f}_{ij}^D$, and the random force $\mathbf{f}_{ij}^R$. The conservative force is a soft repulsive force that allows the beads to overlap and has the following functional form:

$$\mathbf{f}_{ij}^C = \begin{cases} a_{ij}\left(1 - \dfrac{r_{ij}}{r_\mathrm{c}}\right)\hat{\mathbf{r}}_{ij}, & r_{ij} \le r_\mathrm{c} \\ 0, & r_{ij} > r_\mathrm{c} \end{cases}, \tag{2.16}$$

where a_{ij} is the repulsion parameter, which depends on the type of beads, $r_{ij} = |\mathbf{r}_{ij}| = |\mathbf{r}_i - \mathbf{r}_j|$ is the distance between the beads, $\hat{\mathbf{r}}_{ij} = \mathbf{r}_{ij}/r_{ij}$ is the unit vector pointing from bead j to bead i, and r_c is the cutoff radius. The dissipative and random forces are instead defined as:

$$\mathbf{f}_{ij}^D = -\gamma w^D(r_{ij})(\hat{\mathbf{r}}_{ij} \cdot \mathbf{v}_{ij})\hat{\mathbf{r}}_{ij}, \tag{2.17}$$

$$\mathbf{f}_{ij}^R = \sigma w^R(r_{ij}) \frac{\xi_{ij}}{\sqrt{\Delta t}} \hat{\mathbf{r}}_{ij}, \tag{2.18}$$

where $w^D(r_{ij})$ and $w^R(r_{ij})$ are their respective weight functions, $\mathbf{v}_{ij} = \mathbf{v}_i - \mathbf{v}_j$ is the relative velocity between the two beads, and ξ_{ij} is a random number drawn from a Gaussian distribution with zero mean and unit variance. The dissipative force causes a decrease of the energy in the system, which is restored by the random force. Español and Warren (1995) analysed the conditions ensure that the fluctuation–dissipation theorem is respected for DPD, deriving the constraints described here. The dissipative parameter γ and the random parameter σ must be related to each other using the following equation

$$\sigma^2 = 2\gamma k_B T, \tag{2.19}$$

where k_B is the Boltzmann constant and T is the temperature of the system. In addition to this, the following relation between the weight functions must be enforced:

$$w^D(r_{ij}) = \left[w^R(r_{ij})\right]^2. \tag{2.20}$$

Under these conditions, the system corresponds to a canonical ensemble, or NVT ensemble, where the number of particles, the volume, and the temperature are fixed. In statistical mechanics, such an ensemble is achieved by immersing the system in a large thermal bath. In atomistic and coarse-grained simulations, this is implemented through the use of thermostats, *i.e.* algorithms that maintain the temperature of the system constant (Frenkel & Smit, 2023). From this perspective, when the fluctuation–dissipation theorem is respected, the dissipative and random forces act as a thermostat. Moreover, the relation between $\mathbf{f}_{ij}^D$ and $\mathbf{f}_{ij}^R$ ensures correct hydrodynamic behaviour of the DPD fluids for sufficiently large scales (Español & Warren, 2017; Zhao et al., 2018). In the works presented in this thesis, as is common in the literature, the weight for the random force was chosen equal to the functional

form of the conservative force, hence:

$$w^D(r_{ij}) = \left[w^R(r_{ij})\right]^2 = \begin{cases} \left(1 - \dfrac{r_{ij}}{r_c}\right)^2, & r_{ij} \leq r_c \\ 0, & r_{ij} > r_c \end{cases}. \tag{2.21}$$

The trajectory of DPD beads is obtained from the integration of Newton's equations of motion (EoM)

$$\frac{d\mathbf{r}_i}{dt} = \mathbf{v}_i, \tag{2.22a}$$

$$\frac{d\mathbf{v}_i}{dt} = \frac{\mathbf{f}_i}{m_i}, \tag{2.22b}$$

where $\mathbf{f}_i$ is the sum of all the forces acting on bead i and m_i is its mass. The integration is usually performed using the modified velocity-Verlet algorithm proposed by Groot and Warren (1997), whose steps are reported here:

$$\mathbf{r}_i(t + \Delta t) = \mathbf{r}_i(t) + \mathbf{v}_i(t)\Delta t + \frac{1}{2}\frac{\mathbf{f}_i(t)}{m_i}\Delta t^2, \tag{2.23a}$$

$$\widetilde{\mathbf{v}}_i(t + \Delta t) = \mathbf{v}_i(t) + \Lambda\frac{\mathbf{f}_i(t)}{m_i}\Delta t, \tag{2.23b}$$

$$\mathbf{f}_i(t + \Delta t) = \mathbf{f}_i(\mathbf{r}(t + \Delta t), \widetilde{\mathbf{v}}(t + \Delta t)), \tag{2.23c}$$

$$\mathbf{v}_i(t + \Delta t) = \mathbf{v}_i(t) + \frac{1}{2m_i}\Big(\mathbf{f}_i(t) + \mathbf{f}_i(t + \Delta t)\Big)\Delta t. \tag{2.23d}$$

where $\widetilde{\mathbf{v}}_i(t + \Delta t)$ is called predicted velocity and Λ is a parameter that can be varied to improve the temperature control at higher timestep values. In the standard formulation of the velocity-Verlet integrator (Allen & Tildesley, 2017), the calculation of the predicted velocity can also be considered as advancing $\mathbf{v}_i$ by half a time step. Following this, the positions are updated and the force evaluated with the newly calculated positions. As a last step, the velocities are advanced by the last half time step. Imposing a value of $\Lambda = 0.5$ in Equation (2.23b), the standard velocity-Verlet algorithm is recovered, with the only difference lying in the expression of the force. This also depends on the beads' velocities in DPD simulations, due to the presence of the dissipative force, as in Equation (2.17). All the simulations presented in this work were performed using a value of Λ equal to 0.5.

2.2.1 DPD coarse-graining and parametrisation strategies

Beyond the choice of equations of motion and thermostat, a DPD model requires (i) a mapping from chemical species to coarse-grained beads and (ii) a set of interaction parameters governing bonded and non-bonded forces. These modelling choices strongly influence both equilibrium behaviour (e.g., self-assembled microstructures and phase behaviour) and, indirectly, non-equilibrium predictions such as viscosity. As a result, DPD parametrisation remains an active area of research, and multiple strategies have been proposed depending on the class of system and the target properties.

A widely used route for systems containing large molecules is based on Flory–Huggins theory, which provides a link between coarse-grained repulsion parameters and mixture thermodynamics (Groot & Warren, 1997). This approach has been employed in a broad range of applications, including surfactants in oil/water systems (Yuan et al., 2002), phase diagrams for ternary mixtures (Son et al., 2014), and polymer solutions (Prhashanna et al., 2015).

Alternative strategies rely on matching specific physico-chemical properties. For instance, parametrisation based on water–octanol partition coefficients was proposed for small molecules and has been successfully applied to surfactant systems (Anderson et al., 2017). In parallel, automated and workflow-driven approaches have also been developed to systematically construct coarse-grained models and identify parameters (Ferrari et al., 2023b, 2022; Fraaije et al., 2016).

In this thesis, these parametrisation concepts provide the basis for the DPD models used in later chapters. Once a parametrised model is defined, the next step is the evaluation of transport properties under flow, which is addressed in the following section through non-equilibrium simulation methods.

2.2.2 Non-equilibrium simulations

The viscosity of DPD fluids can be evaluated both with equilibrium (Lauriello et al., 2023, 2021) and non-equilibrium (Boromand et al., 2015) techniques. The Green–Kubo (Green, 1954; Kubo, 1957) and Einstein–Helfand (Helfand, 1960) relations are commonly used to estimate the zero-shear viscosity and are particularly well suited for Newtonian fluids. Versions specifically modified for DPD have been

proposed for the former (Ernst & Brito, 2005; Jung & Schmid, 2016) and the latter (Panoukidou et al., 2021). To improve the prediction of transport properties, Junghans et al. (2007) proposed an extension to the standard DPD thermostat. Whereas the standard DPD dissipative force depends only on the radial component of the relative velocity, as in Equation (2.17), the modified thermostat depends on the full relative velocity vector. For the same reason, increments of the dissipative coefficient γ were investigated (Boromand et al., 2015) and *ad hoc* thermostats have been developed (Lowe, 1999; Stoyanov & Groot, 2005).

For non–Newtonian fluids, the zero-shear viscosity is not sufficient to describe the rheological behaviour, hence non-equilibrium methods are required to evaluate the shear-dependent viscosity. For this purpose, in atomistic simulations, non-equilibrium simulations are usually set up using Lees-Edwards boundary conditions (LEBC) (Lees & Edwards, 1972). With this approach, a linear velocity profile is generated and maintained in the simulation box due to the periodicity of the boundary conditions. The method was developed for molecular dynamics simulations, but has been applied to DPD in previous works (Boromand et al., 2015; Droghetti et al., 2018; Hendrikse et al., 2023). For $\dot{\gamma} = \partial v_x / \partial y \neq 0$ using the LEBC, the shear is imposed using a "sliding brick" approach: the periodic images below and above the simulation box are displaced by $\pm L\dot{\gamma}\Delta t$ per time step with respect to the box itself, where L is the box's side length. The position and velocity of the particles that cross the y boundaries are set in order to take into account the different values of v_x in the periodic images. Moreover, the interaction between two particles separated by a boundary is corrected to consider the displacement of the periodic boxes.

All simulations in this work were performed using the open-source software LAMMPS (Large-scale Atomic/Molecular Massively Parallel Simulator) (Thompson et al., 2022), where LEBC are not implemented in their original formulation. The alternative approach uses Lagrangian rhomboid boundary conditions (LRBC) and is based on the actual deformation of the box in LAMMPS, applied with the `fix deform` command. The deformation induces a perturbation in the velocity of the DPD beads, resultin in a linear profile for the velocity within the simulation box. From a theoretical point of view, LEBC and LRBC are equivalent, provided that the velocity profile is taken into account in the periodicity of the boundary conditions (Todd & Daivis, 2017). The use of any of these boundary conditions is sufficient to generate a linear velocity profile, and it is referred to as the boundary-driven approach. Nevertheless, in addition to the lagrangian rhomboid boundary conditions,

the SLLOD equations of motion (EoM) are used. For a planar shear flow applied in the xy plane and a velocity profile in the x direction, the SLLOD EoM reduce to the following form (Todd & Daivis, 2017):

$$\dot{\mathbf{r}}_i = \frac{\mathbf{p}_i}{m_i} + \mathrm{i}\dot{\gamma} y_i, \tag{2.24a}$$

$$\dot{\mathbf{p}}_i = \mathbf{f}_i - \mathrm{i}\dot{\gamma} p_{yi}, \tag{2.24b}$$

where the overdot indicates a time derivative, except for $\dot{\gamma}$, which is the shear rate, i is the unit vector in the x direction, $\mathbf{f}_i$ is the sum of the forces acting on the bead i, $\mathbf{r}_i$ is the position vector, $\mathbf{p}_i$ is the momentum, and m_i the mass of the bead i. The use of SLLOD has important advantages with respect to the boundary-driven approach. It provides a direct link with response theory and the possibility of studying time-dependent flows (Evans & Morriss, 1990; Todd & Daivis, 2017). In LAMMPS, the SLLOD equations of motion are implemented together with the Nosé-Hoover (NH) thermostat (Maffioli et al., 2024):

$$\dot{\mathbf{r}}_i = \frac{\mathbf{p}_i}{m_i} + \mathrm{i}\dot{\gamma} y_i \tag{2.25a}$$

$$\dot{\mathbf{p}}_i = \mathbf{f}_i - \mathrm{i}\dot{\gamma} p_{yi} - \alpha \mathbf{p}_i \tag{2.25b}$$

$$\dot{\alpha} = \frac{1}{Q}\left(\sum_i \frac{\mathbf{p}_i^2}{m_i} - 3Nk_\mathrm{B}T\right), \tag{2.25c}$$

where α is the multiplier of the Nosé-Hoover thermostat, Q is the damping parameter, and N is the number of particles in the system. Nonetheless, as previously described, the dissipative and random forces of the DPD model act as a built-in thermostat. Hence, the presence of an additional thermostat in DPD simulations is often not strictly necessary to obtain an NVT ensemble. Two different approaches have been adopted in the works here presented regarding the NH thermostat, depending on the specific case study. In Chapter 3, the NH thermostat is kept active during the DPD non-equilibrium simulations, to ensure a better temperature control at high shear rates. On the other hand, in Chapter 4, the NH thermostat is deactivated, since the focus is on low shear rates. Moreover, potential interactions between the DPD thermostat and the NH thermostat would have been non-trivial to evaluate in the comparison between the two different viscosity calculation methods used in the work. Different options are available to deactivate the Nosé-Hoover thermostat while performing DPD simulations. A quick fix for this purpose is to set the `tdamp`

parameter in LAMMPS to a huge value, *e.g.* 10^{30}. The parameter `tdamp` is related to the relaxation time of the temperature, so the thermostat becomes more aggressive when this value becomes smaller. By setting it to a very large value, the relaxation time is larger than the length of the simulation, effectively deactivating the thermostat. The alternative pursued in Chapter 4 is to modify the LAMMPS source code to create a new fix that applies the SLLOD equations of motion without the thermostat. The new fix is called `nve/sllod` and it is available on GitHub[1]. It is important to emphasise that, despite the name of the fix, when it is used together with a DPD model, the resulting ensemble is an NVT.

After the system setup, during a non-equilibrium simulation, it is possible to calculate the apparent viscosity μ_{app} of the fluid using Newton's law of viscosity:

$$\mu_{\text{app}} = -\frac{\langle P_{yx} \rangle}{\dot{\gamma}}, \tag{2.26}$$

where the shear rate $\dot{\gamma}$ is an input parameter of the simulation, proportional to streaming velocity and the deformation of the box, and P_{yx} is the shear pressure. Equation (2.26) is consistent with Equation (2.3) when the relation between the viscous stress tensor and the molecular pressure tensor is considered for the off-diagonal components. For shear components, the isotropic pressure contribution is zero, and therefore $\tau_{ij} = -P_{ij}$ with $i \neq j$. In the present shear flow, this gives $\tau_{yx} = -P_{yx}$, and consequently $\mu_{\text{app}} = -\langle P_{yx} \rangle / \dot{\gamma}$. In this case, the off-diagonal term of the pressure tensor of interest is P_{yx} because the gradient of the x-component of the velocity is non-zero along the y direction. The elements of the pressure tensor are evaluated using the Virial (Parker, 1954) formula:

$$P_{\alpha\beta} = \frac{1}{V} \sum_{i=1}^{N} \left[m_i v_{i,\alpha} v_{i,\beta} + \frac{1}{2} \sum_{j \neq i}^{N} r_{ij,\alpha} f_{ij,\beta} \right], \tag{2.27}$$

where V is the volume of the simulation box, the subscripts α and β refer to the Cartesian components, and the subscripts i and j refer to different beads. As reported in Equation (2.26), we are interested in the off-diagonal component P_{yx}, but, in versions of LAMMPS used here, the pressure tensor is evaluated by considering it as always symmetric, hence $P_{yx} = P_{xy}$.

[1] https://github.com/f2a-dr/sllod_nve

2.2.3 Conversion factors

Due to its coarse-grained nature, the DPD model is based on reduced units, which are non-dimensional by definition. It is possible to retrieve the values in physical units from the DPD reduced units through the use of conversion factors. The values of these factors depend on the coarse-graining level of the model, but their identification depends on the specific system and is not trivial (Nafar Sefiddashti et al., 2020; Pieczywek et al., 2020). To connect the DPD description to the molecular one, an immediate approach is to derive the conversion factor from the mass and volume of the atoms and molecules that are represented by a single DPD bead. A third conversion factor is usually obtained from the energy, expressed as $k_B T$, where k_B is the Boltzmann constant and T is the temperature of the system. Different procedures were developed to obtain the time conversion factor by directly matching the self-diffusion coefficient in a simple fluid (Groot & Rabone, 2001; Lauriello et al., 2021), or the diffusion of a micelle in a polymer solution (Groot, 2000). The case of non-equilibrium simulations is more complex, where a well-established methodology for the identification of conversion factors is still lacking (Droghetti et al., 2018). The approach chosen for the work presented in Chapter 3 is based on matching the properties of interest for the systems studied. Hence, the conversion factors are identified in order to match the viscosity of the system at a given shear rate:

$$\mu_{\mathrm{cf}} = \frac{\mu}{\mu_{\mathrm{DPD}}} , \tag{2.28a}$$

$$\dot{\gamma}_{\mathrm{cf}} = \frac{\dot{\gamma}}{\dot{\gamma}_{DPD}} , \tag{2.28b}$$

$$\mathcal{E}_{\mathrm{cf}} = \frac{\mathcal{E}}{\mathcal{E}_{\mathrm{DPD}}} = \frac{k_{\mathrm{B}}\, T}{k_{\mathrm{B,DPD}}\, T_{\mathrm{DPD}}} . \tag{2.28c}$$

In Equation (2.28) the subscript "cf" indicates the conversion factor, while the values in DPD units are marked with the subscript DPD, and the remaining quantities are expressed in physical units. Defining also the conversion factor for a third quantity, in this case the energy in Equation (2.28c), it is possible to derive the conversion factor for any physical quantity. Considering that the standard DPD model is isothermal, it was possible to establish the energy of the system starting from a reference temperature.

2.3 Gaussian Process Regression

Gaussian process regression (GPR) is a mathematical and statistical tool akin to machine learning. To grasp the concept behind it, it is possible to think of a distribution over functions (Wang, 2023).

When there are no training data points, the *prior distribution* is usually a distribution of functions whose mean is equal to zero and whose standard deviation is unitary. Indeed, for every value of the independent variable x, the value of y is normally distributed around a mean, with an associated standard deviation. Hence, it is important to stress that the GPR does not output a functional form of the target function. It is instead a statistical model that outputs the predicted y values for any x in input, together with the uncertainty associated with the prediction. The shape of the functions sampled from this distribution derives from the kernel, which defines the properties, such as differentiability, of these functions. In this work a Radial Basis Function (RBF), or *squared exponential*, kernel was used:

$$\mathcal{K}(x_i, x_j) = \sigma_f^2 \exp\left(-\frac{d(x_i,\ x_j)^2}{2l^2}\right), \tag{2.29}$$

where σ_f is the *signal variance*, a pre-factor related to how much the functions vary vertically, $d(\cdot,\ \cdot)$ is the Euclidean distance between the two points x_i and x_j, and l is the *characteristic length-scale* (Rasmussen & Williams, 2005). The latter parameter expresses how the functions can vary: a high value of l will output smoother functions that do not show rapid variations. Often σ_f and l are referred to as *hyperparameters* since they are free parameters, whose values can be varied and are usually optimised through different techniques.

The addition of training points $(x_{\text{train}},\ y_{\text{train}})$ to the training data set changes the distribution of functions, which results in the *posterior distribution*. The effect of adding training data points can be noticed by comparing Figure 2.1.a and Figure 2.1.b, whose plots illustrate the use of the GPR on a test function $y = \sin(x)$. Considering the distribution of functions of a GPR model, it is possible to take samples from this distribution, analogously to what can be done by sampling a distribution of numbers. However, in this case, the samples correspond to functions that respect the constraints imposed by the used kernel and the training data set. Starting from the prior distribution in Figure 2.1.a, in which sample functions from the distribution are

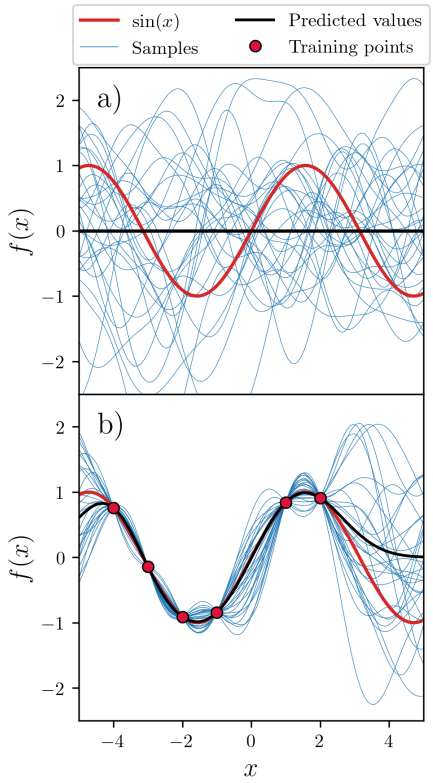

Fig. 2.1 Result of the GPR on an example function $y = \sin(x)$ with RBF kernel. Different steps are illustrated: a) prior distribution, b) posterior distribution obtained with six training data points. The functions in blue are samples from the distributions of functions.

plotted in blue, the addition of training points forces said functions to pass through them, as in Figure 2.1.b. The prediction values, plotted in black, are the result of the regression and they are generated by calculating the mean of the normally distributed functions.

Chapter 3

Coupling Computational Fluid Dynamics with Dissipative Particle Dynamics

This chapter is based on the article written by the candidate: De Roma, F., Marchisio, D., Boccardo, G., Bouaifi, M., and Buffo, A., "Application of a Multiscale Approach for Modeling the Rheology of Complex Fluids in Industrial Mixing Equipment", *Physics of Fluids*, 2024, (De Roma et al., 2024). The study has been conducted in collaboration with the multinational chemical company Solvay.

The personal care industry makes extensive use of ionic and non-ionic surfactants mixed with water for the production of everyday items, such as shampoos and soaps. Usually, the final products for the consumer market have low to moderate concentrations of surfactants ($\sim 12 - 25\,\%$) (Klein & Palefsky, 2007; Pandya et al., 2021). On the other hand, the semi-finished products present considerably higher concentrations of surfactants. Consequently, during the production step, a great variety of composition conditions are explored. In these blends, the concentration of surfactants plays a crucial role, due to their capability of undergoing self-assembly at the microscopic scale (Li et al., 2016). This process leads to the formation of different microstructures depending on composition, ranging from the micellar one to the hexagonal, cubic, and lamellar phases (Capaccio et al., 2020; Castaldo et al.,

2019). Self-assembly occurs also in solutions of water and Sodium Lauryl Ether Sulfate (SLES) (Capaccio et al., 2020; Castaldo et al., 2019; Li et al., 2016), one of the most commonly used surfactants for personal care products.

The presence of microstructures greatly influences the rheology of complex fluids, whose apparent viscosity depends on the composition and on the shear rate (Castaldo et al., 2019; Li et al., 2016). As a result, building a model for this rheological behaviour is considerably challenging and requires a significant amount of experimental data.

Several approaches exist to parametrise DPD models (as mentioned in Section 2.2.1); here we employ the water–octanol partition coefficient scheme to define the interaction parameters for the surfactant mixture. The method produces a set of parameters that can be used for different molecules and has already been used to simulate alkyl surfactants. These studies investigated the phase diagram for solutions of surfactants in water (Panoukidou et al., 2019), in calculating equilibrium properties (Anderson et al., 2018; Del Regno et al., 2021) and the effect of cosurfactants (Wand et al., 2020). These studies, though, analysed low concentrations of alkyl surfactants in water, exploring only the typical final formulations for the consumer market. Moreover, they focused on equilibrium properties, leaving aside the calculation of transport properties, such as diffusion coefficients and viscosity.

A multiscale approach coupling DPD and CFD was proposed by Zhao et al. (2018) to simulate the behaviour of non-Newtonian fluids. The method uses DPD simulations to compute the viscosity of the fluid at different shear rates, generating a dataset used to build the rheology model. This latter step is performed using the Gaussian Process Regression (GPR), a mathematical and statistical tool that belongs to the family of machine learning techniques. The GPR is then directly coupled with the CFD simulation, with the model that takes the shear rate values from the latter as input and gives the corresponding apparent viscosity in output. The use of this multiscale approach was, until now, tested only on a polymer melt (Zhao et al., 2018) and on a diluted polymer solution (Zhao et al., 2021) with promising results. In this chapter, a realistic industrial process is simulated, using a complex fluid composed of a mixture of surfactants in water at high concentration. The fluid flow is studied in a static mixer, a common piece of equipment used in the chemical and personal care industry for mixing fluids.

The chapter is structured as follows: Section 3.1 thoroughly illustrates the DPD model for the mixture of surfactants in water, Section 3.2 describes the macroscale model for the flow in the static mixer, and Section 3.3 presents the coupling strategy between the two techniques. Section 3.4 reports a qualitative validation of the DPD model for surfactant/water mixtures. All the results are illustrated and commented in Section 3.5, focusing on every step of the multiscale approach in different subsections. Finally, the conclusions will be presented in Section 3.6.

3.1 DPD model of the industrial blend

The modelled fluid is the Miraspec UB75, a mixture with three components and a composition reported in Table 3.1.

Table 3.1 Composition of the blend Miraspec UB75 used for the DPD simulations.

Component	Mass fraction
Inter ESA-70	0.72
CME/A2	0.08
Water	0.20

Besides water, the table reports the use of two other main components:

- The Inter ESA-70 is a mixture of SLES (Sodium Lauryl Ether Sulfate) at 70 % in water, whose main function is cleansing.
- CME/A2 is Cocamide Monoethanolamine (CMEA), used to control foaming, viscosity, and mildness of the product.

As depicted in Figure 3.1 and Figure 3.2, both SLES and CMEA have an alkyl tail, which can contain different numbers of carbon atoms. In particular, in Table 3.2 and Table 3.3 are reported the percentages of the molecules for every length of the alkyl chain. These distributions characterise the components of the blend and they are used to calculate the numerical concentrations of the beads in the DPD simulations of the Miraspec UB75.

The molecules of SLES in Inter ESA-70 contain only a single ethoxyl (EO) group, but in general SLES molecules can have different numbers of EO groups. This is also

Table 3.2 Percentage of SLES molecules with a specific length of the alkyl chain, expressed in number of carbon atoms, in the Inter ESA-70 component.

Number of Carbon atoms	Percentage in Inter ESA-70
12	70 %
14	30 %

Table 3.3 Percentage of CMEA molecules with a specific length of the alkyl chain, expressed in number of carbon atoms, in the CME/A2 component.

Number of Carbon atoms	Percentage in CME/A2
8	6 %
10	6 %
12	50 %
14	18 %
16	9 %
18	11 %

indicated in the chemical structure in Figure 3.1 through the presence of the subscript n in the $(CH_2CH_2O)_n$ groups. In particular, the phase diagram reported in the work of Li et al. (2016) refers to SLES molecules with three EO groups. Consequently, the molecule used for the parameter validation in Section 3.4 contained two more $[CH_2OCH_2]$ beads than the one depicted in Figure 3.1, indicated in green.

The process of developing the final model went through different steps. Initially, a DPD model for SLES and water was tested, using the set of parameters to reproduce the phase diagram of the mixture. Then a coarse-grained model for CMEA is developed with the same parametrisation method, and the correct reproduction of the microstructure of the blend is used as a test. In the end, the non-equilibrium simulations were performed with the developed DPD model, to obtain the information on the rheology of the fluid. It should be noted that there is no standard process to identify the parameters of a DPD model. Hence, depending on the system features and the level of coarse-graining, different methods can be used. Anderson et al. (2017) developed a parametrisation scheme based on the water–octanol partition coefficients. The parameters obtained with this technique have been used to simulate micellar blends of alkyl sulfate, alkyl ethoxylate and alkyl ethoxy sulfate surfactants (Anderson et al., 2017, 2018; Del Regno et al., 2021; Panoukidou et al., 2019; Wand

et al., 2020). In this work, we used the latter approach to model the SLES molecules, adopting the same coarse-graining (CG) level depicted in Figure 3.1.

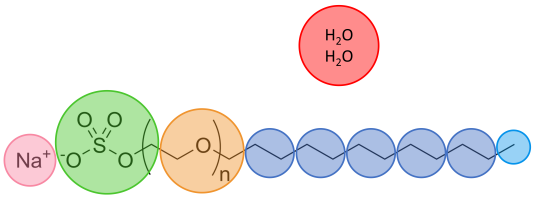

Fig. 3.1 Coarse-graining model adopted for water and SLES molecules (Panoukidou et al., 2019). Changing the length of the alkyl tail results in the addition or the subtraction of $[CH_2CH_2]$ beads.

The full list of conservative parameters a_{ij} and cutoff radii $r_{c,ij}$, reported in Table A.1, was obtained from previous works (Anderson et al., 2017; Panoukidou et al., 2019), while Table 3.4 reports the dissipative parameters γ and the stochastic parameter σ, common to all the beads. The bonded interactions between two

Table 3.4 DPD parameter common to every bead of the Miraspec UB75 blend.

Parameter	Value (DPD units)
γ	10.125
σ	4.5

consecutive beads are modelled using the harmonic potential in Equation (3.1),

$$E_{\text{bond}} = \frac{1}{2} k_{\text{bond}} (r_{ij} - r_0)^2, \tag{3.1}$$

with $k_{\text{bond}} = 150$ (DPD units) for all the bonds and an equilibrium distance calculated according to the following equation (Anderson et al., 2018):

$$r_0 = 0.1(n_i + n_j) - 0.01 \ , \tag{3.2}$$

where n_i and n_j are the number of heavy atoms linearly bonded in the i-th and j-th bead, respectively. According to this rule, $n_i = 4$ for the sulfate bead, with two oxygen atoms that are considered "branched" from the linear chain. The model also includes an angle harmonic potential that involves three beads interacting according

to the formula:

$$E_{\text{angle}} = \frac{1}{2} k_{\text{angle}} (\theta - \theta_0)^2 \,, \tag{3.3}$$

where θ is the angle between two adjacent bonds, $k_{\text{angle}} = 5$ (DPD units) and $\theta_0 = 180°$ for all the interactions.

Within the model, the treatment of the charged beads, *i.e.* the sodium ion and the sulfate group, is particularly interesting. The standard DPD model allows overlapping of the beads, but in the case of $r_{ij} = 0$ the Coulombic potential diverges, leading to the creation of artificial ionic pairs (González-Melchor et al., 2006; Groot, 2003). Previous works on analogous systems adopted a smeared charge approach to overcome this issue (Anderson et al., 2018; Del Regno et al., 2021; Panoukidou et al., 2019; Wand et al., 2020). The same approach was kept in this work, using a Slater-type charge smearing formulated by González-Melchor et al. (2006):

$$E_{\text{el}} = \frac{b q_i q_j}{\varepsilon_{\text{r}} r_{ij}} \left[1 - \left(1 + \frac{r_{ij}}{\zeta} \exp\left(-2 r_{ij}/\zeta\right) \right) \right] \quad r_{ij} \leq r_{\text{c,el}} \,, \tag{3.4}$$

where $b = 1/(k_{\text{B,DPD}} T \varepsilon_0 4\pi)$ is a constant, and, following the implementation of Anderson et al. (2018), the decay length is $\zeta = 1/0.929$ (DPD units) and $r_{\text{c,el}} = 3$ (DPD units). The latter parameter, $r_{\text{c,el}}$, acts like a cutoff for the treatment of the electrostatic forces. When $r_{ij} \leq r_{\text{c,el}}$ the interaction between two beads is evaluated through Equation (3.4), while for $r_{ij} > r_{\text{c,el}}$ the PPPM (particle-particle particle-mesh) solver, in its LAMMPS implementation, is used to evaluate the electric field. The previous literature focused on the study of solutions of SLES in water in micellar phases, a microstructure formed for low concentrations of the surfactant. Consequently, in these previous studies, the value of the dielectric permittivity constant was set equal to the one of water, $\varepsilon_{\text{r}} = 78.3$. In the case of the Miraspec UB75, the concentration of the SLES is substantially higher, hence the value $\varepsilon_{\text{r}} = 25$ was used. This latter value was chosen because it allowed the model to reproduce qualitatively the microstructures for different compositions of the mixture of water and SLES, as reported in Section 3.4.

To simulate the CMEA molecules, a new CG representation was developed, as illustrated in Figure 3.2.

The DPD interaction parameters for the beads forming the CMEA are already partly present in the literature, in the work of Wand et al. (2020); the rest were obtained using the same approach, the water/octanol partition method (Anderson et al., 2017),

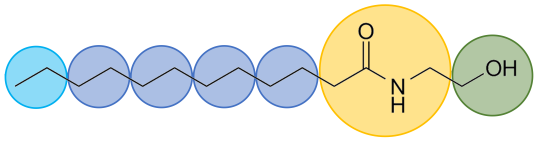

Fig. 3.2 Coarse graining model developed for CMEA molecules. Changing the length of the alkyl tail results in the addition or the subtraction of [CH_2CH_2] beads.

and they were kindly provided by Dr. Richard Anderson. These parameters are relative to the interactions of the [CH_2OH] bead present in the CMEA molecule and are also listed in Table A.1.

The set of conversion factors in Table 3.5 was used for the UB75 blend and it comes from matching one experimental value of viscosity. This approach was chosen due to the current impossibility of matching all the properties of a fluid with a single set of conversion factors in DPD. This becomes particularly true for transport properties and when performing non-equilibrium simulations. In this case, a linear velocity profile must be obtained in a small box, so the stream velocity must overcome the thermal velocity of the beads. Together with the nature of the DPD forces, this leads to very high shear rates at the macroscale and may result in a shift of the rheology model. Hence, the identification of conversion factors focused on matching the properties of interest, *i.e.* viscosity and shear rate, also intending to compensate for the described shift to higher shear rates. From the available experiments, the viscosity at the lowest shear rate was matched with the lowest meaningful value of the DPD shear rate. This corresponds to the lowest $\dot{\gamma}_{\mathrm{DPD}}$ that still results in a linear velocity profile from the imposition of the LRBC. For what concerns the energy

Table 3.5 Set of conversion factors used for the Miraspec UB75 DPD model.

μ_{cf} (Pa s)	$\dot{\gamma}_{\mathrm{cf}}$ (s^{-1})	$\mathcal{E}_{\mathrm{cf}}$ (J)
2.59	10	4.11×10^{-21}

conversion factor, it was obtained considering the temperature $T = 298.15\,\mathrm{K}$, the Boltzmann constant $k_{\mathrm{B}} = 1.38 \times 10^{-23}\,\mathrm{J\,K^{-1}}$, $T_{\mathrm{DPD}} = 1$, $k_{\mathrm{B,DPD}} = 1$ by applying Equation (2.28).

The equilibration stage lasted 1.2×10^6 timesteps, while the deformation of the non-equilibrium stage was set to 10^6 timesteps. The cumulative average of the DPD viscosity was computed, and its value at the end of the simulation was extracted.

3.2 CFD model of SMX static mixer

The application selected in this work to test the multiscale coupling procedure is one step of the production process of the Miraspec UB75. The post-mixing section of such an industrial process is simulated for the blend reported in Table 3.1. This phase is carried out in a static mixer, the Sulzer SMX [1], which consists of a tube filled with mixing elements. Depending on the kind of application, these internal elements can have different shapes (Etchells III & Meyer, 2003). The equipment used in Solvay's process consists of six identical mixing elements, each one rotated by 90° with respect to the previous, with the z axis as the axis of rotation. Every element is constituted by inclined bars, as shown in Figure 3.3. The inclination of each bar, with respect to both the main flux direction and the adjacent bars, is responsible for the mixing. The main flow is broken down into smaller flow paths which are subsequently recombined due to the peculiar geometry of the mixer internals. The static mixer geometry was provided directly by the company in order to reproduce the actual industrial setup as closely as possible. From this perspective, the initial empty region in Figure 3.3 is included to obtain a developed flow at the beginning of the mixing section. Conversely, the relatively short outlet section downstream of the mixing elements reflects the industrial configuration provided by the company and was therefore retained to preserve consistency with the industrial design. The details of the static mixer geometry are reported in Table 3.6.

The boundary conditions applied to the system are summarised in Table 3.7, where the outlet gauge pressure was set to zero. The mesh is tetrahedral and contains 5118292 cells, and it has been provided by the company, together with the equipment specifications. Based on the typical densities of these blends, $\rho = 1160\,\mathrm{kg\,m^{-3}}$ was imposed for the CFD simulations. The system was simulated at steady state, under the assumption of laminar flow, verified after the rheology of the fluid is obtained from the DPD simulations. As reported in Section 3.5.2, the Reynolds number for

[1] Sulzer SMX: https://www.sulzer.com/en/shared/products/static-mixer-smx-plus

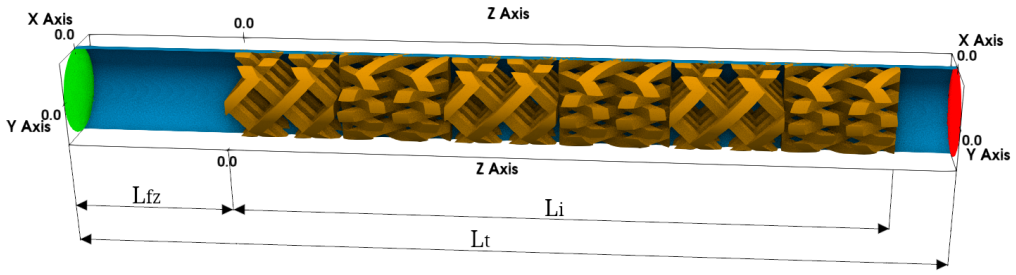

Fig. 3.3 Geometry of the SMX Sulzer static mixer used in the simulations. The colour scheme identifies different regions of the geometry: green for the inlet, red for the outlet, blue for the wall of the tube, and orange for the mixing elements. This colour coding is adopted for clarity, but in the actual computational domain used for the simulations the tube (blue) and the internals (orange) are part of the same wall patch, as in Table 3.7.

Table 3.6 Geometrical details of the computational domain.

		Symbol	Value
Diameter	(mm)	D	16
Tube length	(mm)	L_t	160
Internals length	(mm)	L_i	122
Number of elements		N_e	6
Number of bars per element		N_b	4
Initial free zone length	(mm)	L_fz	30

this system is of the order of 10^{-2}. The details of the CFD numerics are reported in Appendix F.

3.3 Coupling

A linking step between DPD and CFD techniques, described in Chapter 2, was developed to build a functional and automated multiscale approach. The coupling is based on an iterative flow scheme, implemented in Python and reported in Figure 3.4, with an approach similar to the one described in Zhao et al. (2018). The starting point is an initial DPD simulation, performed with a low value of shear rate $\dot{\gamma}_\mathrm{DPD}$, to obtain an initial viscosity value μ_0. This DPD step is necessary to obtain the first viscosity value μ_0, which is used to perform a CFD simulation with a Newtonian model. With the completion of this first CFD simulation, the loop indicated with the blue arrows in Figure 3.4 is initiated. This will be called *outer loop*, and it starts from the extraction

Table 3.7 Boundary conditions used for the CFD simulations with the SMX Sulzer.

	Wall	Inlet	Outlet
Velocity	No slip	Fixed value $v_x,\ v_y = 0\,\mathrm{m\,s^{-1}}$ $v_z = 1.38 \times 10^{-2}\,\mathrm{m\,s^{-1}}$	Zero gradient
Pressure	Zero gradient	Zero gradient	Fixed value $p = 0\,\mathrm{Pa}$

of the interval of the strain rate values from the CFD simulation. The strain rate interval is then passed to the GPR, which builds the model from the training data set, *i.e.* the pairs of points $(\dot{\gamma},\ \mu(\dot{\gamma}))$ obtained from the DPD simulations. Once the model is built, it takes the strain rate values as input and outputs the corresponding viscosity values (predictions) together with an associated standard deviation σ^{gpr}. The latter variable is then used to test the quality of the model in the entire interval. If the σ^{gpr} associated with any viscosity prediction is higher than a user-set limit $\sigma^{\mathrm{gpr}}_{\mathrm{lim}}$, the quality of the model is deemed not sufficient. In this case, the *inner loop*, indicated with the orange arrows in Figure 3.4, starts and a new DPD simulation is issued. The value of $\dot{\gamma}_{\mathrm{DPD}}$ imposed for this simulation is the one corresponding to the maximum value of σ^{gpr} obtained in the tested interval. This iterative process is repeated until the regression is satisfactory, and a new training data point is added for every cycle of the loop. This makes the algorithm automated, since a certain number of DPD simulations are launched until the desired accuracy in the shape of the constitutive relationship is met. When the exit condition for the *inner loop* is satisfied, the GPR is implemented in OpenFOAM as a viscosity model, and a new CFD simulation is launched. The updated strain rate interval, extracted from the last simulation, is compared with the one previously fed to the GPR. If the new interval is wider than a tolerance set by the user, the GPR model is tested on the updated interval and the *inner loop* may start again, depending on the values of σ^{gpr}. The difference between the extremes of the shear rate intervals is calculated as a relative difference according to the following equations:

$$\epsilon_{\mathrm{min,\,rel}} = \frac{\dot{\gamma}^{(\mathrm{n}-1)}_{\mathrm{min}} - \dot{\gamma}^{(\mathrm{n})}_{\mathrm{min}}}{\dot{\gamma}^{(\mathrm{n}-1)}_{\mathrm{min}}}\,, \tag{3.5a}$$

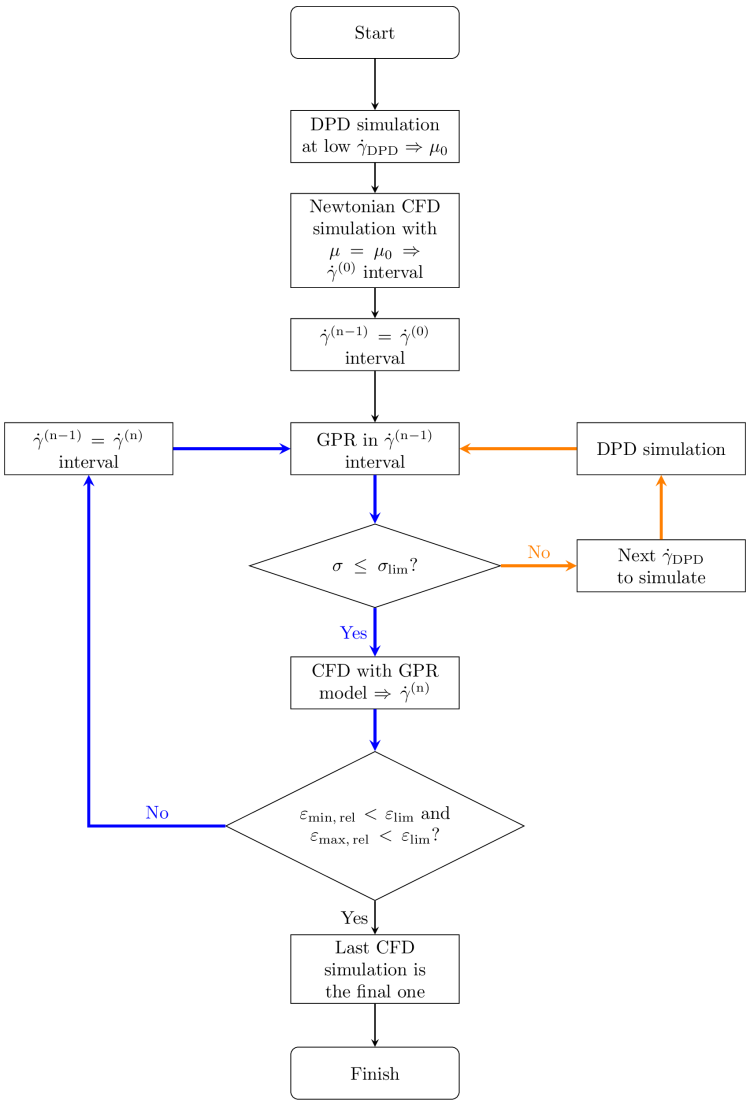

Fig. 3.4 Flowscheme used in the multiscale coupled approach. The following symbols are used: $\dot{\gamma}_{DPD}$ is the shear rate used for a DPD simulation, μ_0 is the viscosity obtained from the first DPD simulation and is used to perform the Newtonian CFD simulation, $\dot{\gamma}^{(i)}$ identifies the i-th rate interval from CFD simulations, σ^{gpr} is the standard deviation associated with the regression, σ^{gpr}_{lim} is the user-set limit for said standard deviation, $\epsilon_{.,rel}$ is the relative difference between the extremes of two shear rate intervals as in Equation (3.5), and ϵ_{lim} is the user-set limit for said relative differences.

$$\epsilon_{max,rel} = \frac{\dot{\gamma}^{(n)}_{max} - \dot{\gamma}^{(n-1)}_{max}}{\dot{\gamma}^{(n-1)}_{max}}, \tag{3.5b}$$

where $\epsilon_{max,rel}$ and $\epsilon_{min,rel}$ must be smaller than a set limit value ϵ_{lim} to exit the loop. It must be stressed that the absolute value is not used in Equation (3.5) because the

convergence criterion should differentiate between a wider and a narrower interval. The use of the absolute value will not lead to convergence in the case of a much narrower $\dot{\gamma}^{(n)}$ interval, since it would not take into account the sign of $\epsilon_{\text{max, rel}}$ and $\epsilon_{\text{min, rel}}$. For this reason, the order of the terms in the numerator of Equation (3.5) is of critical importance. Conversely, if the interval is not significantly wider or the quality of the regression is sufficient, the process exits from the *outer loop*. At this point, the CFD simulation that was performed last is considered to be the one that reproduces the studied system.

In this work, the Python module *scikit-learn* (Pedregosa et al., 2011) was used to perform the GPR step, and in particular to optimise the values of the hyperparameters σ_f and l. After the evaluation of the quality of the regression, the training data set and the values of the hyperparameters are passed to a GPR viscosity model implemented in the CFD code OpenFOAM. This viscosity model works as a function: after reading the GPR hyperparameters, it requires the local value of the strain rate, which is evaluated through the solution of the momentum balance equation, and it provides the viscosity value as output for each cell of the computational domain. The implementation of the GPR in OpenFOAM is written in C++ and it is inspired by freely available implementations on GitHub[2]. Due to the width of the shear rate intervals, the GPR for the simulated systems was performed in log-space, *i.e.* using the values of $\log(\dot{\gamma})$ vs $\log(\mu)$, with an approach comparable that of Zhao et al. (2018).

3.4 Solvay's UB75 blend: testing the DPD model

Before showing the results obtained by the multiscale approach, it is worth discussing more in detail the coarse-grained model chosen for the DPD representation of the molecules. As previously mentioned, among many available approaches to build a DPD model for a large molecule, in this work we used the approach of Anderson et al. (2017) to build the DPD model of the molecules in the Miraspec UB75 blend (Anderson et al., 2017, 2018). The starting point is the Inter ESA-70, a mixture of Sodium Lauryl Ether Sulfate (SLES) molecules with different lengths of the alkyl tail. The coarse-grained model of a SLES molecule and the DPD parameters reported by Panoukidou et al. (2019) were tested. The DPD model assessment is carried out

[2] https://github.com/jonfink/GP

through a qualitative comparison between simulation results and the experimental phase diagram of a SLES/water mixture (Li et al., 2016). It is important to note that the mixture reproduced to test the parameters does not exactly represent the Inter ESA-70. More precisely, the SLES molecules simulated in this step present a higher number of ethoxyl groups and a different length of the alkyl chain (Li et al., 2016). Nonetheless, the ability to reproduce a water/SLES phase diagram can provide a measure of the quality of the DPD model for these kinds of molecules. The lower side of the ternary phase diagram in Li et al. (2016) represents a binary mixture of SLES and water, from which three regions are identified to conduct the assessment. While for low SLES concentrations (0.002 36 to 28 % w/w) a micellar phase is found, intermediate SLES concentrations (31.5 to 56 % w/w) lead to the formation of the hexagonal phase and for high SLES concentrations (63 to 70 % w/w) a transition to lamellar phase occurs (Castaldo et al., 2019). One equilibrium DPD simulation in each of these regions was performed, and the resulting microstructure is qualitatively analysed. The three DPD simulations performed are summed up in Table 3.8, and the results were in agreement with the phase diagram, as it is possible to see in Figure 3.5.

Table 3.8 Values of SLES mass fraction used in the DPD simulation and corresponding expected microstructure according to (Castaldo et al., 2019; Li et al., 2016).

Expected structure	Simulated SLES mass fraction
Micellar	0.03
Hexagonal	0.45
Lamellar	0.67

To obtain a qualitative confirmation of the hexagonal structure, it was necessary to conduct a non-equilibrium simulation with an imposed shear rate $\dot{\gamma} = 0.1$ (DPD units) on the velocity component v_x along the y axis. This kind of behaviour was already reported in the literature for a DPD model that simulates a mixture of water and a tri-block co-polymer (Droghetti et al., 2018). When there is no shear applied the fluids form a network of worm-like micelles, as in Figure 3.5.c. From Figure 3.5.d it is clear how the application of a shear leads to the formation of rodlike micelles, typical of hexagonal structures.

Having assessed the qualitative capability of the model to predict the microstructure self-assembly for the binary system made of SLES and water, the addition of the third component was tested. The CME/A2 component is Cocamide Mo-

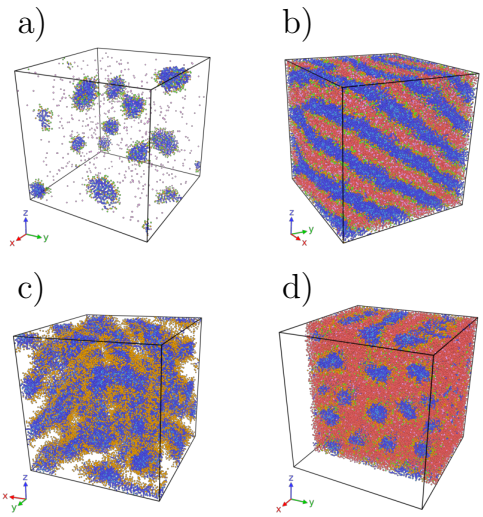

Fig. 3.5 Resulting microstructures of the DPD simulation performed. SLES mass fraction equal to a) 0.03, b) 0.67, c) and d) 0.45. In c) there is no shear applied, the water and the sulfate groups beads are not shown to highlight the network formed by the wormlike micelles, while in d) the system is shown after the application of a shear of $\dot{\gamma} = 0.1$ (DPD units) along the y axis to the velocity component v_x. To allow the micelles visualisation, the water beads are not shown in a). To facilitate the visualisation of the rodlike micelles in d) the box is sliced at $3/4$ of its length in the x direction. The colour coding of the beads is shown in Figure 3.1.

noethanolamine (CMEA), whose coarse-grained model was developed as described in Section 3.1 with parameters for the DPD forces retrieved from the literature (Anderson et al., 2017, 2018; Panoukidou et al., 2019). In Figure 3.6 it is shown that, for the composition in Table 3.1, lamellar microstructure is obtained, which is indeed expected for the Miraspec UB75.

3.5 Results and discussion

3.5.1 Multiscale approach and GPR

Once the performance of the DPD model for Miraspec UB75 was assessed, the model was then used to simulate a more realistic macroscopic application. The production of this blend requires the usage of a static mixer, in which the components are mixed in multiple steps at various temperatures. The multiscale approach is applied here to a simplified version of the production process, which is isothermal and with uniform

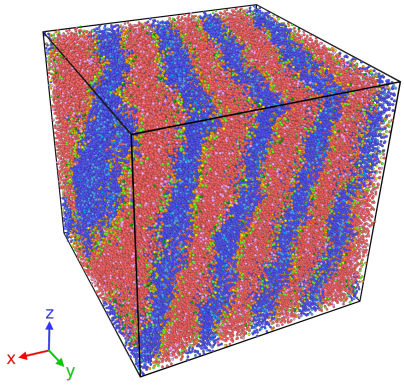

Fig. 3.6 Lamellar microstructure obtained from a simulation of the blend Miraspec UB75 with composition reported in Table 3.1. The colour coding of the beads is shown in Figure 3.1 and Figure 3.2.

composition. The latter is a strong assumption, equivalent to having the blend already mixed at the entrance of the equipment. Besides the general performance of the multiscale approach, the macroscopic variable of interest is the pressure drop across the mixer.

Table 3.9 Maximum and minimum values of the strain rate $\dot{\gamma}$ inside the CFD domain with the different viscosity models. The variable ϵ is the difference, calculated as a relative difference, between the values of one CFD run and the previous.

CFD run	$\dot{\gamma}_{\text{min}} \times 10^{-2}$ (s^{-1})	$\epsilon_{\text{min, rel}}$	$\dot{\gamma}_{\text{max}}$ (s^{-1})	$\epsilon_{\text{max, rel}}$
Newtonian	3.606		324.98	
GPR I	2.513	0.303	432.30	0.330
GPR II	2.488	0.010	361.05	−0.165

Table 3.9 summarises the CFD simulations performed, using incremental Roman numerals each time that an updated GPR model is used. Three CFD simulations were completed before the whole approach could reach convergence. The criterion described here refers to what, in the multiscale approach, is called *outer loop*, as expressed in Section 3.3. To evaluate the convergence of the iterative process, the strain rate interval extracted from a CFD simulation was compared with the one extracted from the previous simulation. The convergence criterion is set on the maximum ($\dot{\gamma}_{\text{max}}$) and on the minimum ($\dot{\gamma}_{\text{min}}$) values of the strain rate intervals, as

follows:

$$\epsilon_{\text{min, rel}} = \frac{\dot{\gamma}_{\text{min}}^{(\text{n}-1)} - \dot{\gamma}_{\text{min}}^{(\text{n})}}{\dot{\gamma}_{\text{min}}^{(\text{n}-1)}} \leq 0.01 \,, \tag{3.6a}$$

$$\epsilon_{\text{max, rel}} = \frac{\dot{\gamma}_{\text{max}}^{(\text{n})} - \dot{\gamma}_{\text{max}}^{(\text{n}-1)}}{\dot{\gamma}_{\text{max}}^{(\text{n}-1)}} \leq 0.01 \,, \tag{3.6b}$$

where the superscript (n) refers to the latest CFD simulation and the superscript (n − 1) refers to the previous CFD simulation. If the strain rate interval of the last CFD simulation is wider than 1 % with respect to the one from the previous simulation, the GPR should test the training data on the newly extracted interval. The condition is tested separately for the upper limit and the lower limit, and both need to be satisfied for convergence.

Figure 3.7 shows the regression process applied to the first shear rate interval, which is extracted from the CFD simulation with the Newtonian viscosity model. Besides the rheograms, Figure 3.7 depicts also information about the quality of the regression for the GPR loop, called *inner loop* in the multiscale approach (Section 3.3). As seen from Figure 3.7.a2 and Figure 3.7.b2, to reach the convergence of the GPR, the following equation must be satisfied in the whole strain rate interval:

$$\sigma^{\text{gpr}} \leq \sigma_{\text{lim}}^{\text{gpr}} = 10^{-2} \tag{3.7}$$

with $\sigma_{\text{lim}}^{\text{gpr}}$ corresponding to the dotted orange line in the plots. Figure 3.7.a1 and Figure 3.7.a2 report the results of an incomplete GPR viscosity model, obtained with a partial training data set of two $(\dot{\gamma}, \mu(\dot{\gamma}))$ pair of points. Figure 3.7.b1 and Figure 3.7.b2, instead, illustrate the viscosity model GPR I (Table 3.9), obtained after the convergence of the GPR on the interval extracted from the Newtonian CFD simulation. Comparing Figure 3.7.a1 and Figure 3.7.b1 it is possible to illustrate how the addition of the third data point to the data set substantially improves the regression. This is confirmed by the low values of σ shown in Figure 3.7.b2, which correspond to a very narrow 95 % confidence interval in Figure 3.7.b1, as visible only in the magnified inset.

The GPR I and GPR II viscosity models (Table 3.9) are depicted in Figure 3.8.a and Figure 3.8.b, respectively. As previously stated, the GPR I model is built on the shear rate interval extracted from the first CFD simulation, which employed a Newtonian viscosity model. GPR II model is instead built on the shear rate

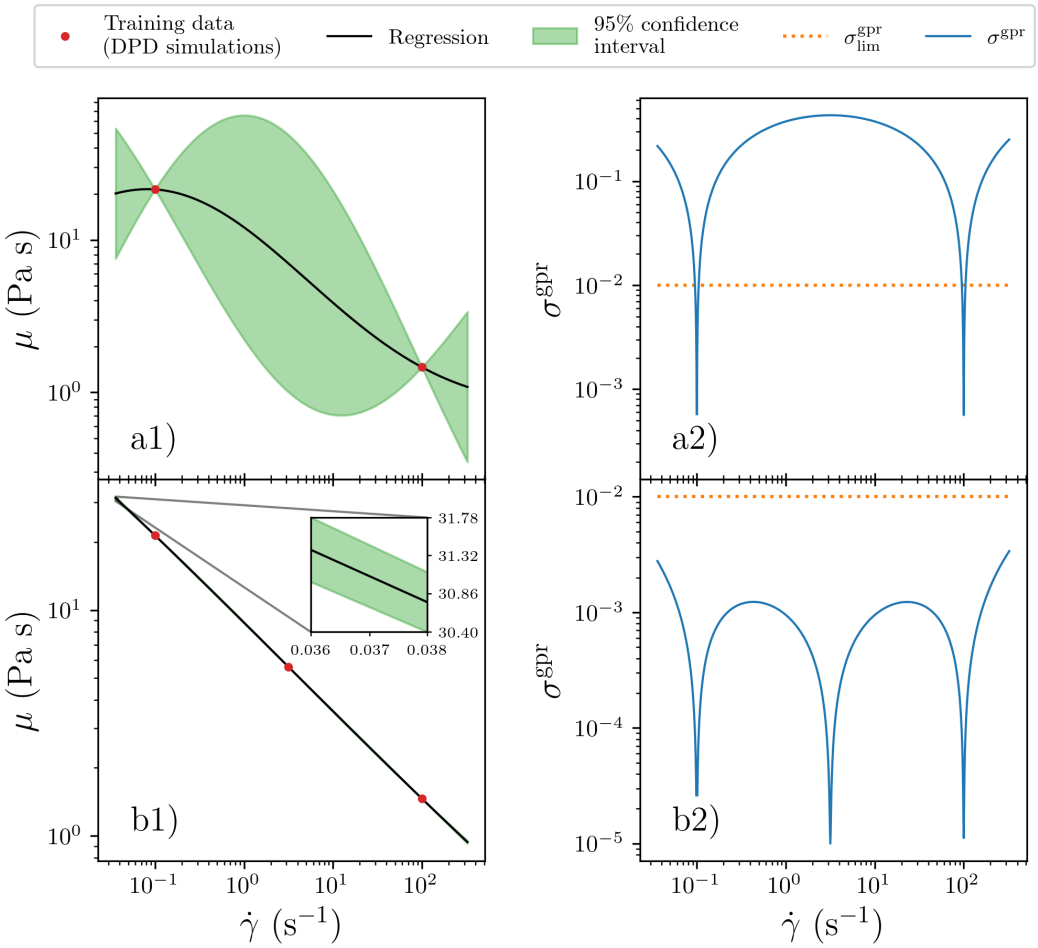

Fig. 3.7 Illustration of the regression process to build the viscosity model GPR I, using the shear rate interval extracted from the Newtonian CFD simulation. The different plots show: a1) rheogram of the incomplete GPR I model before convergence, a2) standard deviation associated with the regression of the incomplete GPR I model before convergence, b1) rheogram of the converged GPR I model, b2) standard deviation associated to regression of the converged GPR I model. The inset in b1) contains the magnification of a portion of the regression, to allow the visualisation of the narrow 95 % confidence interval.

interval extracted from the second CFD simulation, which implemented the GPR I model. Moreover, the training data set used is the same for the two viscosity models, indicating that no additional DPD simulations were necessary to reach the convergence of the regression step. Consequently, the two viscosity models are very similar and the only difference resides in the shear rate interval. Indeed, the GPR II is built on a wider interval than GPR I, as emphasised by the dotted vertical grey lines in Figure 3.8. The 95 % confidence intervals in Figure 3.8.a1 and Figure 3.8.b1 are

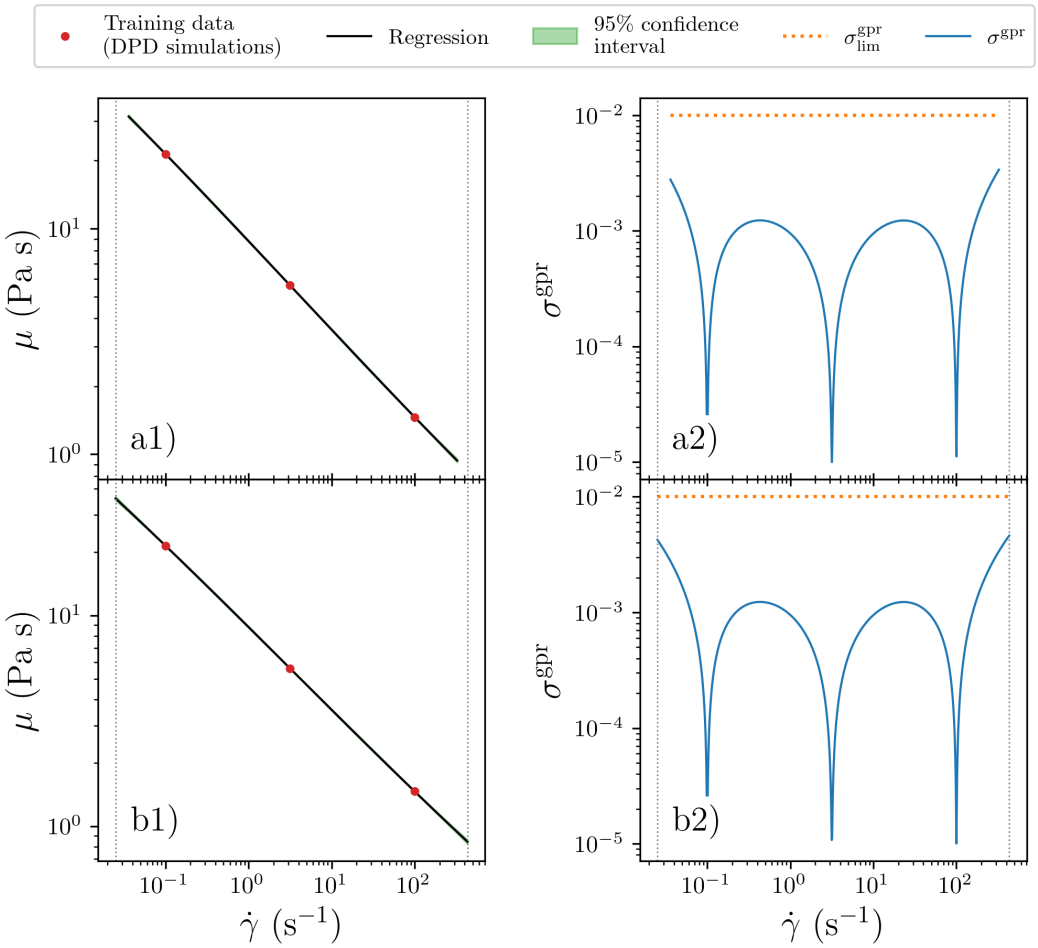

Fig. 3.8 Comparison between GPR I and GPR II viscosity model. The plots show: a1) rheogram of the converged GPR I model, a2) standard deviation associated to the regression of the converged GPR I model, b1) converged GPR II model, b2) standard deviation associated to the regression of the converged GPR II model. The 95 % confidence intervals in a1) and b1) are slightly visible only close to the extremes of the curves, due to their narrowness. The dotted grey vertical lines highlight the different width between the intervals used for the regression in the two models.

very narrow and slightly visible only close to the extremes of the intervals. Hence, σ reaches its maxima in correspondence to the interval extremes in both Figure 3.8.a2 and Figure 3.8.b2, since the GPR technique performs worse in extrapolating than in interpolating.

A third GPR viscosity model was not built since, as reported in Table 3.9, the difference between the last $\dot{\gamma}$ interval and the previous one respected the convergence criteria in Equation (3.6). The difference between the limits of the strain rate intervals

is also noticeable in Figure 3.9, where the cumulative distribution functions of $\dot{\gamma}$ are plotted. The same figure also shows that the $\dot{\gamma}$ distributions for the two GPR models are basically superimposed, and the differences from the Newtonian one are not very significant. The reason for such small differences is probably due to the viscosity value ν used for the Newtonian simulation. The initial guess for the value of ν resulted to be intermediate when compared to the extreme values of the final viscosity interval (Figure 3.12.a). This could explain both the slight shift to higher $\dot{\gamma}$ values of the Newtonian distribution and the different shape for intermediate values of strain rate.

A total of three DPD simulations were necessary during the whole process, to have the Equation (3.7) to be satisfied, as illustrated by the series labelled as "Training data" in Figure 3.7 and Figure 3.8. The final viscosity model obtained with the multiscale approach describes a shear-thinning fluid. This is consistent with the experimental measurements available, which usually lead to a power-law viscosity model for simulation purposes.

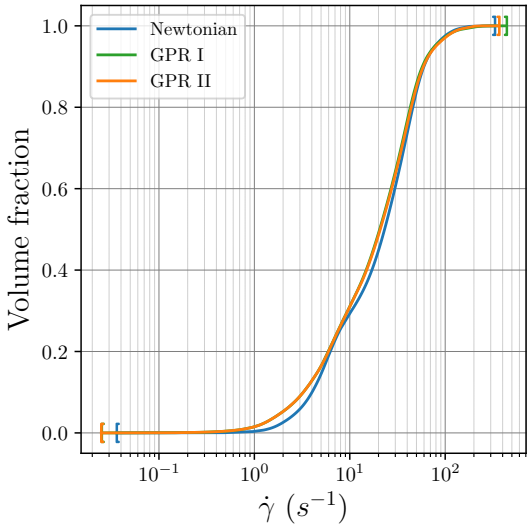

Fig. 3.9 Volume cumulative distribution function for the shear rate values in the different CFD simulations. The "[" and "]" markers correspond to the $\dot{\gamma}_{\text{min}}$ and $\dot{\gamma}_{\text{max}}$ respectively, for every interval.

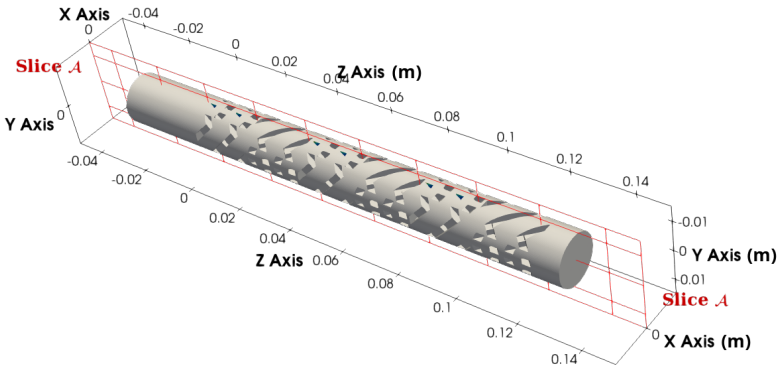

Fig. 3.10 Visual representation of the slice $\mathcal{A}$ used for contour plots. This cuts the CFD domain with the plane $x = 0$ m. All the lengths in the figure are expressed in metres.

3.5.2 CFD simulations

The results of the CFD simulations are analysed qualitatively through contour plots on the slice shown in Figure 3.10. The figure shows the slice $\mathcal{A}$, that cuts the domain with the plane $x = 0$ m from the inlet section to the outlet one. In Figure 3.11 the just described slice is used to compare the strain rate $\dot{\gamma}$ inside the domain from different simulations. In these contour plots, it is shown that the strain rate trend in the domain is similar regardless of the viscosity model used. The strain rate values are higher close to the walls of the tube and close to the mixing elements, while regions of low strain rates are found mostly at the inlet and outlet. Hence, the contour for the $\dot{\gamma}$ is in a qualitative agreement with the theory since a steeper variation of the velocity of the fluid is expected in correspondence with the walls. The only visible differences in the contour plots are confined to the inlet region in the simulation with the Newtonian model. This is due to the viscosity value of the fluid in that region, lower than the one in the non-Newtonian simulations, which consequently influences the distribution of $\dot{\gamma}$.

Figure 3.12 illustrates the contour plot for viscosity in the same plane. Since the Newtonian model was employed, Figure 3.12.a reports a constant value, and the viscosity corresponds to an intermediate value when compared to the whole interval of μ explored by the GPR models. As already noticeable from the rheogram in Figure 3.8,

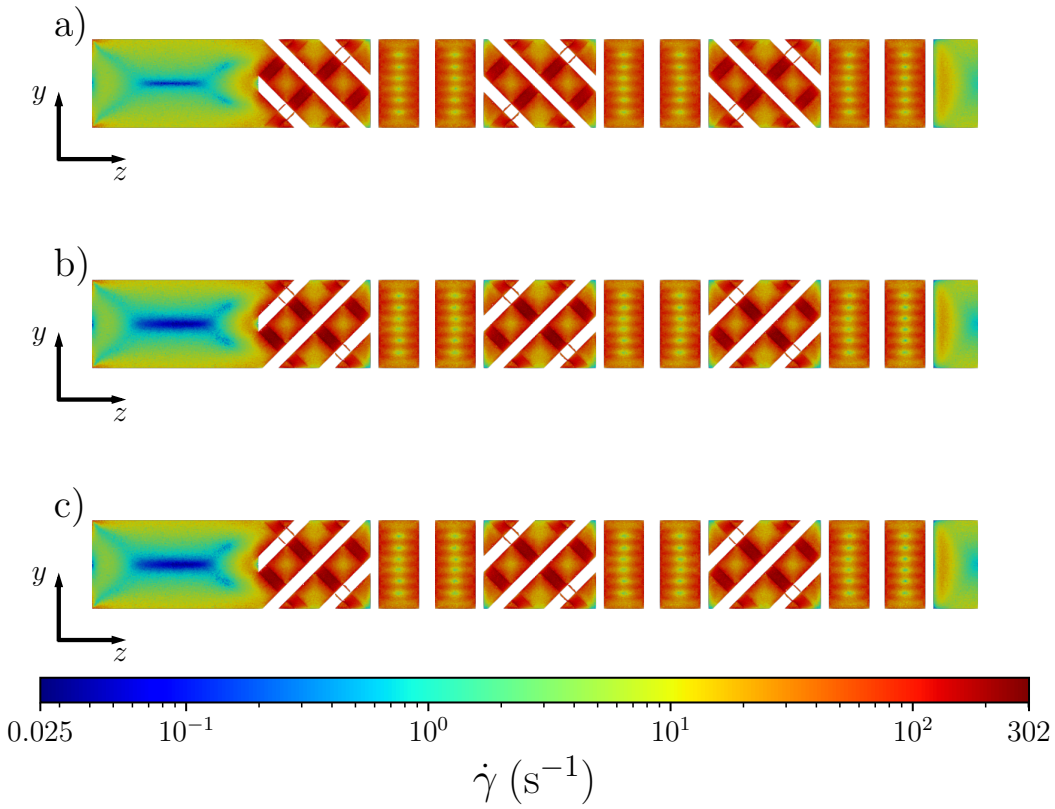

Fig. 3.11 Contour plot for the strain rate $\dot{\gamma}$ in correspondence of the slice $\mathcal{A}$. The values are plotted using a logarithmic scale for the colour bar. Different CFD runs are shown: a) Newtonian model, b) GPR I viscosity model, c) GPR II viscosity model.

a shear-thinning model resulted from the DPD simulations. This shear-thinning behaviour is visible in Figure 3.12.b, where the viscosity is lower in correspondence with the high strain rate regions of the mixing elements (Figure 3.11.b). When

Table 3.10 Pressure drop across the static mixer system for the different CFD simulations.

CFD run	Δp (Pa)
Newtonian	2.90×10^5
GPR I	2.41×10^4
GPR II	2.50×10^4

compared with the viscosity of the GPR model, the value of μ for the Newtonian simulation resulted lower in the inlet and outlet regions, but higher in the mixing section. Since the latter brings a substantially higher contribution to the pressure

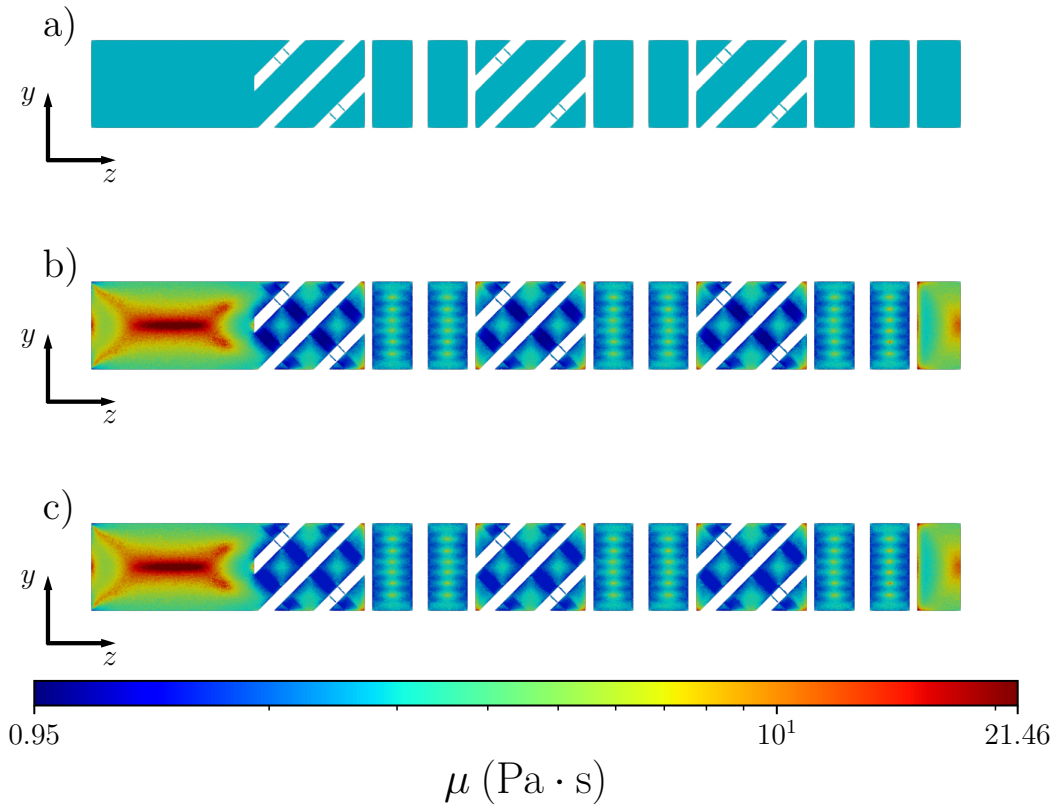

Fig. 3.12 Contour plot for the viscosity μ in correspondence of the slice $\mathcal{A}$. The values are plotted using a logarithmic scale for the colour bar. Different CFD runs are shown: a) Newtonian model, b) GPR I viscosity model, c) GPR II viscosity model.

drop, the Newtonian model presented a value of Δp higher by one order of magnitude than the GPR models, as in Table 3.10. The difference between GPR I and GPR II can be ascribed to the different $\dot{\gamma}$ explored: the GPR I simulation reached higher values of strain rate (Table 3.9), resulting in a lower viscosity in the mixing section and slightly lower Δp. As a final result, the pressure drop obtained from the last CFD simulation was $\Delta p = 2.50 \times 10^4$ Pa.

Though it is not possible to carry out a validation of this result, its order of magnitude can be considered reasonable given the investigations done by Solvay in static mixers. In particular, a comparison can be made with a mixture at 65 % of SLES in water, flowing in an SMX static mixer with a smaller diameter of 4.95×10^{-3} m. This system has been studied through CFD simulations and with the correlations proposed by Liu et al. (2006), using a power law to model its rheology. For a generalised Metzner–Reed Reynolds number (Liu et al., 2006; Metzner & Reed,

1955) of $\mathrm{Re_{MR}} = 6.54 \times 10^{-2}$ it was obtained $\Delta p = 1.66 \times 10^4$ Pa from the CFD simulations, and $\Delta p = 1.70 \times 10^4$ Pa using the correlation of Liu et al. (2006). By fitting the experimental measures available on Miraspec UB75 (see Section 3.5.3) with a power law, it was possible to calculate $\mathrm{Re_{MR}} = 6.38 \times 10^{-2}$ for the simulation of this work. The comparisons between these results show an agreement on the order of magnitude, though they cannot be considered as a validation process.

3.5.3 Viscosity model from DPD simulations

The application of a shear to a DPD fluid still presents some unsolved issues. In particular, an unphysical shear-thickening behaviour was found even for Newtonian fluids in high shear rate conditions (Boromand et al., 2015). Moreover, for very low shear rate values, the thermal noise prevails over the streaming velocity imposed by the box deformation. As a consequence, it becomes impossible to obtain a linear velocity profile, *i.e.* a constant imposed shear rate, and to apply Equation (2.26). The use of DPD simulations in large shear rate intervals should be tested, to avoid the occurrence of the described computational artefacts. In this work, partial mitigation of these effects was obtained through the use of a higher dissipative DPD constant γ combined with the SLLOD equation of motion, described in Section 2.2.2. Therefore, the results used to build the rheology model were obtained from simulations performed in a safe DPD shear rate interval.

The viscosity results obtained from the DPD simulations were compared with the results of two sets of experiments, previously performed at Solvay with the blend Miraspec UB75. The measurements were carried out with the Brookfield DV-II+ viscometer, using the LV3 spindle at 25 °C. The results are shown in Figure 3.13, where it is important to remember that the first DPD point corresponds perfectly because this point was used to identify the conversion factor in Table 3.5. The agreement between the simulations and the experiments is remarkably good, but more simulations and experiments are needed to increase the robustness of the model. In particular, the effects of the temperature and composition should be taken into account since they can have a great impact on the value of viscosity of these kinds of mixtures.

To further assess the quality of the viscosity model built on the DPD simulations, a power law was used to fit both the experimental data and the prediction from the

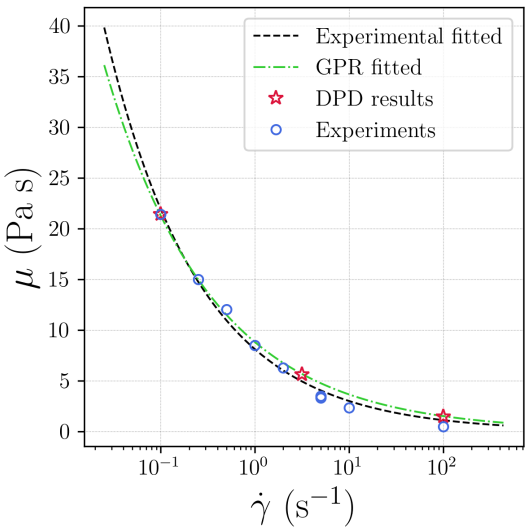

Fig. 3.13 Comparison between the viscosity model obtained from experimental results and DPD simulations. The blue hollow circles represent the experiments performed at Solvay, and the red hollow stars are the results of the DPD simulations. The black dashed line is the power law resulting from the fitting of the experimental data, while the green dashed and dotted line is the power law resulting from the fitting of one thousand GPR predictions logarithmically spaced on the interval from GPR I in Table 3.9.

GPR. This is expressed as

$$\mu = k \cdot \dot{\gamma}^{\,n-1}, \tag{3.8}$$

where k is the consistency index and n is the flow behaviour index. The power law is one of the most commonly used functions in rheology to approximate the behaviour of shear-thinning fluids for intermediate shear rates. It should be reminded that the GPR does not output a functional form, but a value of apparent viscosity for every shear rate value in input. Hence, to obtain a power law model for comparison, the GPR was performed to produce one thousand of $(\dot{\gamma}, \mu)$ pair of points in the final interval (GPR I in Table 3.9). These points are fitted with a power law and the comparison with the power law generated from the experimental data is illustrated in Figure 3.13, while the parameters of the power law are reported in Table 3.11. As it is possible to see from Figure 3.13 and table 3.11, the two fitted functions are close to each other, indicating that the GPR model provides a physically reasonable description.

Table 3.11 Parameters obtained from the fitting process of the experimental and GPR data using the power law in Equation (3.8).

Data set	k (Pa s^n)	$n-1$
Experimental	$8.11 \pm 3.0 \times 10^{-1}$	$-0.432 \pm 2.0 \times 10^{-2}$
GPR	$8.81 \pm 3.0 \times 10^{-3}$	$-0.383 \pm 1.4 \times 10^{-4}$

3.5.4 Multiscale approach computational performance

The idea behind the approach described in this work is the automatic selection of which DPD simulation to perform. This should lead to a reduction of the computational resources needed, through the minimisation of the number of DPD simulations. The simulations were performed on a workstation with a CPU "Intel® Xeon® Gold 6248 CPU @ 3.00GHz" using 24 cores. The time required by each simulation is reported in Table 3.12. Here, the CFD simulations are identified through the viscosity model used to perform them, while the DPD simulations are numbered following the order of execution. It is possible to discriminate between these DPD simulations through the applied shear rate, as reported in Table 3.13. In Table 3.12 is evident that the DPD simulations are the bottleneck of the automated approach, requiring from six to ten times the time of a CFD simulation.

Table 3.12 List of simulations in the order in which they were performed, with the corresponding computational time. The performed *inner loops* are also indicated.

	Simulation	Computational time (h:m)
	CFD Newtonian	0:14
1° GPR–DPD loop	DPD 1°	6:08
	DPD 2°	11:24
	DPD 3°	8:02
	CFD GPR I	1:09
	CFD GPR II	1:10

For what concerns the variability of the time needed to complete a simulation, it appears that a simulation with the GPR model can take up to about five times as long as a Newtonian one. The Newtonian simulation stopped after 588 iterations, while the GPR model continued until 2000 iterations. This can be the sign of overly strict convergence criteria for the CFD simulation, which can be affected not only by the viscosity model but also by the quality of the mesh. Consequently, a different

mesh or a better choice of the convergence parameter could lead to a reduction of the computational time.

Table 3.13 List of DPD simulations with the corresponding time to completion and the imposed shear rate $\dot{\gamma}$. The simulations are ordered with increasing $\dot{\gamma}$, to highlight the dependence of the requested time on the imposed shear rate.

Simulation	$\dot{\gamma}$ (DPD units)	Computational time (h:m)
DPD 1°	0.01	6:08
DPD 3°	0.317	8:02
DPD 2°	10	11:24

Conversely, for the DPD simulation, there is a strong dependence of the computational time on the value of $\dot{\gamma}$. Higher values of the shear rate imposed on the simulation box lead to longer computational times to complete the simulation, according to Table 3.13.

Using an automated approach for choosing the best shear rate value to add a point to the training data set led to satisfactory results in terms of computational time. Nonetheless, it must be noted that the rheogram resulted simple enough to obtain a good quality regression with only three training points. Consequently, to assess the computational advantages of this approach with more accuracy, it should be tested on a more complex rheology model, *e.g.*, including the effect of composition. Instead, regarding the CFD and DPD techniques, the computational time depends strongly on the models implemented in these kinds of simulations, so it is not possible to make a generalisation.

3.6 Conclusions

The focus of the work presented in this chapter was the development of a multiscale automated approach that could allow the simulation of complex fluids in typical mixing equipment. The proposed framework aimed to obtain information on macroscopic variables, such as pressure drops across a static mixer, through Computational Fluid Dynamics (CFD) simulations. The rheological model for the non-Newtonian fluid was derived from Dissipative Particle Dynamics (DPD) simulations. These were used as training dataset for a Gaussian Process Regression (GPR), which provided a

viscosity model for the macroscale model. The features of the GPR technique were exploited to reduce the number of DPD simulations needed.

The fluid of interest, the blend Miraspec UB75, was modelled using a parametrisation developed for similar surfactants. Using this parametrisation, a part of the phase diagram of a mixture of SLES and water was successfully reproduced from a qualitative point of view. This confirmed the capabilities of the DPD technique to obtain qualitative information about the microstructure of the simulated fluids. Non-equilibrium simulations were used to reproduce the rheological behaviour of the fluid under the application of shear stress. The application of the shear condition on the simulation box showed some limitations of the DPD method, regarding the explorable shear rates. It was noticed that for too high or too low values of $\dot{\gamma}$, the results of the non-equilibrium simulations are less reliable. This is common in non-equilibrium particle-based simulations, but it would be beneficial to study how to mitigate the effects of extreme strain rate conditions on the quality of the predictions. Despite this issue, it was possible to reproduce the rheological behaviour of the studied fluid. The final Δp was realistic when compared to the behaviour of similar blends in the same mixing devices. Moreover, the value of viscosity obtained from the DPD simulations resulted in remarkably good agreement with two sets of experiments conducted at different shear rates. This is noteworthy in light of the approach used for the identification of the conversion factors, which is often a weak point in non-equilibrium DPD simulations.

The results showed the feasibility of an automated multiscale approach to describe a real system that is relatively simple in terms of chemical composition, but further studies should be conducted to explore the limits of the DPD technique. Among these limitations, the most critical are the parametrisation of the molecules and the width of the explorable shear rate interval in non-equilibrium simulations. This last aspect requires particular care, as imposing a shear rate that is compatible with the physics of a real system could also lead to a more rigorous derivation of the conversion factors.

Chapter 4

Dissipative particle dynamics rheology at arbitrarily low shear rates

This chapter is based on an article written by the candidate: De Roma, F., Maffioli, L., Smith, E. R., Buffo, A., "Study of Arbitrarily Low Shear Rate Rheology Using Dissipative Particle Dynamics", *Journal of Chemical Theory and Computation*, 2026, (De Roma et al., 2026).

The rheology of complex fluids has been explored in several works using DPD (Hendrikse et al., 2023; Nafar Sefiddashti et al., 2020), generally with satisfactory results, although important limitations remain. In particular, viscosity estimates are affected by large uncertainty when shear rate is decreased (Meng et al., 2015; Prhashanna et al., 2016), whereas at high shear rates DPD simulations may display an increase in temperature and viscosity (Boromand et al., 2015), which is unphysical in many cases (Droghetti et al., 2018).

To improve the prediction of transport properties, Junghans et al. (2007) proposed an extension to the standard DPD thermostat to use the full relative velocity vector. Along the same line, increases in the dissipative coefficient γ have been investigated (Boromand et al., 2015), and *ad hoc* thermostats have been developed (Lowe, 1999; Stoyanov & Groot, 2005). The approach followed in Chapter 3 was instead centred on matching the viscosity of the DPD fluid to the corresponding real fluid, enabling a more realistic description of the system but requiring a specific set of conversion

factors. This requirement stems from the relatively high shear rates needed to obtain an acceptable signal-to-noise ratio in non-equilibrium DPD simulations. The alternative explored in this chapter aims to overcome this limitation by enabling simulations at lower shear rates. In this way, conversion factors derived from the characteristic length and time scales of the system can also be used in non-equilibrium simulations.

The chapter is organised as follows. The systems studied are described in Section 4.1, Section 4.2 shows the modifications implemented in the transient time correlation function (TTCF) approach, and Section 4.3 reports the computational details. The results obtained from the simulations are presented and discussed in Section 4.4. Finally, the conclusions are presented in Section 4.5.

4.1 Studied systems

The present work focuses on the application of TTCF to Dissipative Particle Dynamics (DPD), with a Lennard–Jones (LJ) fluid used as a benchmark. Since the DPD model requires some modification to the standard TTCF approach (see Section 4.2.1), the LJ fluid, which has been extensively studied, is used to test the correctness of the implementation and eliminate potential coding errors.

4.1.1 Lennard–Jones model

A truncated and shifted Lennard–Jones potential is used to model the fluid, resulting in a Weeks-Chandler-Anderson (WCA) potential (Weeks et al., 1971):

$$\phi(r_{ij}) = \begin{cases} 4\varepsilon \left[\left(\frac{\sigma_{\mathrm{LJ}}}{r_{ij}} \right)^{12} - \left(\frac{\sigma_{\mathrm{LJ}}}{r_{ij}} \right)^{6} \right] + \phi_c, & \text{if } r_{ij} \leq r_c \\ 0, & \text{if } r_{ij} > r_c \end{cases} \tag{4.1}$$

where r_{ij} is the distance between particles i and j, σ_{LJ} is the particle diameter, ε is the potential well, and r_c is the cutoff radius. The potential is truncated at $r_c = 2^{1/6}\sigma_{\mathrm{LJ}}$, and ϕ_c is the constant that shifts the potential to ensure the continuity of the function at the cutoff radius. To maintain consistency with previous works (Borzsák et al., 2002; Maffioli et al., 2024), the system is studied at the Lennard–Jones

triple point, with a reduced density $\rho^* = \rho\sigma_{\mathrm{LJ}}^3 = 0.8442$ and a reduced temperature $T^* = k_{\mathrm{B}}T/\varepsilon = 0.722$, with k_{B} being the Boltzmann constant. Proceeding in this way, the results can be compared with those obtained by previous works, and the implementation can be tested against a well-known system.

4.1.2 DPD simple fluid model

A detailed description of the DPD model and equations is provided in Section 2.2. Hence, the purpose of this section is to illustrate the values of the parameters used for the simulations of the DPD simple fluid analysed in this chapter. Table 4.1 reports the DPD forces parameters, the number density of beads ρ_{DPD}, the temperature T_{DPD}, the Boltzmann constant k_{B}, and the mass of the beads m. These values are consistent with those adopted in the seminal works on DPD (Español & Warren, 1995; Groot & Warren, 1997).

Table 4.1 Parameters used for the DPD simple fluid model. All the parameters are expressed in reduced DPD units.

a	γ	σ	r_c	ρ_{DPD}	T_{DPD}	k_{B}	m
25.0	4.5	3.0	1.0	3.0	1.0	1.0	1.0

Conversion factors

Identifying appropriate conversion factors is crucial for translating the results of DPD simulations into meaningful physical units of measurement. For systems in equilibrium, these factors can be directly calculated from the characteristics of the fluid modelled. Hence, if a single DPD bead represents a water molecule, a conversion factor for the length can be calculated from the approximate volume of the molecule (*i.e.* $\approx 30\,\text{Å}^3$). This value can be associated with a sphere with radius equal to the cutoff radius r_c, resulting in a length conversion factor on the order of 10^{-10} m. Analogously, the mass of a water molecule, which is approximately 3×10^{-26} kg, can be compared to the unitary mass of a bead, yielding a mass conversion factor equal to the mass of a water molecule. Various approaches can be used to derive a conversion factor for time. A possibility is to match the value of $k_{\mathrm{B}}T$ in real units with the DPD units, which is typically set to unity, to calculate the conversion factor

for energy. The next step is to use the three obtained conversion factors to derive the time conversion factor. An alternative approach is based on matching the real value of the self-diffusion coefficient of water with the one from DPD simulations (Groot & Rabone, 2001). In both cases, the resulting conversion factor for time is typically on the order of 10^{-12} s. The shear rate conversion factor is the reciprocal of the one for time and is therefore on the order of $10^{12}\ s^{-1}$. With these conversion factors, a shear rate of $\dot{\gamma} = 0.01$ DPD units provides an acceptable signal-to-noise ratio (SNR) but translates to approximately $10^{10}\ s^{-1}$ in real units. Such shear rates are not representative of conditions in industrial equipment, nor are they accessible experimentally. In rheometry experiments, the range of shear rates is usually from 10^{-1} to $10^{3}\ s^{-1}$, which corresponds to a range from 10^{-13} to 10^{-9} in DPD units. Therefore, performing simulations at lower shear rates with a high SNR is essential for studying the fluid under more realistic conditions.

4.2 Transient Time Correlation Function

To calculate the apparent viscosity as in Equation (2.26), the value of P_{yx} is averaged over many realisations, or trajectories, of the same simulation setup. This simple averaging procedure is the most common approach for calculating the shear viscosity in atomistic simulations, and it will be referred to as direct averaging (DAV) throughout this chapter. The most important drawback of DAV is linked to the inherent noise of the simulations, which can completely conceal the signal of interest, especially for small shear rates. To avoid this issue and increase the signal-to-noise ratio (SNR), high shear rates are usually applied to the system. This approach guarantees a high SNR and is suitable for Newtonian fluids, but it poses some complications when applied to non-Newtonian fluids. In many cases, the shear rate applied to achieve high SNR results is too high to be compared with experimental data or even realistic industrial applications. If the viscosity depends on the shear rate, as for non-Newtonian fluids, the results may not be representative of the real system, and extrapolation to lower shear rates may not be accurate.

An alternative approach to DAV is the transient-time correlation function (TTCF), which is a generalisation of the Green-Kubo relations (Evans et al., 2016; Evans &

Morriss, 1990), and it states that (Evans et al., 2016; Evans & Morriss, 1990):

$$\langle B(t)\rangle = \langle B(0)\rangle + \int_0^t \langle \Omega(0)B(s)\rangle \mathrm{d}s, \tag{4.2}$$

where $B(t)$ is a generic phase variable measured in the system and $\Omega(0)$ is the dissipation function evaluated at time $t = 0$, the instant at which the external field driving the system out of equilibrium is applied. The dissipation function is related to the external dissipative field applied to the system, and to the work done by this field. In the case of a sheared system with SLLOD dynamics, the dissipation function is equal to:

$$\Omega = -\frac{\dot{\gamma}V}{k_\mathrm{B}T} P_{yx}. \tag{4.3}$$

Consequently, the equation for the evaluation of the shear pressure becomes:

$$\langle P_{yx}(t)\rangle = \langle P_{yx}(0)\rangle - \frac{\dot{\gamma}V}{k_\mathrm{B}T} \int_0^t \langle P_{yx}(0)P_{yx}(s)\rangle \mathrm{d}s. \tag{4.4}$$

As shown in Equation (4.2), the TTCF formalism correlates $\Omega(0)$, a quantity computed at equilibrium, with $B(t)$, which is obtained from the non-equilibrium trajectories. In practice, the simulation procedure is based on a single equilibrium trajectory, called "mother", which is used to spawn many non-equilibrium trajectories, called "daughters". In this way, the initial conditions for the non-equilibrium trajectories are generated from the equilibrium probability distribution of the system (Maffioli et al., 2024; Todd & Daivis, 2017). The mother trajectory is then sampled to be used as the daughters' initial condition at regular intervals, which must be long enough to ensure that the starting points of different daughters are decorrelated. Moreover, decorrelation of the quantities in the non-equilibrium trajectories is a condition for the use of TTCF, which means:

$$\langle \Omega(0)B(t)\rangle \to \langle \Omega(0)\rangle\langle B(t)\rangle, \quad \text{for } t \to \infty. \tag{4.5}$$

Under this condition, the system is *mixing* and the convergence of the integral is ensured. At $t = 0$ the system is in equilibrium, hence the dissipation function $\langle \Omega(0)\rangle = 0$, and after the decorrelation time the integral does not contribute anymore to $B(t)$. Nonetheless, from a computational point of view, $\langle \Omega(0)\rangle$ is equal to zero only in the limit of an infinite number of trajectories. With a finite number of

trajectories, the integrated function will not go to zero after the decorrelation time, and the integral value will continue to grow indefinitely in time.

The most common approach to ensure that $\langle \Omega(0) \rangle = 0$ is to generate ensemble members with the same probability but different non-equilibrium trajectories from the same point in the equilibrium trajectory (Evans & Morriss, 1990). To do so, the positions and momenta of the equilibrium phase space point $\mathbf{\Gamma}_i$ are modified according to mappings that depend on the type of external field applied to the system. In the case of SLLOD with planar shear flow in the xy-plane, the following mappings are a potential choice:

$$\begin{aligned} \mathbf{\Gamma}_i &= (\mathbf{x}, \mathbf{y}, \mathbf{z}, \mathbf{p}_x, \mathbf{p}_y, \mathbf{p}_z) \\ \mathbf{\Gamma}_i^{'} &= (\mathbf{x}, \mathbf{y}, \mathbf{z}, -\mathbf{p}_x, -\mathbf{p}_y, -\mathbf{p}_z) \\ \mathbf{\Gamma}_i^{''} &= (\mathbf{x}, -\mathbf{y}, \mathbf{z}, \mathbf{p}_x, -\mathbf{p}_y, \mathbf{p}_z) \\ \mathbf{\Gamma}_i^{'''} &= (\mathbf{x}, -\mathbf{y}, \mathbf{z}, -\mathbf{p}_x, \mathbf{p}_y, -\mathbf{p}_z). \end{aligned} \tag{4.6}$$

Choosing the mappings in this way means that $P_{yx}(0) = P_{yx}^{'}(0) = -P_{yx}^{''}(0) = -P_{yx}^{'''}(0)$, hence $\langle P_{yx}(0) \rangle = 0$. Moreover, the mappings increase the efficiency of the simulations, as they allow the generation of multiple daughter trajectories from a single sample of the mother trajectory. For these reasons, most of the literature cited in the present work successfully employs the TTCF together with mappings.

4.2.1 The use of mappings with a DPD model

The main role of mappings is to ensure that the dissipation function is equal to zero at the time the external field is applied. To check whether this effect is maintained when using a DPD model, the shear pressure P_{yx} is calculated using the Virial formulation (Equation (2.27)). From Equation (4.3), the only time-dependent variable in the definition of the dissipation function for SLLOD is P_{yx}, hence $P_{yx}(0) = 0 \Rightarrow \Omega(0) = 0$. The first sum in Equation (2.27) is the kinetic term, which depends only on the velocities of the particles. Consequently, it is not directly affected by the functional form of the force field used in the simulation. Applying the mappings will then lead to a zero contribution of the kinetic term for a DPD model, as is the case for a Lennard–Jones fluid. The second sum is the configurational term, which depends on the forces acting on the particles. It is possible to show that the contribution of the conservative force $\mathbf{f}^C$ is equal to zero when mappings are applied,

since it depends only on the position of the beads. The random force $\mathbf{f}^R$ follows the same argument only if the random number ξ_{ij} is the same for the interaction between the beads i and j in all the mapped trajectories. A different result is obtained for the dissipative force $\mathbf{f}^D$, which depends on the relative velocity between the beads. In this case, the sum across the mappings of the contribution of this force to the configurational term is equal to zero only in equilibrium simulations, *i.e.* when no velocity profile is imposed on the box. When the external field is applied and the velocity profile is imposed, the following result is obtained:

$$\sum_{\text{mappings}} r_{ij,x} f^D_{ij,y} = -4\gamma\dot{\gamma} w^D(r_{ij}) \left(\frac{y_i - y_j}{r_{ij}}\right) x_i(x_i - x_j), \tag{4.7}$$

which is equal to zero only if the two beads i and j have the same x or y coordinates. In particular, from Equation (4.7), it is clear that this contribution is dependent on the imposed shear rate $\dot{\gamma}$.

The results just described are derived in more detail in Appendix B, and have been tested using simulations of Lennard–Jones and DPD models. These tests are illustrated in Figure 4.1, where the values of $|\langle P_{yx}(0)\rangle|$ are reported for different force fields. The mappings should ensure that the shear stress is zero at time $t = 0$, which is seen in the simulation results as $|\langle P_{yx}(0)\rangle| \sim O(10^{-16})$, a value effectively equal to zero within double precision machine limits.

The results of the Lennard–Jones WCA model are used as a benchmark and confirm the expected behaviour of the mappings with a value of zero to machine precision. On the contrary, for a standard DPD model ("DPD $\mathbf{f}^C + \mathbf{f}^D + \mathbf{f}^R$" in the plot), the initial value of the shear stress is considerably different from zero. This is a result of the random terms, which are unique for each daughter and so do not cancel across mappings. Therefore, using different random numbers for all daughters masks the expected dependence on the shear rate reported in Equation (4.7). The DPD model using only the conservative force, indicated with "DPD $\mathbf{f}^C$" in the figure, shows a value of zero. To further explore the influence of the random number ξ, a modified DPD model was tested in this part of the work. The model "DPD $\mathbf{f}^C + \mathbf{f}^R_{\xi_{ij}\text{ fixed}}$" in Figure 4.1 uses only the conservative and random forces, but the value of ξ is set equal for every value of random number ξ_{ij}, regardless of the beads involved in the interaction. This shows the same cancellation property across mappings and zero initial shear stress. Finally, the approach of a fixed constant random number is used

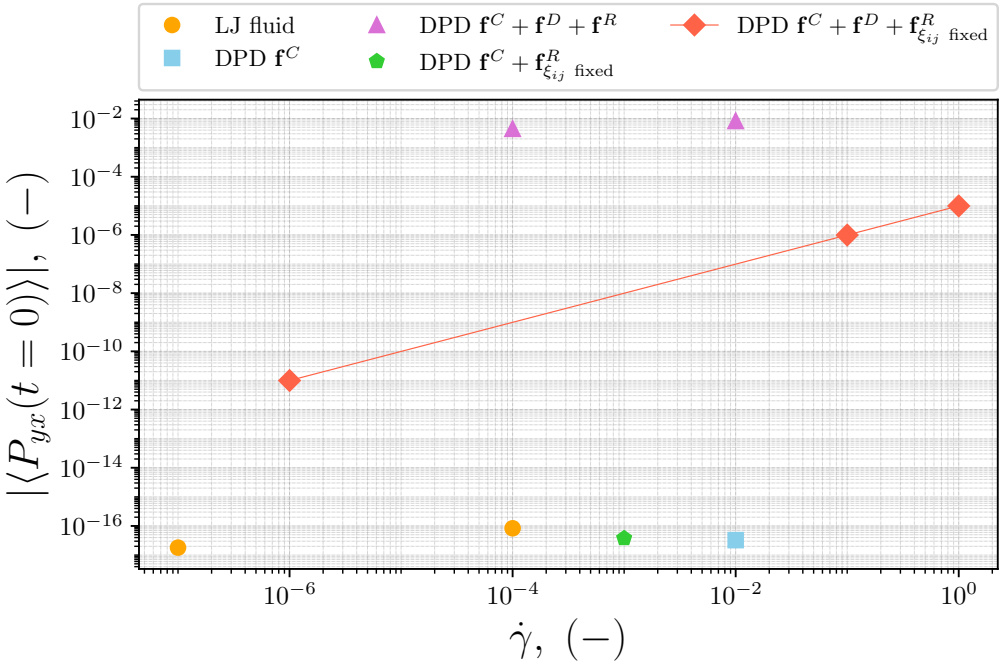

Fig. 4.1 Values of $|\langle P_{yx}(0)\rangle|$ for different models using mappings. The yellow circles refer to the LJ-WCA fluid, the purple triangles to a standard DPD model, the light blue square to a DPD model with only the conservative force, the green pentagons to a DPD model without the dissipative force and with a constant number ξ for the random force, and the red diamonds to a DPD model with the three standard forces but with a constant random number ξ. $\langle P_{yx}(0)\rangle$ can assume negative values, so its absolute value is plotted to use a logarithmic scale.

with the complete DPD force field ("DPD $\mathbf{f}^C + \mathbf{f}^D + \mathbf{f}^R_{\xi_{ij}\text{ fixed}}$" in the plot), where the initial shear stress increases together with the shear rate $\dot{\gamma}$. The simulations confirm the theoretical findings, including the dependence of the dissipative contribution of the configurational term on the shear rate. As a consequence, it is not possible to use the mappings in Equation (4.6) together with a DPD model to ensure that $\langle P_{yx}(0)\rangle = 0$. In principle, different mappings could be developed to respect the condition also for the dissipative force, but forcing the values of ξ_{ij} to be constant across the mapped trajectories poses a different problem. Enforcing this condition would require non-trivial management of the random numbers, since the interaction between bead i and bead j must use the same random number ξ_{ij} for each mapped trajectory. Setting the same random seed in each mapped daughter will not be sufficient, as the order of operations would also need to be identical. A potential solution could involve defining the same list of random numbers for each bead in each mapped trajectory and deriving ξ_{ij} from the numbers ξ_i and ξ_j in the list. Such an implementation would be complex in parallel simulations, with the added difficulty of avoiding unexpected correlations.

The alternative to the use of mappings is a modification of the TTCF formula in Equation (4.4), to take into account the finite number of trajectories. Hartkamp et al. (2012) developed this modification and applied it to a LJ-WCA fluid under mixed and elongational flow, also providing an intuitive explanation for the modification. Considering $\langle\Omega(0)\rangle \neq 0$ as an error, this error can be subtracted from $\Omega(0)$ in the integrand function, so it is possible to write:

$$\begin{aligned}\left\langle B(s)\left[\Omega(0) - \left\langle\Omega(0)\right\rangle\right]\right\rangle &= \left\langle B(s)\Omega(0) - B(s)\left\langle\Omega(0)\right\rangle\right\rangle \\ &= \left\langle B(s)\Omega(0)\right\rangle - \left\langle B(s)\right\rangle\left\langle\Omega(0)\right\rangle,\end{aligned} \tag{4.8}$$

which is equal to the covariance between $B(s)$ and $\Omega(0)$.
Consequently, the modified formula for the shear pressure becomes:

$$\begin{aligned}\left\langle P_{yx}(t)\right\rangle &= \left\langle P_{yx}(0)\right\rangle - \frac{\dot{\gamma}V}{k_\mathrm{B}T}\int_0^t\left[\left\langle P_{yx}(0)P_{yx}(s)\right\rangle - \left\langle P_{yx}(0)\right\rangle\left\langle P_{yx}(s)\right\rangle\right]\mathrm{d}s \\ &= \left\langle P_{yx}(0)\right\rangle - \frac{\dot{\gamma}V}{k_\mathrm{B}T}\int_0^t\left\langle P_{yx}(0)P_{yx}(s)\right\rangle\mathrm{d}s \\ &\quad + \frac{\dot{\gamma}V}{k_\mathrm{B}T}\left\langle P_{yx}(0)\right\rangle\int_0^t\left\langle P_{yx}(s)\right\rangle\mathrm{d}s.\end{aligned} \tag{4.9}$$

4.2.2 Error estimation

The main advantage of TTCF over DAV is the high signal-to-noise ratio that can be obtained from simulations even at very low shear rates. On the other hand, the DAV is a more straightforward method, easy to implement and to use, while the TTCF requires a more complex setup. In this context, error estimation becomes a crucial point in the choice of the method to calculate the shear viscosity. When using the formulation in Equation (4.4), the error estimation is simple and direct, since the variance of the left-hand side of the equation is equal to the sum of the variances of the two terms on the right-hand side. When using the TTCF without mappings, Equation (4.9) can be rearranged since the ensemble averages and integrals are linear operators:

$$\begin{aligned}\langle P_{yx}(t)\rangle = \langle P_{yx}(0)\rangle - \frac{\dot{\gamma}V}{k_\mathrm{B}T}\left\langle \int_0^t P_{yx}(0)P_{yx}(s)\mathrm{d}s\right\rangle \\ + \frac{\dot{\gamma}V}{k_\mathrm{B}T}\langle P_{yx}(0)\rangle\left\langle \int_0^t P_{yx}(s)\mathrm{d}s\right\rangle .\end{aligned} \tag{4.10}$$

From this equation, it is clear that the variance of $\langle P_{yx}(t)\rangle$ cannot be calculated as the sum of the variances of the three averaged variables. This is due to the product of the two ensemble averages $\langle P_{yx}(0)\rangle \left\langle \int_0^t P_{yx}(s)\mathrm{d}s\right\rangle$ in the last term.

Since a different approach is required to estimate the precision of TTCF, the bootstrap method (Good, 1999) is used in this work. This method allows the reconstruction of an approximation of the distribution of an estimator by resampling the dataset. It was described for the first time by Efron (1979) and employs resampling with replacement, which means that the same value can be sampled multiple times. In the case of TTCF, the collected data set is large enough, but the particular formulation makes the calculation of the variance impossible. In this case, it is possible to use the bootstrap method to estimate the distribution of the mean, and from this to compute its 95 % confidence interval.

For each time step, a number of samples equal to the number of trajectories is drawn from the ensemble of P_{yx} values obtained from the simulations. The mean is then calculated from the sampled dataset and the whole resampling procedure is repeated a number of times specified by the user. A distribution of the mean is then obtained and the 95 % confidence interval is calculated from this distribution. Moreover, an estimation of the standard error of the mean can be obtained from the

same distribution. A higher number of trajectories or resamples will produce more accurate results, but it can also dramatically increase the computational cost of the bootstrapping procedure.

4.3 Computational details

The TTCF formalism is implemented in the open-source Python package TTCF4LAMMPS (Maffioli et al., 2024) built on top of LAMMPS and available on GitHub[1]. The original package was modified to include the possibility of using the TTCF without mappings and add a module to perform bootstrapping on the generated data has been added. With respect to the original version, the approach without mappings requires the user to save the variable of interest, *i.e.* P_{yx}, for every time step of every trajectory. As a result, both the simulation process and the bootstrapping procedure are embarrassingly parallelisable, but the disk space required to store the data can be very large. In particular, it is proportional to the number of trajectories, the number of timesteps per trajectory, and the number of variables of interest.

For all the results presented in this work, the simulations of the Lennard–Jones WCA fluid have been performed on a system of $N = 256$ particles, with a time step of $\Delta t = 2.5 \times 10^{-3}$ in reduced units. The initial mother trajectory is run for 10000 timesteps to ensure the system reaches equilibrium, then sampled every 1000 timesteps to generate a total of 40000 daughter trajectories, each running for 600 timesteps.

The DPD simulations presented here were performed in a box with side length $L = 5$ DPD reduced units, corresponding to a total of $N = 375$ particles, considering the number density ρ_{DPD}, the conservative force coefficient a, the dissipative force coefficient γ, the random force coefficient σ, and the cut-off radius r_c reported in Table 4.1. The timestep is set to $\Delta t = 0.01$ DPD reduced units, the mother trajectory is initially equilibrated for 1500 timesteps and sampled every 100 timesteps to generate a total of 10^5 daughter trajectories, each running the sheared system for 420 timesteps. The criteria for the choice of simulation length and timestep value are illustrated, respectively, in Appendix D and Appendix E. The bootstrapping was

[1] https://github.com/edwardsmith999/TTCF4LAMMPS

performed only on the DPD results by resampling the original dataset 1200 times, with a sample size equal to the number of daughter trajectories.

4.4 Results and discussion

4.4.1 Reproduction of LJ results with and without mappings

Before using the TTCF non-mapped approach with a DPD system, its performances is assessed on an LJ-WCA fluid. Previous works studied the application of TTCF on a simple LJ-WCA fluid to compute the shear viscosity, providing a benchmark. In particular, the setup used by Maffioli et al. (2024) is reproduced here. To better understand the plot of this section, it is useful to recall that the expected viscosity for this fluid at the simulated shear rates is $\mu \sim 2.3$ - 2.4 (–) (Maffioli et al., 2024; Pan & McCabe, 2006; Todd & Daivis, 2017). Consequently, the expected value of shear pressure is $P_{yx} \sim -2.3 \cdot \dot{\gamma}$ (–).

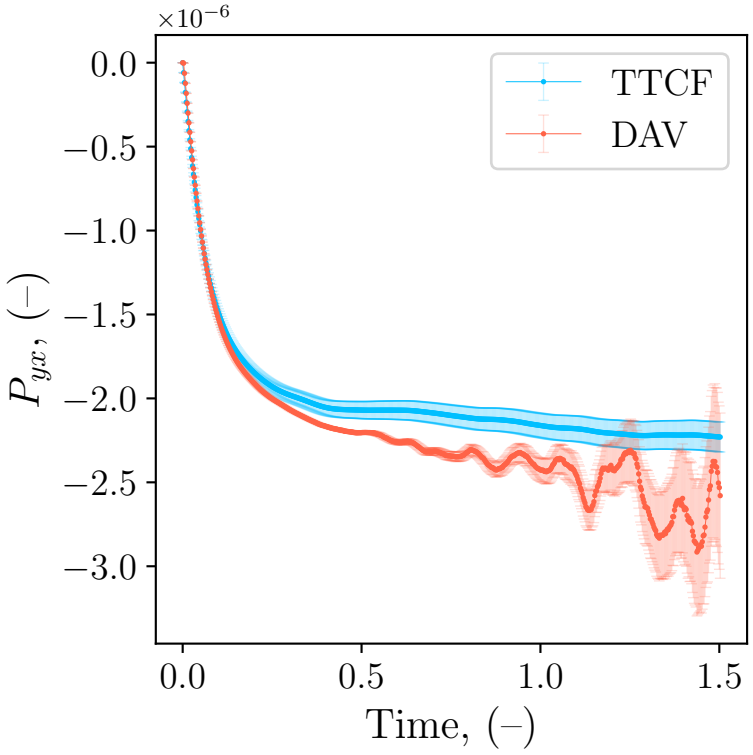

Fig. 4.2 Time response of P_{yx} for a LJ-WCA fluid with an applied shear rate of $\dot{\gamma} = 10^{-6}$ (–). Four mappings are used, the error bars are equal to the standard error.

Figure 4.2 illustrates the typical results obtained with a direct ensemble average of the trajectories (DAV) compared to the TTCF results. The use of mappings is necessary to ensure that $\langle \Omega(0) \rangle$ is equal to zero, which for a simple shear means $\langle P_{yx}(0) \rangle = 0$ (*cf.* Equation (4.3)). Additionally, the mappings lead to a reduction of the DAV's standard error in the initial phase of the non-equilibrium simulation. Hence, the DAV's error, which is zero initially due to the mappings, grows over the simulation as each daughter trajectory diverges. As $t \to \infty$, the DAV's standard error will reach a maximum value, which is related to the effective accuracy of the method. In a similar manner, it is possible to observe in the plot an increase in the TTCF's standard error, which is associated with the integration process. This means that the error will continue to grow in time without reaching a plateau, making long simulations less precise. The plot in Figure 4.2 clearly shows a higher standard error for DAV at steady state, when compared to TTCF at such low shear rates.

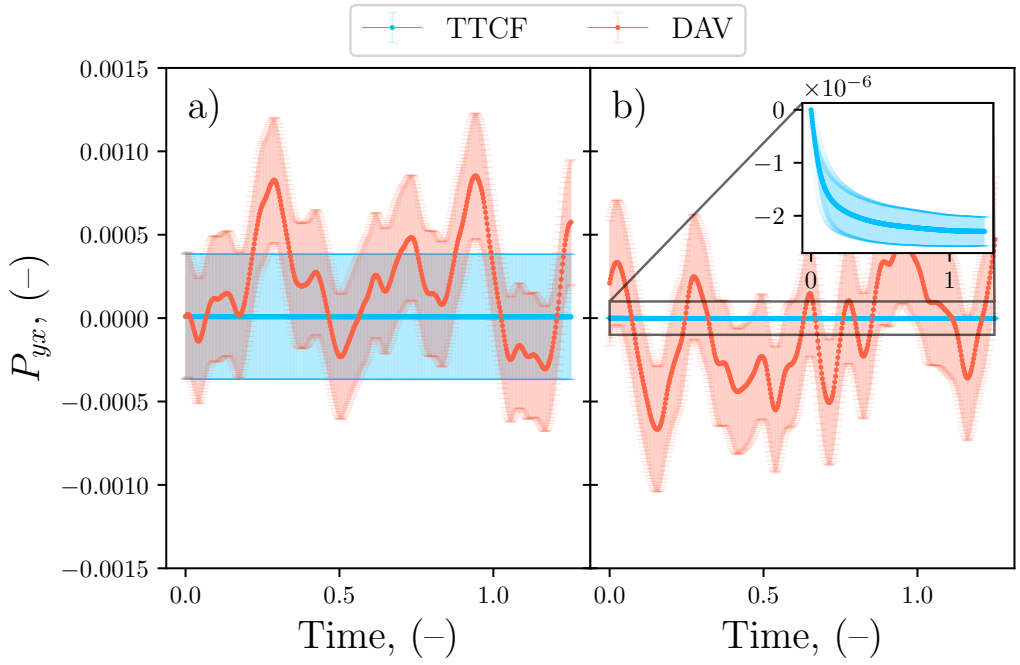

Fig. 4.3 Time response of P_{yx} for a LJ-WCA fluid with an applied shear rate of $\dot{\gamma} = 10^{-6}$ (–). Mappings are not used, and the correction in Equation (4.9) is adopted. a) The value of $\langle P_{yx}(0) \rangle$ is calculated as an ensemble average. b) The value of $\langle P_{yx}(0) \rangle$ is imposed equal to zero for the TTCF formula.

When mappings are not used, as in Figure 4.3a, the high standard error of both DAV and TTCF is visible starting from the first timestep. A comparison of the two

curves shows that the mean value of the DAV oscillates significantly more than that of the TTCF. The apparently similar standard error in Figure 4.3a is misleading, as the TTCF error is in practice orders of magnitude lower, but the high error in the plot is the result of the error at time zero introduced by the term $\langle B(0)\rangle$ in Equation (4.2), which dominates the plot. This term is still calculated as a direct ensemble average, and, consequently, it has a standard error of the same order of magnitude as the other DAV measurements. To eliminate this effect, the equilibrium condition of the mother trajectory is exploited. For a system in equilibrium $\langle P_{yx}\rangle = 0$, and at $t = 0$ the shear is applied on an equilibrium system, therefore $\langle P_{yx}(0)\rangle = 0$ is imposed in Equation (4.9). Such a procedure is applicable only when the value for a system at equilibrium is known from theory, as in the present case. Imposing this condition makes the TTCF signal unaffected by the DAV noise in $t = 0$, as shown in Figure 4.3b. Moreover, in Figure 4.3b, it is possible to compare the accuracy of DAV and TTCF for low shear rates by looking at the error bars associated with the two methods. The DAV standard error is about three orders of magnitude bigger than the signal, while the TTCF error bars indicate a much lower uncertainty, making evident the higher precision of the TTCF.

As already shown in the literature (Maffioli et al., 2024), the advantage of the TTCF reduces when the shear rate is increased. At high shear rates, the precision of the DAV becomes comparable to, or even higher than, that of the TTCF one.

The use of mappings is generally considered beneficial as the cancelling of errors between daughter trajectories, starting from the same point in phase space, is used to reduce uncertainty (Evans & Morriss, 1988). As a result, removing these mappings, as required for DPD, would be expected to perform worse than the mapped approach. The error was tested by applying a low shear rate of 10^{-6} on the LJ-WCA system and the comparison between the mapped and non-mapped approaches is presented in Figure 4.4. Surprisingly, the non-mapped approach does not exhibit a significant increase in error, and, in the tested case, even shows a small reduction. This implies the benefits of the TTCF are mainly derived from the ensemble of trajectories rather than from the use of mappings. Nonetheless, mappings remain useful, as they can generate multiple starting points without advancing the mother trajectory. For large systems or long correlation times, this is a significant computational saving since many more mappings than the four used here can be generated from a single point in time.

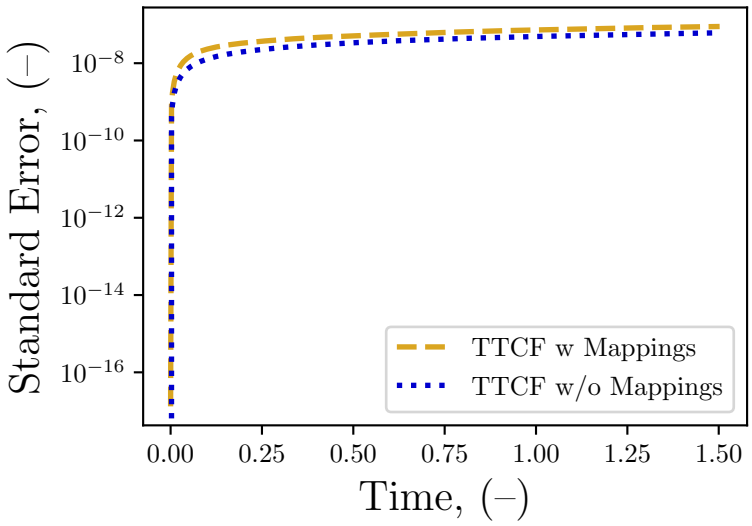

Fig. 4.4 Comparison of the standard error of P_{yx} obtained with and without the mappings using the TTCF on 4×10^4 daughter trajectories. The shear rate applied to the LJ-WCA fluid is $\dot{\gamma} = 10^{-6}$ (–).

4.4.2 DPD system

Existing data for viscosity of DPD simple fluids

Many works in the literature are focused on the use of dissipative particle dynamics to study complex fluids, whereas interest in simulating simple fluids is limited. This is most likely due to the remarkable capability of DPD to reproduce the structural properties of complex fluids and the lack of interest in simple fluids from an applicative point of view. In this work, as the methodology for applying TTCF with DPD is developed, the focus is placed on the simplest DPD fluid. Among the few works that studied the transport properties of a simple DPD fluid, a certain variability is found regarding the exact value of the viscosity. Table 4.2 recaps some of those viscosity values, which have been obtained using different methods. Among the non-equilibrium methods, standard Lees–Edwards and Müller–Plathe RNEMD are used, but also a modified version of the classic Lees–Edwards is proposed by Boromand et al. (2015). Equilibrium methods such as Green–Kubo and Einstein–Helfand are also used, since they are suitable for the calculation of the viscosity of a Newtonian fluid. Lauriello et al. (2021) focused on the evaluation of the cumulative integral of the Green–Kubo formula, while Panoukidou et al. (2021)

developed a modified version of the Einstein–Helfand method and compared it with the Green–Kubo method proposed by Jung and Schmid (2016). Given the variability obtained by previous studies, these values are intended to provide context rather than serve as reference values for the simulations.

Table 4.2 Viscosity values for a DPD simple fluid from literature. The values for Green–Kubo, Lees–Edwards, and modified Lees–Edwards from (Boromand et al., 2015) and the one from Droghetti et al. (2018) were extracted from Figure 13.c(Boromand et al., 2015) and Figure 1 of the supporting information(Droghetti et al., 2018), respectively. The other values here displayed were specified in tables or the text in the original papers together with the associated error, when reported.

Reference	Method	Viscosity μ (–)
Lauriello et al. (2021)	Green–Kubo	0.860 ± 0.002
Lauriello et al. (2021)	Einstein–Helfand	0.847
Lauriello et al. (2021)	Müller-Plathe RNEMD	0.860
Panoukidou et al. (2021)	modified Green–Kubo[a]	1.1
Panoukidou et al. (2021)	modified Einstein–Helfand	1.1
Panoukidou et al. (2021)	Lees–Edwards	1.1
Droghetti et al. (2018)	Lees–Edwards	0.85
Boromand et al. (2015)	Green–Kubo	0.871 ± 0.708
Boromand et al. (2015)	Lees–Edwards	0.871 ± 0.489
Boromand et al. (2015)	modified Lees–Edwards	0.769 ± 0.363
Boromand et al. (2015)	Poiseuille flow	0.866

[a] Modified according to Jung & Schmid (2016).

DPD without mappings

As presented in Figure 4.1, due to the presence of dissipative and random forces, the use of mappings is not enough to guarantee that $\langle \Omega(0) \rangle = 0$ for DPD systems. To consider this issue, the correction described in Section 4.2.1 is applied to the TTCF formula, and the value of $\langle P_{yx}(0) \rangle$ is imposed to be zero. Finally, the original LAMMPS implementation of SLLOD includes a Nosé-Hoover thermostat, which can interfere with the built-in thermostat of DPD. As described in Section 2.2.2, this issue can be overcome in two ways: either by modifying the LAMMPS source code, or by using `nvt/sllod` with a very long thermostat relaxation time (*i.e.* `t_damp` = 10^{30}). Both methods yield the same results, but those presented in this section were obtained using the modified version of SLLOD, `nve/sllod`, which does not apply the Nosé-Hoover thermostat.

The DPD system was investigated at different shear rates, ranging from 10^{-12} to 10^{-2} (reduced DPD units). The results of the simulations are summarised in Figure 4.5, which shows the value of the shear pressure P_{yx} divided by the shear rate $\dot{\gamma}$. Without this normalisation, the values of P_{yx} would differ by several orders of magnitude, depending on $\dot{\gamma}$, making the comparison impossible. Moreover, $-P_{yx}/\dot{\gamma}$ is equal to the viscosity, which is expected to be constant since a simple DPD fluid exhibits Newtonian behaviour. Looking at the time evolution in Figure 4.5, it is clear that the same viscosity value is reached after the transient for all studied shear rates. These curves are plotted with different shades of blue to highlight the absence of any visible trend with respect to the shear rate. The error bars reported in both plots of Figure 4.5 correspond to the 95 % confidence interval for the mean value, and they are used to assess the precision of the method. As expected, the error in Figure 4.5a increases with time, due to the error accumulated during the numerical evaluation of the integrals. This is an inherent error of the method, which can be limited either by using a more accurate integration algorithm or by reducing the number of timesteps used in the simulation. Hence, identifying the end of the transient is crucial to obtaining the lowest possible uncertainty.

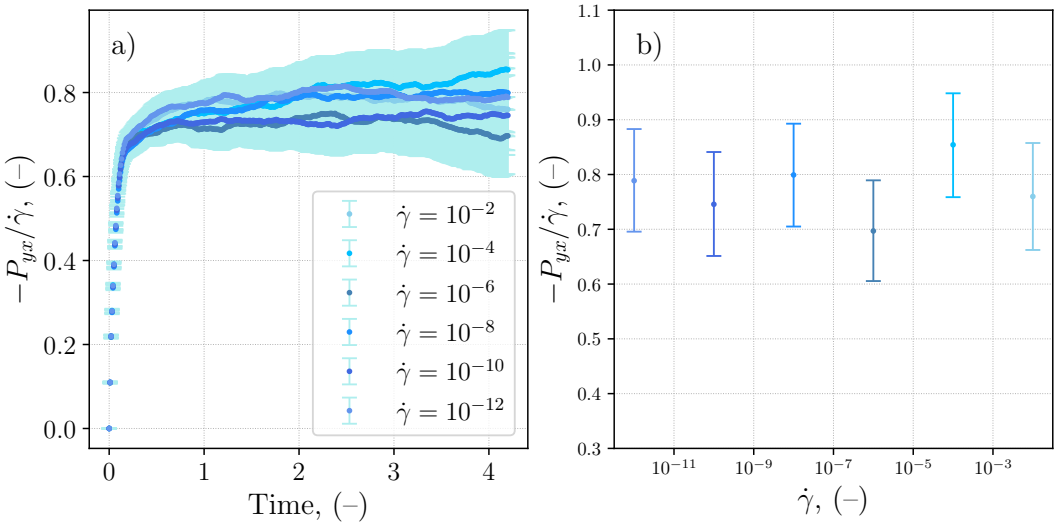

Fig. 4.5 Results obtained with the TTCF method on a DPD simple fluid: a) time evolution of the shear pressure P_{yx} divided by the shear rate $\dot{\gamma}$ for different shear rates; b) value for different shear rates at the last timestep of the simulation. The error bars represent the 95 % confidence interval for the mean value. All values are expressed in reduced DPD units.

The error bars in Figure 4.5b are the most important result obtained with the TTCF, as they show how the precision of the method is not affected by the value of the shear rate. For comparison, Figure 4.6 includes the results obtained with the DAV method, which is the standard approach to compute the shear viscosity in DPD simulations. From Figure 4.6b, it is possible to understand how DAV precision and accuracy are affected by the shear rate. When the shear rate is reduced, the DAV error bars grow dramatically, making it impossible to use the results obtained from the simulation for $\dot{\gamma} < 10^{-2}$. For the same reason, in Figure 4.6a the DAV results are shown only for the highest shear rate tested, $\dot{\gamma} = 10^{-2}$. Plotting the curves for lower shear rates would render the figure unreadable, due to the excessive noise present in DAV results. Moreover, from this plot, it is possible to notice a certain discrepancy between the DAV and TTCF time evolution. This behaviour was already observed in previous works that used LAMMPS (Maffioli et al., 2024), and it is most likely due to issues in the implementation of SLLOD in LAMMPS. The same discrepancy is noticeable in the simulations of the LJ-WCA fluid in Figure 4.2, and leads to a systematically higher value of the viscosity calculated with the DAV. Currently, this issue is being addressed by other research groups, which are working on an alternative implementation of the SLLOD algorithm in LAMMPS (Sanderson & Searles, 2025).

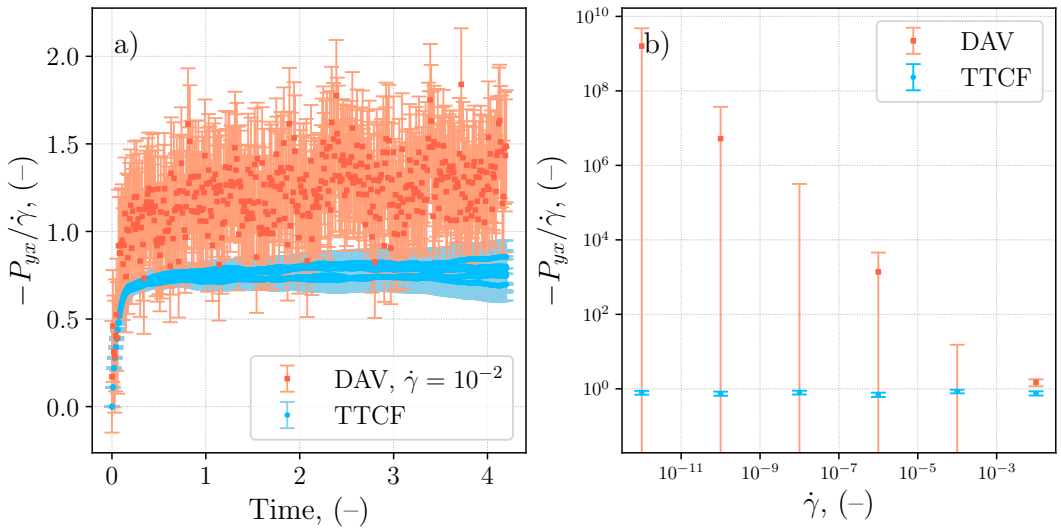

Fig. 4.6 Comparison between DAV and TTCF for a DPD simple fluid. The error bars represent the 95 % confidence interval for the mean value. a) Time evolution of the shear pressure P_{yx} divided by the shear rate $\dot{\gamma}$, DAV results are shown only for a shear rate of 10^{-2} (–). b) Value obtained at the last timestep of the simulation for different shear rates, the DAV error bars are not symmetrical due to the logarithmic scale of the y-axis. All the values are in reduced DPD units.

The increase in precision obtained through the use of TTCF is assessed more in detail using two quantities. The first is the standard error (SE), the second is a measure of the relative magnitude between the signal and the noise, indicated as signal-to-noise ratio (SNR). The SNR is calculated as:

$$\mathrm{SNR} = \frac{\langle P_{yx} \rangle}{\mathrm{SE}_{P_{yx}}}, \tag{4.11}$$

where the ensemble average of the shear pressure is divided by its standard error. Since the DAV presents too high uncertainty for low shear rates, the SNR is calculated using the mean value from the TTCF method, leading to the following expressions:

$$\mathrm{SNR}^{\mathrm{DAV}} = \frac{\langle P_{yx} \rangle^{\mathrm{TTCF}}}{\mathrm{SE}^{\mathrm{DAV}}_{P_{yx}}}; \qquad \mathrm{SNR}^{\mathrm{TTCF}} = \frac{\langle P_{yx} \rangle^{\mathrm{TTCF}}}{\mathrm{SE}^{\mathrm{TTCF}}_{P_{yx}}}; \tag{4.12}$$

The results are plotted in Figure 4.7, and show a quantitative comparison between the precision of the two methods. The DAV standard error in Figure 4.7a is constant in time, as expected, since mappings are not used. Moreover, the DAV curves collapse

on a single one, indicating a standard error that does not depend on the shear rate. The limitations of the DAV are evident, as its performance is inferior to that of TTCF in modelling $\dot{\gamma} \leq 10^{-2}$. In contrast, the TTCF standard error grows in time as a result of the numerical integration, but has the advantage of being proportional to the shear rate. This confirms the TTCF as a suitable method for arbitrarily low shear rates in DPD simulations, since it means that the SNR is constant with respect to the shear rate. The plot in Figure 4.7b illustrates this behaviour, also showing that the SNR for DAV decreases by several orders of magnitude when the shear rate is lowered.

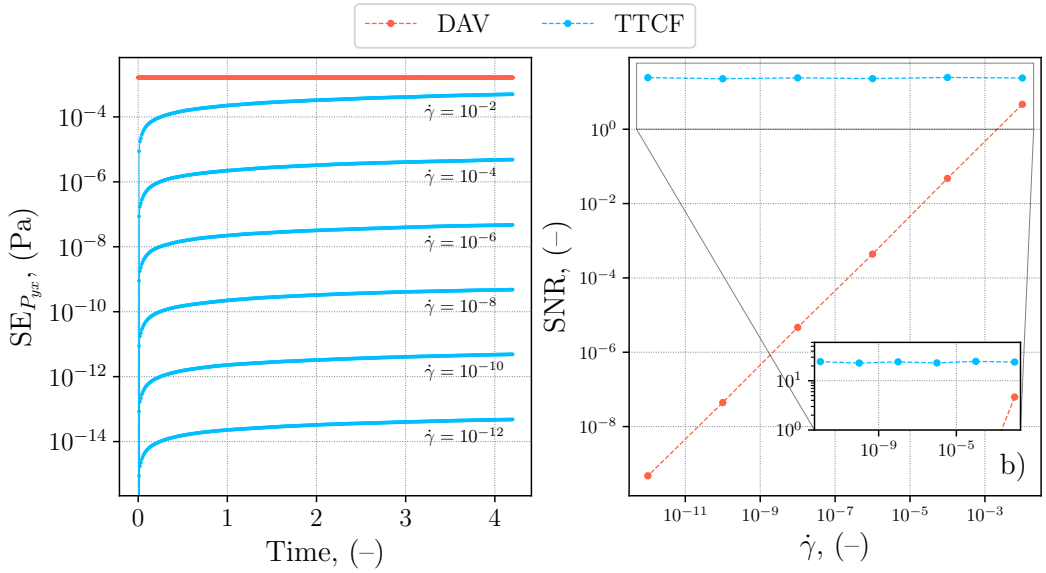

Fig. 4.7 Precision assessment of DAV and TTCF for a DPD simple fluid. a) Time evolution of the standard error (SE) for the shear pressure for different shear rates. The DAV curves collapse on a single one, while each TTCF curve refers to a different shear rate. b) Signal-to-noise ratio (SNR) for the shear pressure calculated on the last timestep, the mean value from TTCF is used as signal for both TTCF and DAV curves. All values are expressed in reduced DPD units.

Computational cost and accuracy

The use of TTCF requires a large number of independent simulations, since it is based on the evaluation of the transient. On the other hand, each simulation does not usually require a large number of timesteps, depending on the decorrelation time of $\Omega(0)$ and $B(t)$. As reported in Section 4.3, 10^5 trajectories have been simulated and averaged over 420 timesteps for each value of the shear rate. The management of such a high

number of simulations was possible using the Python package TTCF4LAMMPS, modified to include the non-mapped approach. The simulations were performed on a cluster, using 120 cores over approximately half an hour of wall time, equal to about 63 core hours, for each shear rate. The bootstrap method was parallelised on the same number of cores, and the time necessary to evaluate the standard error was negligible compared to the simulation time, as reported in Table 4.3.

Table 4.3 Computational time to perform simulations and bootstrapping for different shear rates.

$\dot{\gamma}$ (–)	Simulation time (s)	Bootstrap time (s)
10^{-2}	1850	48
10^{-4}	1861	48
10^{-6}	1898	46
10^{-8}	1890	46
10^{-10}	1859	45
10^{-12}	1880	47

The study of a DPD simple fluid has some advantages from the computational point of view, since in such systems the decorrelation time is short. This is due to the absence of microstructures, which, depending on the type of structure, can increase the time for the stresses in the fluid to relax. For this reason, the simulations were carried out on a small system of 375 particles, which resulted in a relatively high uncertainty for both TTCF and DAV. This is noticeable both in Figure 4.5b and in Figure 4.7b, where the confidence interval for the mean value is still quite large and the TTCF SNR is below one. The present work is focused on illustrating how to apply the TTCF method to DPD systems and to highlight the advantages with respect to the DAV. Hence, the absolute value of SNR is not the main focus, but rather the fact that it is constant with respect to the shear rate.

It is possible to increase the accuracy of the TTCF method by either *i*) considering a large system or *ii*) increasing the number of independent trajectories to be averaged. The first approach is often necessary for studying complex fluids, where the size of the microstructures imposes the size of the box. This must be large enough to be representative of the system. Increasing the system size is computationally more expensive, but usually increases the SNR. The second approach allows for an increase in the computational cost and precision of the method with more granularity. However, in some cases, a large number of independent trajectories is necessary to significantly improve the SNR.

4.5 Conclusions

This chapter presented the application of the transient time correlation function (TTCF) method to DPD simple fluids, to perform shear simulations at arbitrarily low shear rates. It is shown that the TTCF can be successfully applied to simple DPD systems, allowing for the calculation of shear viscosity at shear rates as low as 10^{-12} without losing precision on the results.

To assess the performance of TTCF, its results were compared with the direct ensemble average (DAV), which is the standard approach for calculating shear viscosity. As expected, the DAV method showed an SNR that decreases with lower shear rates, making the error too high for the DAV to be useful at shear rates below 10^{-2} (−). On the other hand, the TTCF method was able to provide accurate results for each tested shear rate with a lower error than the DAV and an SNR that remains constant with respect to the shear rate. The more straightforward DAV method resulted reliable only for high shear rates, which usually do not correspond to replicable conditions in experiments.

The TTCF method could not be applied directly, and it was necessary to adapt it to account for the DPD force field. The presence of the DPD thermostat required a modification of the SLLOD algorithm implemented in LAMMPS, to avoid interference of the Nosé-Hoover thermostat with the DPD one. Moreover, it was demonstrated that the dissipative and random forces, the core of the DPD thermostat, break the symmetry imposed by the mappings. Mappings are no longer sufficient to guarantee that the dissipation function $\langle\Omega(0)\rangle$ is equal to zero at the initial time, and a correction to the TTCF equation becomes necessary. The revised formulation, already proposed by previous works, allows the calculation of the apparent viscosity for a DPD simple fluid, but makes it more complex to estimate the error. To overcome this issue, the bootstrap method was used to estimate the distribution of the mean value, and to recover from it the 95 % confidence interval. The increase in computational cost due to the bootstrapping procedure was negligible compared to the simulation time due to the high parallelisability of the method. A key outcome of this study is that the use of mappings is not practical with DPD. Remarkably, their absence does not compromise the accuracy of TTCF results and can even lead to improved precision.

The results presented open the possibility to study the rheology of structured fluids using DPD in combination with TTCF without the high shear rate limitations of the direct averaging. In this way, simulations that match the experimental conditions could be performed with conversion factors derived from the characteristic time and length scales of the system. Crucially, the deformation of the microstructures under shear flow could be studied under realistic conditions, avoiding unphysical behaviour due to extremely high shear rates. Studies on such complex systems will also be helpful in identifying the limitations of the method, which are often influenced by system–specific properties, such as the stress relaxation time.

Chapter 5

Computational Fluid Dynamics modelling of unbaffled stirred tanks

This chapter includes data obtained through collaborations with colleagues from the *Università di Bologna* and the *Università di Napoli*. The experimental power and PIV measurements in the stirred tank were carried out at the *Università di Bologna*, whereas the rheometry experiments used to develop the viscosity models (except the GPR-based model) were performed at the *Università di Napoli*.

The study of unbaffled stirred tanks has always attracted less attention from the scientific and industrial community. This is a direct consequence of their poorer mixing performance compared to baffled vessels (Scargiali et al., 2013). Baffles break the circular flow generated in the tank, improving mixing in both the radial and axial directions. Their absence leads to a strong tangential flow, which deforms the free surface of the liquid, generating a vortex that can entrain air into the system (Busciglio et al., 2013; Nagata et al., 1975). Two different fluid dynamics regimes can be observed based on the relative position of the impeller and the vortex. For low impeller speeds, in the subcritical regime, the vortex is located above or at the level of the impeller, while in supercritical condition the vortex overcomes the impeller planes. This latter regime is characterised by air entrainment and bubble injection into the liquid, and it is achieved at higher impeller speeds (Scargiali et al., 2013).

The supercritical regime has been found to increase the mixing efficiency of unbaffled stirred tanks to the efficiencies of baffled vessels (Busciglio et al., 2014).

Nonetheless, unbaffled systems have attracted increasing interest in recent years. This is due to their advantages in specific applications, where shear stress must be limited, as is the case with sensitive biological fluids (Scargiali et al., 2014). The presence of baffles can also be undesirable during crystallisation (Hekmat et al., 2007) and precipitation (Kagoshima & Mann, 2006), because particle impact and friction near the baffles are difficult to control. Baffled systems are more prone to incrustation formation, making them less suitable for the standards required by the food and pharmaceutical industries (Assirelli et al., 2008). Furthermore, for highly viscous fluids under laminar or transitional regimes, baffles are not necessarily beneficial (Scargiali et al., 2014). They may promote dead zones near the vessel wall and can even increase blend times at sufficiently low Reynolds numbers (Etchells & Hesketh, 2023; Scargiali et al., 2014). The potential advantages of unbaffled configurations motivate this chapter, which focuses on power consumption and the velocity field in an unbaffled stirred tank. A comparison with a twin experimental setup is performed to assess the accuracy of the model. The fluid studied in these systems is Pluronic L64, whose complex rheology has been modelled using both conventional viscosity models and a GPR model. In particular, the latter required a simplified computational approach, limiting the study to trends and qualitative insights.

The chapter is organised as follows: the fluids studied and their rheological models are presented in Section 5.1, Section 5.2 describes in detail the computational macroscale model and its coupling with the GPR viscosity. The results obtained from the simulations, the comparison with experimental data, and the performance of the GPR – CFD approach are presented in Section 5.3. Finally, the conclusions are reported in Section 5.4.

5.1 Poloxamers

Poloxamers are a class of polymers developed by the chemical company BASF (Badische Anilin- und Soda Fabrik) and are commercially known as Pluronics. These molecules are non-ionic triblock copolymers, which follow the chemical structure shown in Figure 5.1. From this structure, it is possible to identify two polyethylene oxide (PEO) chains at the ends of the molecule and a central core of polypropylene

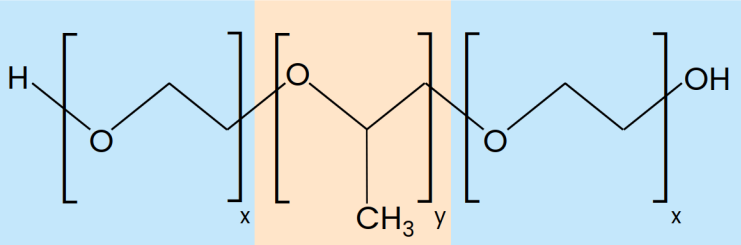

Fig. 5.1 General chemical structure of a poloxamer, the hydrophilic ethylene oxide group is highlighted in light blue, while the hydrophobic propylene oxide group is highlighted in light orange.

oxide (PPO). While the PEO segments are hydrophilic, the PPO inner part exhibits hydrophobicity, giving the molecule an amphiphilic character. The possibility to vary the relative length of these two segments makes poloxamers adaptable to many different applications. For this reason, these fluids find their industrial applications in diverse sectors, from personal care to the pharmaceutical sector.

The amphiphilicity is also responsible for self-assembly into different microstructures depending on the polymer concentration in an aqueous solution. In structured fluids, the different spatial arrangements of the molecules in these microstructures influence the response to flow condition, and hence the rheological behaviour (Larson, 1999). Pluronics are classified according to the molecular weight of the PPO segment, the weight fraction of the PEO segment, and the physical state at room temperature (flake, paste, or liquid) (Khimani et al., 2020). In this way, these polymer molecules can be placed in a matrix that provides information about their size and the PPO/PEO ratio (Alexandridis & Alan Hatton, 1995).

The fluid analysed in this chapter is Pluronic L64, which is found in the liquid state and has an exact chemical structure with x = 14 and y = 31, where x and y refer to the number of repeating groups reported in Figure 5.1. The phase diagram and rheology of this Pluronic have been extensively studied experimentally (Pasquino et al., 2019) and computationally (Droghetti et al., 2018; Prhashanna et al., 2016).

5.1.1 Rheology of Pluronic L64

The rheological behaviour of a mixture of Pluronic L64 (PL64) in water is influenced by the composition and the temperature. Depending on these variables, the mixture is found in different phases, which correspond to various microstructural configurations.

The microstructures respond in different ways under the effect of a stress, resulting in different viscosity values, or even different rheological behaviour. Figure 5.2 reports the phase diagram for PL64 in water, showing how the transition between the various phases depends on both temperature and polymer concentration. In this figure, the phases of interest are highlighted with different colours and correspond to a micellar phase (L1), a hexagonal phase (E), and a lamellar phase (L2). In general, increasing

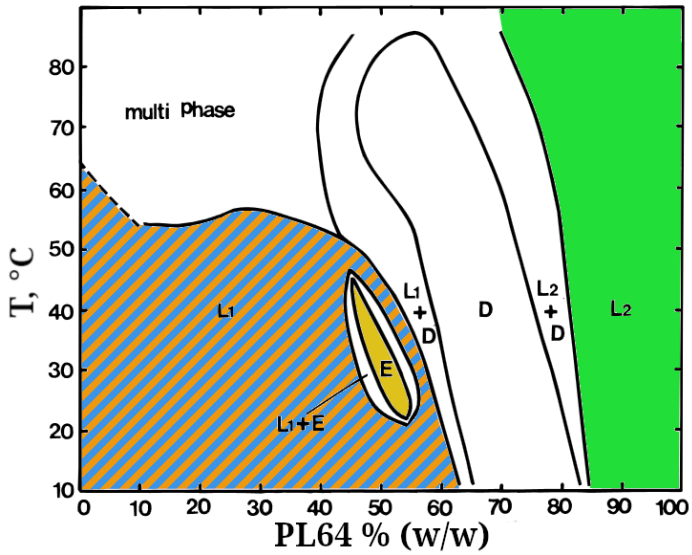

Fig. 5.2 Phase diagram for a mixture of Pluronic L64 in water adapted from Alexandridis et al. (1996). The different regions indicate different phases and the ones relevant to this chapter are highlighted with colour. The L1 region is coloured with blue and orange stripes, and corresponds to a micellar phase, typical of the blends P40 and P50M. The E region, highlighted in dark yellow, is the hexagonal phase, characteristic of the P50H mixture. The region L2, coloured in bright green, is the lamellar phase.

the concentration of polymer leads to an increase in viscosity, but when the fluid is in certain conditions it behaves as a non-Newtonian fluid.

Viscosity values for the PL64/water blends studied in this chapter are reported in Table 5.1, differentiating the Newtonian cases from the other ones. The same table also illustrates the short name, or mixture ID, for different composition and phase conditions. These short names are composed of the letter P, which stands for Pluronic, followed by the percentage by weight of the polymer in the mixture. An additional letter is used to discriminate between two blends that contain the 50 % (w/w) PL64, but exhibit different rheological behaviours. For this concentration, a phase transition is visible in Figure 5.2 between 25 and 30 °C, and the microstructures rearrange

Table 5.1 Viscosity values for PL64 in water at different concentrations.

Mixture ID	PL64 % (w/w)	T, °C	ρ, kg m^{-3}	μ, Pa s
P100	100	24	1050	non-Newtonian
P50H	50	32	1025	non-Newtonian
P50M	50	24	1025	0.442
P40	40	26	1020	0.125

from a micellar (P50M) to a hexagonal (P50H) configuration. The micellae grow, mutating from a spherical shape to a rod-like one, organising in a more ordered structure. The P50 was tested at two different temperatures: 24 °C, which is below the phase transition temperature, and 32 °C, which is above that temperature. As a result of this transition, the viscosity of the P50H is remarkably higher, and its value becomes a function of the shear rate $\dot{\gamma}$. Rheological experimental data for the P50H have been obtained at different shear rates, and interpolated using a power-law:

$$\mu = k\dot{\gamma}^{n-1}, \tag{5.1}$$

where k is the consistency index and n is the flow behaviour index.

The experimental results and the fitted viscosity law are illustrated in Figure 5.3a. In this figure, the shear thinning behaviour of P50H is evident, with a decrease in viscosity of two order of magnitude as the shear rate increases from 0.1 to 100 s^{-1}. A power-law function does not impose any limit to the values of viscosity, resulting in an infinite viscosity fluid at very low shear rates and an inviscid one at very high shear rates. This behaviour does not reflect the real fluid features and can also rapidly lead the simulation to diverge and stop due to numerical errors. For this reason, the μ calculated with the power-law for the P50H is limited, and can vary between 5 and 254 Pa s. A shear thinning behaviour is also characteristic of P100, the pure Pluronic L64, which is a polymer melt. In this case, the data and the fitted rheology law are illustrated in Figure 5.3b, which shows a more contained variation in the value of μ. A Bird–Carreau model can be used to interpolate these data:

$$\mu = \mu_\infty + (\mu_0 - \mu_\infty)[1 + (\lambda\dot{\gamma})^2]^{\frac{\alpha-1}{2}}, \tag{5.2}$$

where μ_0 is the zero-shear viscosity, μ_∞ is the viscosity at infinite shear, λ is a time constant, and α is the power index.

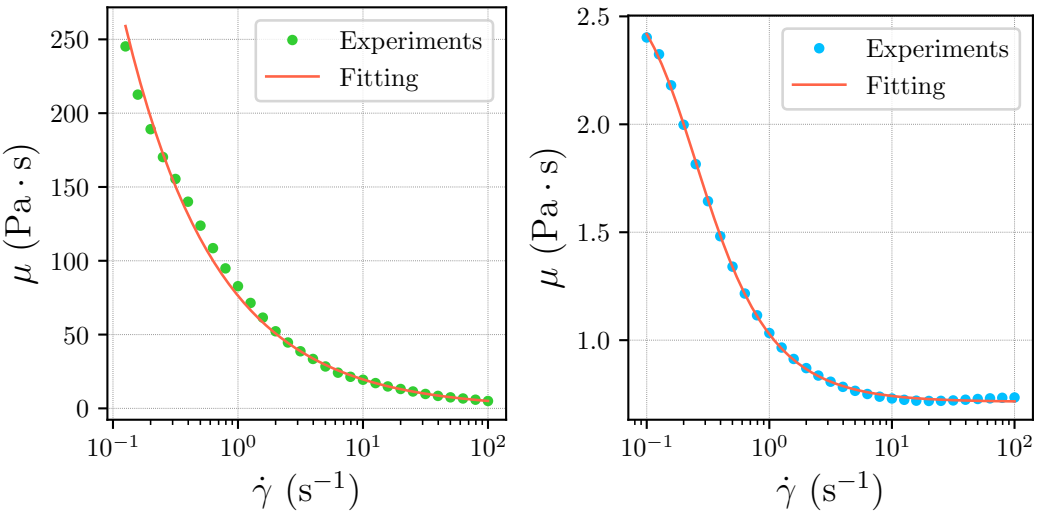

(a) P50H data and power-law fitting.

(b) P100 data and fitting with Bird–Carreau.

Fig. 5.3 Experimental rheometry data for non-Newtonian blends and viscosity models resulting from the interpolation procedure.

The values of the parameters of the rheology models used for the non-Newtonian blends can be found in Table 5.2. The mixtures of PL64 and water at 40 % and 50 % at 24 °C show a constant viscosity for different shear rates, hence are classified as Newtonian. In these cases, the fluid is found in a micellar phase, and the viscosity increases with the polymer's concentration, as reported in Table 5.1.

Table 5.2 Parameters obtained from the fitting of experimental rheometry data for P50H and P100.

	Parameter	Value	Units
Power law	k	76.3	Pa s^n
	n	0.41	-
Bird–Carreau	μ_0	2.68	Pa s
	μ_∞	0.71	Pa s
	λ	5.48	s
	α	0.41	-

GPR model for PL64 rheology

In addition to the rheological models illustrated in the previous section, a Gaussian Process Regression (GPR) model was developed for the L64/water mixture. The

purpose of this model is to extend the coupling described in Chapter 3 to include the dependence of viscosity on fluid composition. No extended dataset was available for the mixture under the temperature conditions investigated in the stirred tank experimental campaign. Consequently, the focus of this part of the work shifts from direct reproduction and validation against experiments to the improvement of the coupling method.

The GPR model was trained using a preliminary dataset covering a wider range of polymer concentrations C, from pure water to 90 % by mass of PL64 in water. The data were obtained from Pasquino et al. (2019), where rheometry experiments were conducted by varying the shear rate from 0.1 to 100 s^{-1} at a temperature of 30 °C. The training dataset is shown in Figure 5.4a and the results sampled

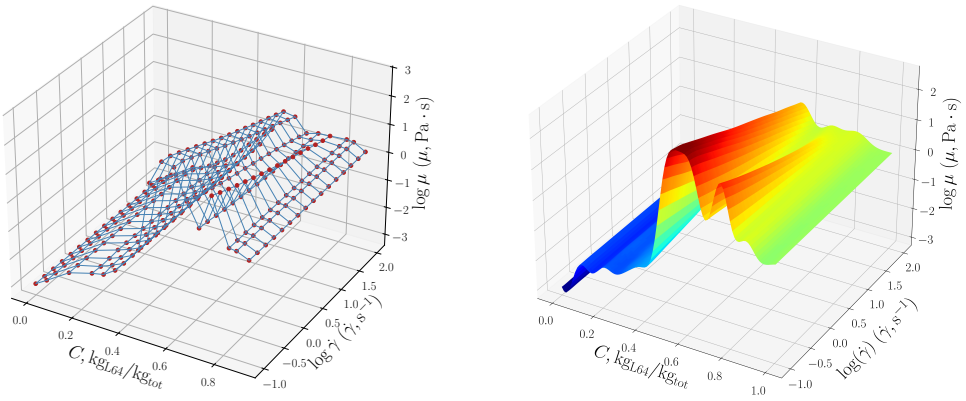

(a) Rheometry data.

(b) GPR model.

Fig. 5.4 Pluronic L64 rheometry data and resulting GPR model, the data are collected for different concentrations C and at different shear rates $\dot{\gamma}$.

from the GPR model are reported in Figure 5.4b. From the rheometry data, it is possible to identify an interval at low L64 concentration in which the mixture has a constant viscosity, corresponding to the micellar phase. As the polymer concentration increases, the system undergoes the phase transitions reported in Figure 5.2, and displays pronounced non-Newtonian behaviour, with a viscosity peak observed at $C = 0.55\,\mathrm{kg_{L64}/kg_{tot}}$. At higher concentrations, the blend is found in a lamellar phase, still characterised by a shear-thinning behaviour but with a viscosity that slightly decreases with C.

The uncertainty associated with the GPR model is depicted in Figure 5.5 and is higher in regions where the data are sparse. This effect arises from the non-

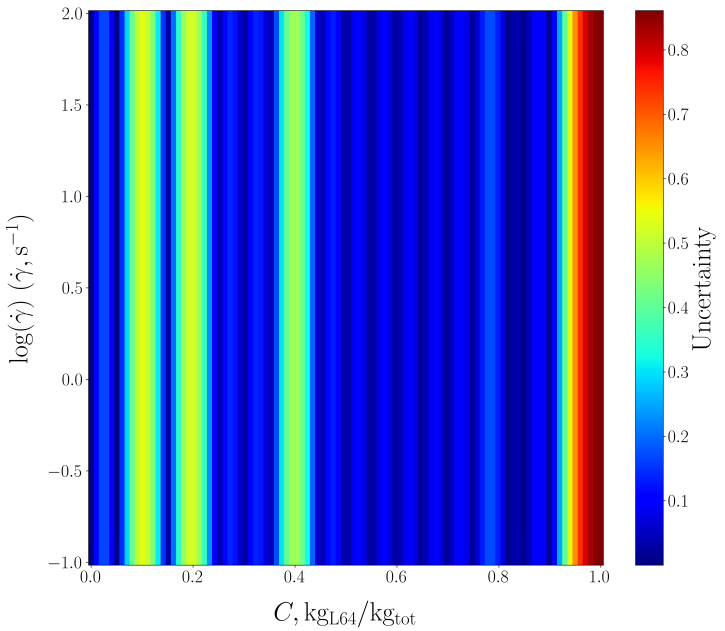

Fig. 5.5 Uncertainty in output for the GPR model depending on the PL64 concentration C and the shear rate $\dot{\gamma}$.

uniform sampling of polymer concentration over the interval from 0 to 1 $\mathrm{kg_{L64}/kg_{tot}}$. Moreover, it confirms that the GPR's uncertainty increases when the predictions are made outside the training data range, as for $C > 0.90\,\mathrm{kg_{L64}/kg_{tot}}$.

5.2 Computational model

The system studied is an unbaffled stirred tank with elliptical bottom, equipped with standard Rushton turbine. The dimensional features of the computational domain are identical to those of a 10 L experimental vessel, and they are reported in Table 5.3. These are also shown in a schematic representation of the equipment in Figure 5.6a. The correspondence between the equipment used for experiments and the CFD domain allows the direct comparison of the results. Based on this agreement, it is possible to assess both the accuracy of the CFD and the quality of the experimental measurement method. The computational domain is obtained using the open-source software Blender (version 3.5) which includes a Python interface. A small Python module was developed, to automatically generate the geometry of a stirred tank in STL (standard tessellation language), starting from the dimensional features and

Table 5.3 Dimensional features of the computational domain.

Parameter	Value, m
T_d	0.230
D	0.0767
H	0.202
C_d	0.101
B_d	0.060

some descriptors. Parameters like the presence of baffles, the type of bottom, and the type and position of the impeller are inserted as input data. The software can be extended to add different geometries or impeller types, and can be found on GitHub[1]. The result of the generation is shown in Figure 5.6b, where the side walls and the elliptical bottom are cut to make visible the impeller and the shaft.

To account for the effect of impeller rotation, a Multiple Reference Frame (MRF) approach is employed in all the steady-state simulations for the evaluation of N_p and velocity fields (Sections 5.3.1 and 5.3.2). The MRF approach is primarily suited to steady or quasi-steady simulations, since the impeller is kept fixed in space and its rotation is represented through the governing equations in a rotating reference frame rather than through an actual motion of the mesh. Therefore, MRF does not resolve blade-passing effects or the true time-dependent motion of the impeller.

For the transient simulations using the GPR-based viscosity model (Section 5.3.3), a sliding mesh approach (Bakker et al., 1997) was initially tested. However, this approach was subsequently abandoned because of its prohibitive computational cost. Sliding mesh simulations are intrinsically more expensive than MRF simulations and, in the present case, the coupled transient problem required the use of a low Courant number, further increasing the computational time. For the same reasons, sliding mesh simulations could only be performed on a very coarse mesh, which compromised the reliability of quantitative results. Moreover, no experimental data are available under the thermodynamic conditions covered by the GPR training dataset.

Consequently, the transient simulations are used exclusively to assess the robustness and functionality of the proposed coupling strategy, rather than to provide quantitative predictions. In these simulations, the transient term is retained to resolve

[1] https://github.com/mulmopro/autoCSTR

the temporal evolution of the scalar field and the resulting changes in local viscosity and velocity. The MRF approach is therefore used as an approximate treatment of the flow field induced by the impeller during the coupled scalar–momentum calculation, not as a method to resolve the physical rotation of the impeller. This approximation is considered acceptable for the present qualitative analysis, especially because the vessel is unbaffled and the blade–baffle interaction is therefore absent. Nevertheless, a sliding mesh approach would be more appropriate from a physical standpoint for mixing prediction or evaluation of time-resolved effects related to blade passage.

The MRF region corresponds to a cylindrical zone with a radius equal to 60 % of the tank radius and a total height equal to four times the impeller blade height. This region is highlighted in orange in Figure 5.6a.

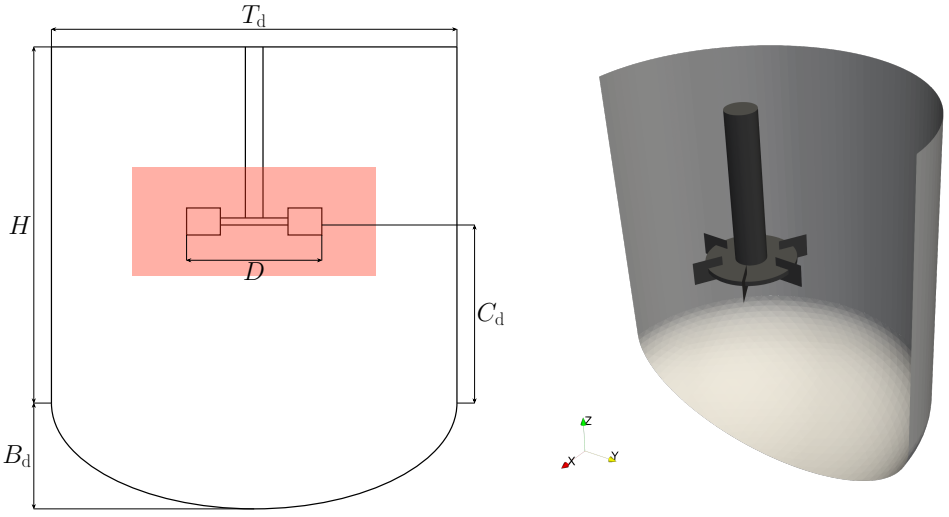

(a) Stirred tank dimension (see Table 5.3). (b) Clipped 3D representation of the stirred tank.

Fig. 5.6 Model for the computational domain of the stirred tank. The highlighted orange zone in (a) represents the MRF zone.

The comparisons between experiments and CFD are focused on the power number N_p and the velocity field inside the equipment. The power number is a dimensionless number that relates the power consumed by the impeller to the power require to set the fluid in motion. N_p for stirred tanks is calculated as:

$$N_p = \frac{P}{\rho N_r^3 D^5}, \tag{5.3}$$

where P is the power drawn at the impeller, ρ is the density of the fluid, N_r is the impeller speed measured in revolutions per second, and D is the diameter of the impeller. The power number depends on the Reynolds number, and on the geometrical features of the system, like the presence of baffles, and the type and dimensions of the impeller (Hemrajani & Tatterson, 2003). $\mathrm{N_p}$ is usually studied at various Reynolds numbers, which, for a stirred tank is defined as:

$$\mathrm{Re} = \frac{\rho N_\mathrm{r} D^2}{\mu}, \tag{5.4}$$

where μ is the dynamic viscosity of the fluid. For the non-Newtonian mixtures, the Reynolds number is calculated using the apparent viscosity of Equations (5.1) and (5.2) at the average shear rate in the impeller region. The latter can be estimated using the Metzner–Otto relation (Hemrajani & Tatterson, 2003)

$$\dot{\gamma} = K N_\mathrm{r}, \tag{5.5}$$

where N_r is the impeller speed and K is the Metzner–Otto constant. This relation is valid for shear-thinning fluids in laminar regime and derives from the study by Metzner and Taylor (1960). The value of the Metzner–Otto constant is chosen equal to 11, which is in the range of the recommended one for high-speed impellers. The correlation between $\mathrm{N_p}$ and Re has captured the interest of the community for long time, with a higher focus on baffled systems with different impellers (Rushton et al., 1950). Recently, the renewed attention in unbaffled stirred tanks led to the development of correlations for the power number in these systems (Scargiali et al., 2017; Scargiali et al., 2013).

In CFD simulations, the power at the impeller can be calculated either from the moment of the forces in the z direction, or using the viscous dissipation rate. In the first case, the power can be calculated using the following equation:

$$P = 2\pi N_\mathrm{r} M_z = \omega M_z, \tag{5.6}$$

where ω is the angular velocity in rad/s and M_z is the moment in the z direction acting on the impeller and the shaft. It must be reminded that the value of the moments on the static walls of the stirred tank should be the same acting on the rotating parts, in order for the system to be in equilibrium. Alternatively, it is possible to calculate the

power from the average viscous energy dissipation rate ϵ, defined as:

$$\epsilon = \nu \dot{\gamma}^2, \tag{5.7}$$

where ν is the kinematic viscosity of the fluid and $\dot{\gamma}$ is the magnitude of the rate-of-strain tensor $\dot{\boldsymbol{\gamma}}$. This latter has already been defined it Equation (2.6) and its magnitude is obtained through the double dot product, as reported in Equation (2.7). After the evaluation of the viscous dissipation rate, the power number is still calculated following Equation (5.3), where the power P is equal to

$$P = \rho \epsilon V = \rho \nu \dot{\gamma}^2 V, \tag{5.8}$$

with V volume of the fluid. Both Equation (5.6) and Equation (5.8) have been taken into account to perform the grid dependence study (Section 5.2.1), while the results presented in Section 5.3.1 are calculated using the moments on the rotating and static walls, as in Equation (5.6).

The study here presented is centred around the behaviour of fluids with high viscosity, with the underlying assumption of systems in laminar regime conditions. For this reason, a laminar transport model was employed for all simulations performed. The operating conditions are varied through the impeller speed N_r, whose value ranges from 102 to 502 RPM. These correspond to a tip velocity v_tip that spans from 0.41 to 2.02 m s^{-1}. Different mixtures are used in combination with the same impeller's speed, to reproduce different Reynolds numbers, in the interval between 0.76 and 400. Looking at these values, the laminar regime assumption will surely hold for the most viscous fluids, which are at low Re. On the contrary, it must be verified for less viscous mixtures, when the system will have a higher Reynolds number value.

5.2.1 Grid dependence study

The computational grid, or mesh, is generated using *snappyHexMesh*, a meshing tool included in OpenFOAM. The mesh is based on an o-grid approach, as visible in the detail of Figure 5.8, where the central square shape has been modified to smooth the transition to the external circular zone. Beside the inner core of the o-grid, an additional level of refinement is imposed on the radial direction, on a zone up to the

60 % of the vessel's radius, as in Figure 5.7b. Another refinement is also imposed along the axial direction, *i.e.* z, centred in correspondence of the disk of the Rushton turbine and symmetrical with respect to the impeller position. The height of this refinement zone is a parameter, and for the simulations presented in this chapter it was specified as four times the height of the impeller's blades. Figure 5.7a illustrates the refinement in both directions, emphasising their overlap in a central cylinder that corresponds to the zone where MRF is active.

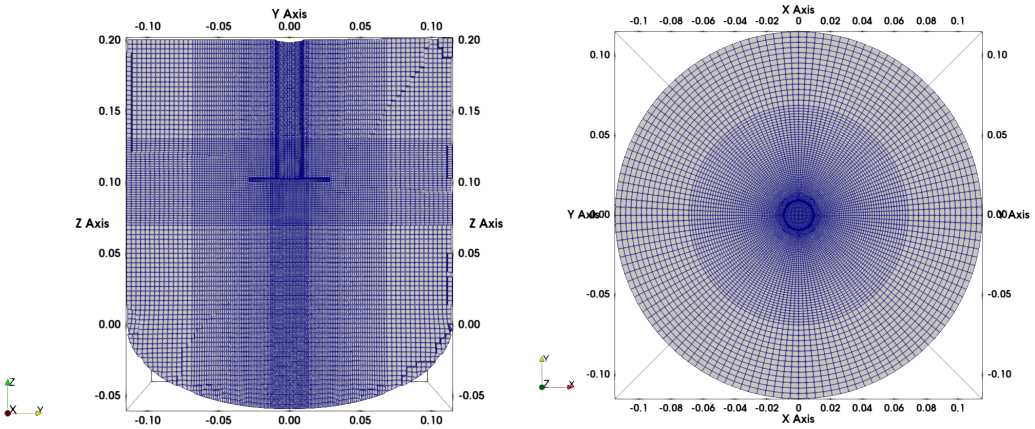

(a) Front view, orthogonal to x direction. (b) Up view, orthogonal to z direction.

Fig. 5.7 Computational mesh for the stirred tank model.

Starting from a base mesh, the cell densities in radial, axial, and circumferential directions have been increased using a multiplicative factor, to find a grid independent solution. This factor is equal to 1.26, and has been chosen to obtain a number of cells that is roughly the double every time that a finer mesh is generated, with respect to the previous level of refinement. The cell densities and the respective total number of cells are reported in Table 5.4 for all the tested grids. The monitored parameter is the power number N_p, which has been calculated using the moments in the z direction on the rotating and the static parts, and using the laminar viscous dissipation rate. The grid dependency study is carried out on a laminar Newtonian case, on the mixture at 50 % (w/w) of Pluronic L64 in water, at a Reynolds of about 60.

The results of this study are illustrated in Figure 5.9. This shows a substantial independence of the power number calculated with the moments on both static and rotating walls, with respect to the number of cells. On the other hand, the value of N_p calculated from the viscous dissipation rate settles only for meshes with a certain number of cells. This number is equal to the number of elements corresponding to

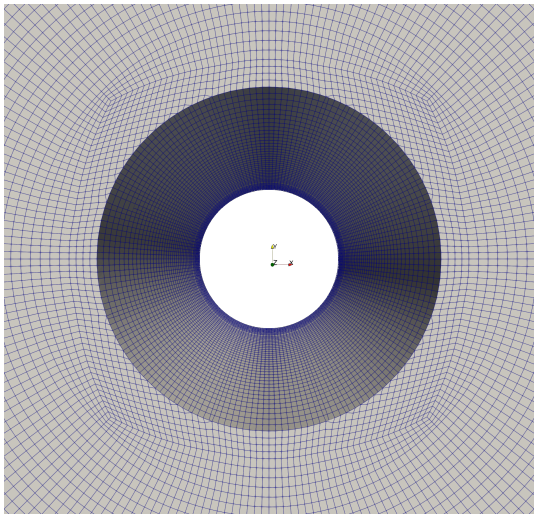

Fig. 5.8 Detail of the o-grid mesh in the transition to the circular mesh zone.

Table 5.4 Level of refinement of mesh for the grid independence.

Refinement	Cell density		Number of cells
	Circumferential cells/round angle	Radial and axial cells/m	
Base	137	305	851264
LVL1	173	384	1669618
LVL2	218	484	3329774
LVL3	274	610	6606008
LVL4	345	769	13273186

LVL2 in Table 5.4. Consequently, the LVL2 refinement mesh is chosen for all the simulations presented in this chapter, as a good compromise between accuracy and computational costs. The only exception is represented by the transient simulations using the GPR viscosity model, which are performed on a coarser mesh. In this case, the mesh employed has a number of cells roughly equal to the half of the base one from Table 5.4. As already mentioned, the reason is the high computational cost of the transient simulations, which require low Courant numbers and therefore significantly increased simulation times.

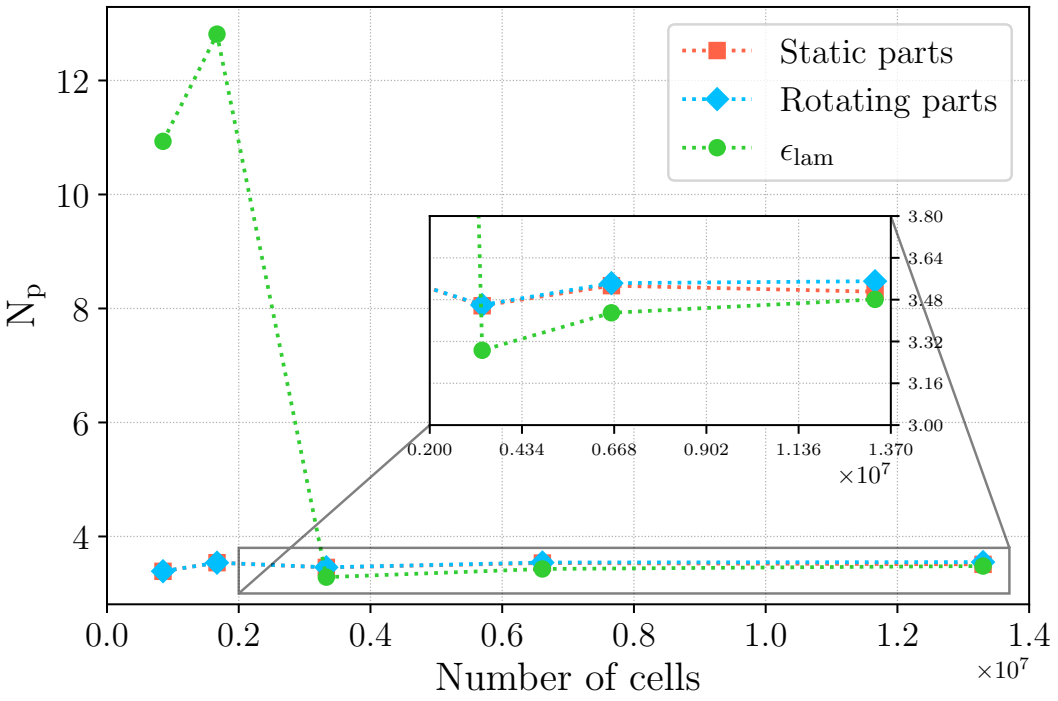

Fig. 5.9 Variation of Power number N_p with the number of cells. Orange squares refers to the Power number calculated using the moments of the forces on the lateral and bottom walls of the vessel. Blue diamonds refer to the Power number calculated using the moments of the forces on the shaft and the impeller. Green circles refers to the Power number calculated using the power as in Equation (5.8).

5.2.2 Numerical details

The software used to conduct the study is OpenFOAM (www.openfoam.org), in its versions 8 and 9. The momentum and continuity equations have been solved and specifications on numerics and schemes used can be found in Appendix F. The system depicted in Figure 5.6 is closed, all the boundary conditions refer to walls elements and are summarised on Table 5.5. A `zeroGradient` condition is imposed to the pressure p for every boundary. The boundary conditions for the velocity are more complex, since the domain is divided in moving and static walls. A `noSlip` velocity condition is imposed on the lateral and bottom walls of the vessel, depicted in light grey in Figure 5.6b. In the experimental setup, the top of the tank is closed with a wall that is not in direct contact with the fluid, leaving a certain headspace. In experiments, the explored operating conditions did not lead to aeration or formation of sizeable vortexes, hence the presence of the headspace is neglected in the computational model. Nonetheless, the fluid in the tank does not experience the presence of a wall

in the top part, and a `slip` velocity condition is imposed here. The Rushton turbine, composed of the disk and the blades, has also a `noSlip` boundary condition applied, since its rotation is taken into account as part of the MRF zone.

A different approach was chosen for the shaft, which has only a small fraction of its length in the MRF zone. In this case, the boundary condition applied is `rotatingWallVelocity`, with a value equal to the impeller speed in rounds per second. At the same time, the shaft is listed among the `nonRotatingPatches` in the MRF, to avoid counting twice its rotation in the zone closer to the impeller.

For the transient simulation using the GPR model, additional boundary conditions are imposed for the scalar field C, which represent the mass concentration of Pluronic L64 in water. A `zeroGradient` condition is applied on all the solid surfaces, and the initial condition is calculated based on the desired concentration of the mixture using `setFields`. This is visible in Figure 5.10, which illustrates the fields of concentration C and kinematic viscosity ν short time after the start of the simulation. In the depicted case the GPR viscosity model was employed with a target composition of 50 % by mass of PL64 in water.

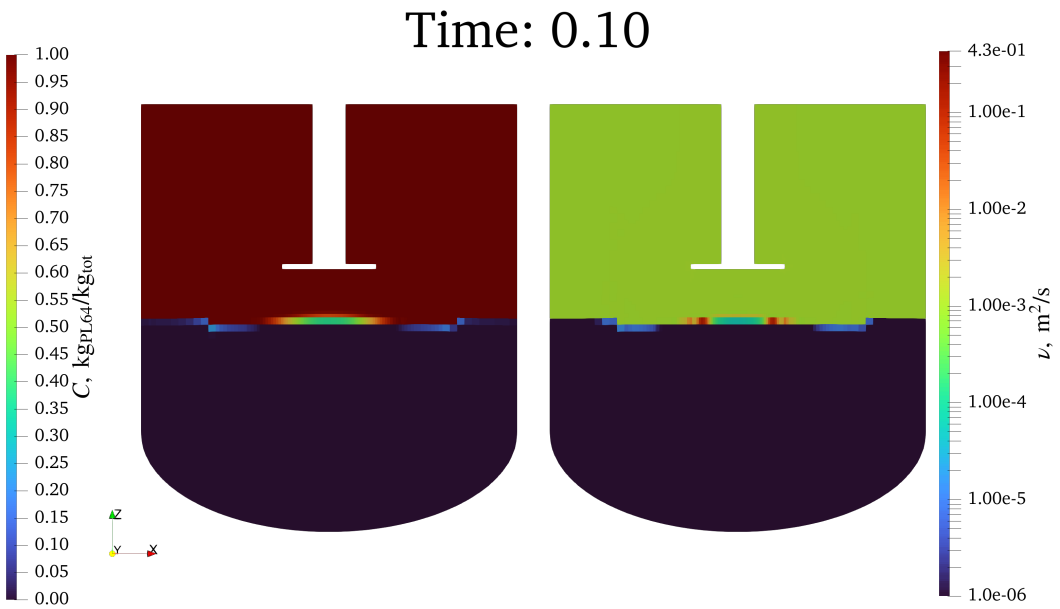

Fig. 5.10 Fields of concentration C (left) and kinematic viscosity ν (right) at $t = 0.1$ s after the start of a transient simulation using the GPR model. The total concentration of PL64 in water is 50 % by mass.

Table 5.5 Boundary conditions and inclusion in the MRF.

Boundary	Pressure	Velocity	MRF applied
Top	Zero gradient	Slip	No
Side wall	Zero gradient	No slip	No
Bottom wall	Zero gradient	No slip	No
Shaft	Zero gradient	Rotating wall	No
Disk	Zero gradient	No slip	Yes
Blades	Zero gradient	No slip	Yes

A list of all the simulations performed is reported in Table 5.6, ordered with increasing Reynolds number. The use of different blends is the key parameter to explore a wide Re interval, as the range of speed for the impeller is limited.

5.2.3 GPR implementation for transient simulations

A slightly different implementation than the one used in Section 3.3 is employed in this chapter. As discussed previously, the GPR model uses rheometry data input as training data, which constitutes a fixed dataset that cannot be expanded while performing simulations. Consequently, no constraint is imposed on the uncertainty associated with the prediction (Figure 5.5) and the flowscheme in Figure 3.4 cannot be implemented. Another difference lies in the implementation of the GPR model within OpenFOAM. The training step is still performed in Python using *scikit-learn* (Pedregosa et al., 2011); however, the hyperparameters are not passed to a C++ to train again the model and predict the viscosity. Instead, the entire model is saved as a *pickle* file, which is a serialised Python object that can contain a binary representation of the GPR trained model. The model is then loaded directly within an OpenFOAM viscosity model, which can execute an internal Python interpreter, as described by Rodriguez and Cardiff (2022). For each computational cell of the domain, the viscosity is evaluated inside OpenFOAM using the strain rate and the polymer concentration as input data. The communication between Python and OpenFOAM is enabled through the *pybind11* library (Cardiff et al., 2018; W. Jakob, J. Rhinelander, D. Moldovan and others, 2017). Compared to the approach presented in Section 3.3, the methodology adopted in this chapter optimises the GPR workflow by performing the training step only once within the Python code. The main advantage of this strategy is the ability to interface arbitrary Python code, exploiting the full range

Table 5.6 CFD simulations performed.

Fluid	RPM	Re
P50H	102	0.76
	203	2.26
	297	4.14
	401	6.67
	494	9.29
P100	149	20.98
	202	28.46
	296	41.93
	350	49.65
	376	53.24
	399	56.55
	426	60.31
	448	63.42
	497	70.38
P50M	349	79.30
	398	90.46
	446	101.26
	502	114.03
P40	252	201.41
	301	240.98
	353	281.84
	403	321.82
	451	360.84
	502	401.19

of features available in modules such as *scikit-learn* and *PyTorch*. This approach eliminates the need for reimplementing kernels and other functionalities in C++.

5.3 Results

The results are divided according to the type of simulation performed. Steady-state MRF simulations are first used to evaluate the power number curve in Section 5.3.1 and the velocity field in Section 5.3.2. These results are compared with experimental measurements to assess the accuracy of the CFD model. Transient simulations are then presented in Section 5.3.3, where the GPR viscosity model is coupled with the CFD solver. This final part is limited to a qualitative analysis, since its purpose is to test whether the model can follow the local changes in concentration, viscosity, and flow during mixing.

5.3.1 Power number curve from steady state simulations

Already in the initial studies on stirred tanks (Rushton et al., 1950) the different dependence of the power number N_p on the Reynolds number Re for unbaffled stirred tanks was observed. For baffled vessels, in laminar conditions the Power number rapidly decreases with increasing Re, while in fully turbulent systems N_p becomes independent from Re. In the latter case, the value of N_p depends only on the geometrical features of the system (Hemrajani & Tatterson, 2003). For this reason, the power number curve for a given impeller is constant above a certain Reynolds number threshold. In unbaffled stirred tanks N_p slightly decreases even in fully turbulent conditions (Scargiali et al., 2017; Scargiali et al., 2013), up to the attainment of supercritical conditions. At that point, the N_p decreases more rapidly with increasing Re as the air entrainment becomes more significant. Correlations are available for asymptotic Re conditions (Scargiali et al., 2017; Scargiali et al., 2013) and identification of the transition point at intermediate Reynolds numbers (Busciglio et al., 2013). At intermediate Reynolds number, the trend is instead less general and more dependent on the specific system.

Figure 5.11 reports the correlation proposed by Scargiali et al. (2013) for low Re together with all the results of CFD simulations performed in this chapter. Numerical data obtained with the highly viscous non-Newtonian P50H show a good agreement

with the correlation, and it is evident the expected change of slope for higher Re. Nonetheless, the data obtained with the other blends do not correspond to a fully turbulent system, hence cannot be compared with high Re correlations. Instead, a

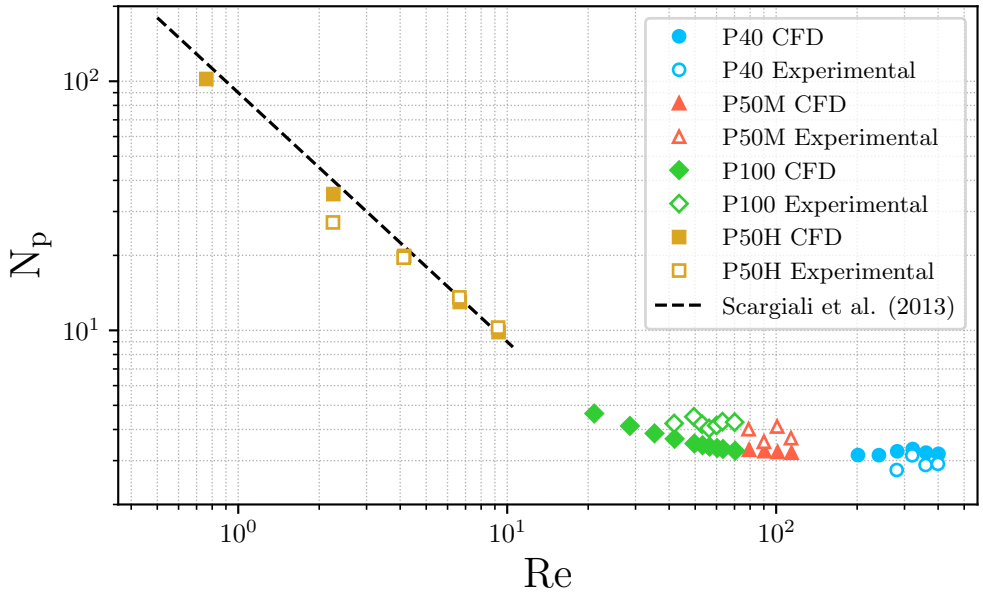

Fig. 5.11 Comparison of numerical and experimental N_p obtained at different Re numbers. Full symbols are used for CFD results and outlined symbols with white filling are used for experimental data. The different colours and symbols refer to the different PL64/water mixtures from Table 5.1. The CFD values reported on the plot are the average of the N_p calculated on the rotating and the static parts starting from M_z. The correlation for low Re from Scargiali et al. (2013) is also reported for comparison.

comparison with experimental data is possible by looking at the difference between filled and hollow symbols in the same figure. The experimental dataset is slightly smaller than the numerical dataset reported in Table 5.6 and its results are in agreement with the CFD. Small discrepancies are visible both at low and intermediate Re, but can be ascribed to different factors. For the P50H blend, it is important to remind that the mixture at this composition is very sensitive to temperature variations. As detailed in Section 5.1.1, the transition from a micellar phase to a hexagonal phase dramatically changes the rheology of the mixture. This means that a shift of a few degrees could require non-negligible adjustments in the parameters of the rheology power-law. These temperature differences can be attributed to changes in the room temperature values during different days of the experimental campaign. The effect of the agitation is considered negligible, as the maximum measured increase of temperature between the start and the end of the tests was 0.1 °C.

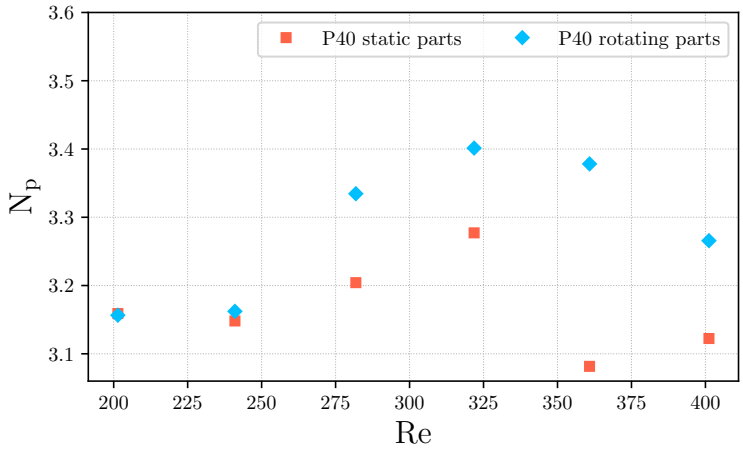

Fig. 5.12 Analysis of the Power number obtained from the CFD simulation of P40 at different Re. Blue diamonds refer to the N_p calculated using the moments acting on the rotating parts, while the orange squares refer to the one calculated using the moments acting on the static parts.

Regarding the N_p values at intermediate Re, the discrepancies can be attributed mostly to the precision of the experimental measurement method. If the relative difference is calculated as

$$\frac{\left|{N_p}^{CFD} - {N_p}^{Exp}\right|}{{N_p}^{Exp}} \cdot 100, \tag{5.9}$$

the maximum discrepancy between the simulation and the experimental results is equal to 30 % for Re = 2.26, while the average difference on the whole dataset is about 15 %.

An additional analysis is necessary for values obtained with the blend P40, which corresponds to the highest tested Reynolds numbers. As already noticeable in Figure 5.11, the blue filled circles are more spread than the values obtained for P50M and P100. Figure 5.12 illustrates more in detail this behaviour, showing also that as Re increases, the Power numbers calculated using moments on static and rotating parts are different. For higher values of Reynolds, the system is no longer in laminar regime, and a different approach is needed to simulate it correctly. Further proof is in Figure 5.13, which reports the evolution of N_p with the simulation step, calculated using Equations (5.3) and (5.6). For lower Re, the values for static and rotating parts converge to a single value, while for higher Re after a pseudo-steady state is reached, the two values start to oscillate independently.

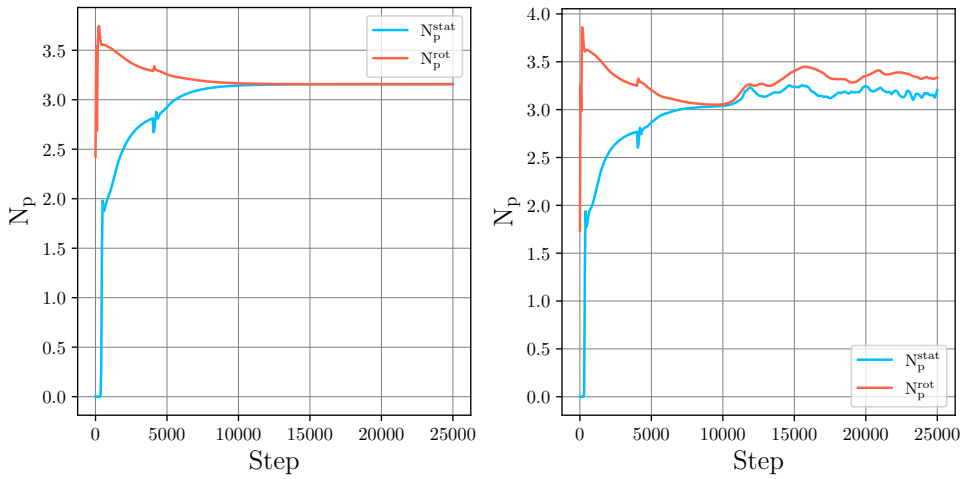

(a) Re = 200. (b) Re = 281.

Fig. 5.13 Analysis of the Power number evolution along the CFD simulation timestep for P40 at different Re. The blue colour refers to the results calculated on the static parts and the orange colour to the one calculated on the rotating parts.

5.3.2 Velocity field at the steady state

In addition to the reproduction of the N_p vs Re curve, the simulations can also be used to study the velocity field inside the stirred tank. In particular, the numerical results are compared with measurements of the velocity obtained through Particle Image Velocimetry (PIV). This comparison is visually presented in two ways: through the velocity profile along a line and through the contour plot on a plane in the domain. The velocity profile is calculated on a line parallel to the axis of the stirred tank, which is also the z axis. This line is positioned at a distance of 0.061 m from it in the radial direction and it is depicted in Figure 5.14. The plane for the contour plot is illustrated in Figure 5.15 and can be identified through the coordinate intervals x = 0.039 - 0.112 m, and z = 0.06 - 0.17 m on the xz plane.

It must be noted that the procedures to compute the velocity profile and field from experimental data and CFD involve two different averaging procedures. Since the PIV data are measured on a plane, the average was computed using the instantaneous value of the velocity components at different times. On the other hand, the CFD simulations are performed at steady state, hence the velocity components are calculated using a spatial average along the circumferential direction. Due to the symmetry of the system, these averaging procedures are comparable and should yield the same results.

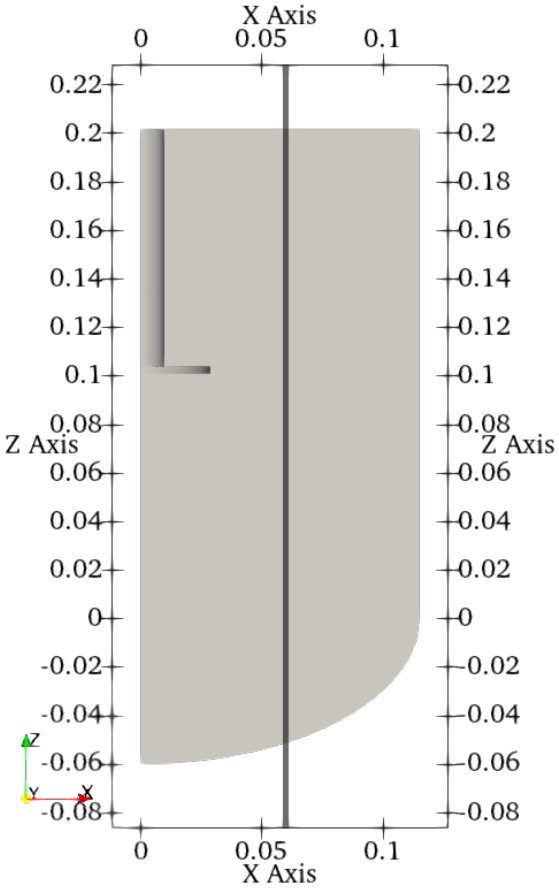

Fig. 5.14 Representation of the line along which the velocity profiles are computed.

A comparison of the velocity field obtained from the CFD simulations and the one obtained through PIV was performed for two different Reynolds numbers. In one case the system studied is the P50M at Re = 79.30, while the P40 is investigated at Re = 281.84. In this second case the system is most probably approaching the transitional regime. Consequently, a worse agreement between computational and experimental data is expected. In this section, the symbols v_x will be used for the radial component of the velocity field and the symbol v_y will be used for the tangential one. While this is not true in the whole domain, all the results presented here refer to averages along the circumferential direction. These will be illustrated on the xz plane, where the x and the z directions correspond to the radial and axial directions, respectively, as shown in Figures 5.14 and 5.15.

Fig. 5.15 Plane used to compare the velocity fields through contour plots after averaging.

For the P50M, a comparison of the three velocity components is presented in Figure 5.16, showing a general good agreement between CFD and PIV data. The tangential component, which corresponds to v_y in the contour plots, has the highest values and it is the one driving the flow. As expected, the value v_y rapidly decreases moving away from the impeller zone, where its maximum is found. In Figure 5.16b, CFD model was not able to reproduce a peculiar structure, visible in the PIV contour plot, which is attributed to the impeller's blade movement. Nonetheless, the magnitude of the tangential component obtained from the simulation shows only moderate deviation from the experimental one.

A good agreement is found also regarding the secondary flow, which is the velocity vector given by the radial and axial contribution, respectively v_x and v_z in Figure 5.16. The secondary flow is the main driver of distributive mixing mechanism (Stobiac et al., 2014) and is expected to have relatively higher values at low Re. The shape of the radial and axial velocity fields are reproduced correctly by the CFD model, with small differences in local values. In particular, in Figure 5.16c, is visible the axial recirculation flow, which is typically more pronounced for low Re

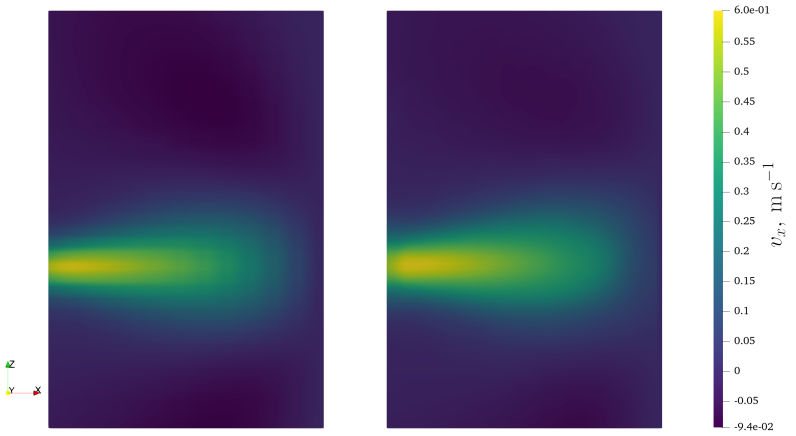

(a) Radial velocity component obtained from CFD (left) and experiments (right).

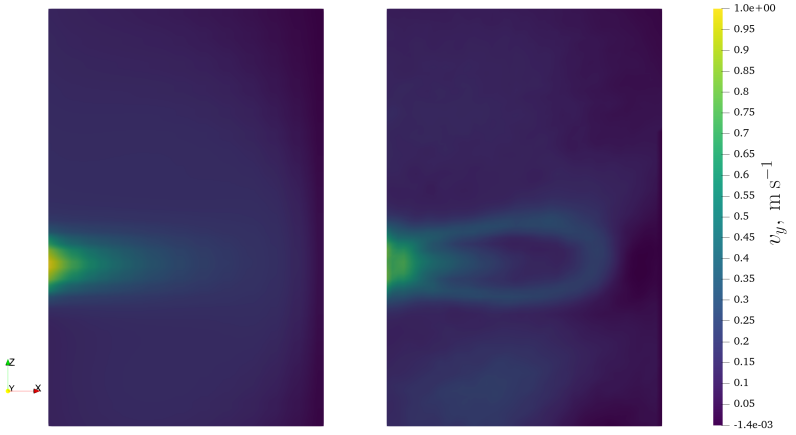

(b) Tangential velocity component obtained from CFD (left) and experiments (right).

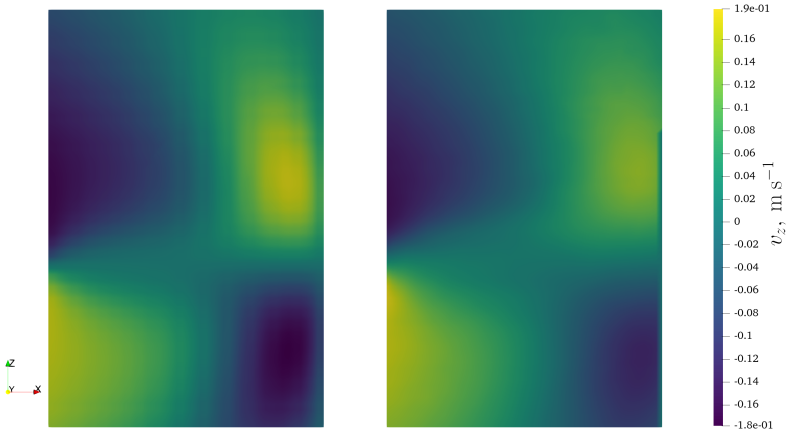

(c) Axial velocity component obtained from CFD (left) and experiments (right).

Fig. 5.16 Comparison of the velocity components obtained from simulations and experiments for the P50M blend at Re = 79.30.

systems. A quantitative evaluation of the error between PIV and CFD is illustrated in Figure 5.17, where the velocity values are compared and normalised by the tip velocity, according to the following equation:

$$\Delta v_i^{\text{rel}} = \frac{\left| v_i^{\text{CFD}} - v_i^{\text{PIV}} \right|}{v_{\text{tip}}}, \tag{5.10}$$

where i is the velocity component index and $v_{\text{tip}} = 1.40\,\text{m}\,\text{s}^{-1}$ for this simulation. The normalisation using v_{tip} highlights the areas where the error is relevant with respect to a characteristic velocity of the system. In this way, it is also possible to compare the error between the different velocity components, which is not practical with the absolute error. Moreover, the tip velocity takes into account the potential inaccuracies of the PIV measurements, which are less precise in low-velocity zones. In this context, the use of the classic relative error would instead emphasise the error in the low-velocity zones, overrating their importance.

The contour plots in Figure 5.17 show a limited error, which is below 10 % of the tip velocity for the radial and axial components. The tangential component shows the peak error in a small region closer to the impeller, with a value that reaches 18 % of v_{tip}. Velocity profiles are also compared along the line in Figure 5.14. The radial distance from the axis of the stirred tank is chose to from the impeller, to avoid interference of the blades during the measurement procedure. The results in Figure 5.18 show a remarkably good agreement, especially for the radial component, v_x. The errors on the axial components are more pronounced, with CFD slightly overpredicting the absolute values, but are still acceptable. The maximum velocity and the inversion of the sign are indeed at the same axial coordinate for the two profiles in Figure 5.18b. Furthermore, as already said, the PIV is more accurate where the velocity is higher, hence a higher discrepancy is expected for the v_z profile. This is also noticeable for the radial velocity in Figure 5.18a away from the impeller zone, where the fluid is moving slower.

For the analysis of the P40 system, only contours of the normalised error are showed in this section. The contour plots for the three velocity components obtained via simulations and experiments will not be described in detail here, and can be found in Appendix C. The general shape of the velocity field described for Re = 79.30 is still clearly visible, with increased velocity values for all the components. The

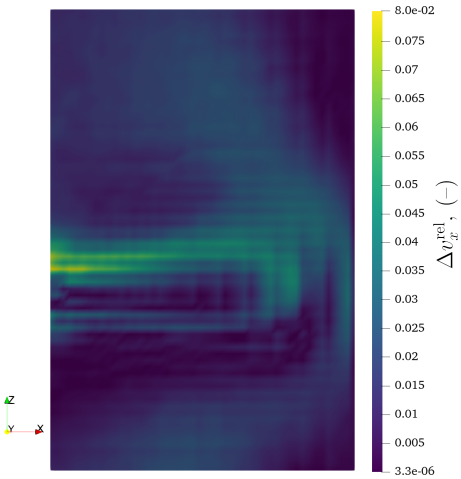

(a) Radial velocity component.

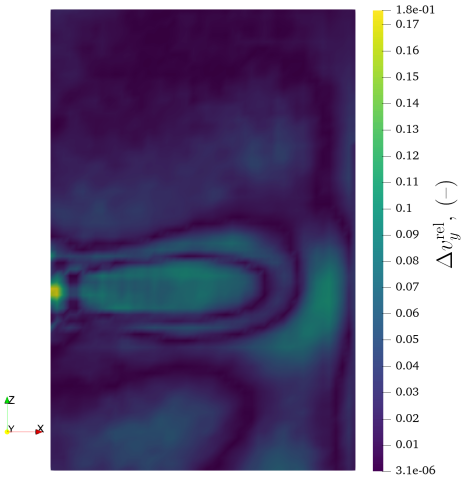

(b) Tangential velocity component.

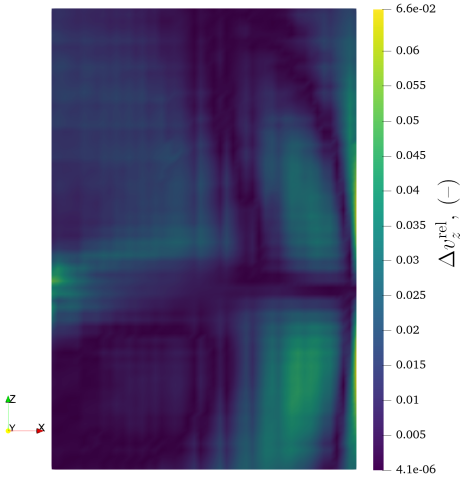

(c) Axial velocity component.

Fig. 5.17 Error between CFD and PIV velocity field normalised by $v_{\mathrm{tip}} = 1.40$ m/s. P50M blend at Re = 79.30.

only exception concerns the tangential component, whose PIV contour plot does not exhibit any structure related to the impeller blades.

Figure 5.19 reports the error between CFD and PIV calculated according to Equation (5.10) for the P40 mixture. In this case, the system is at Re = 281.84, with a tip velocity of $v_{\mathrm{tip}} = 1.42\,\mathrm{m\,s^{-1}}$. The errors are generally higher than the ones calculated for the lower Re case, with values below 19 % of the tip velocity for the radial component and below 16 % for the axial one. The peak error is found again

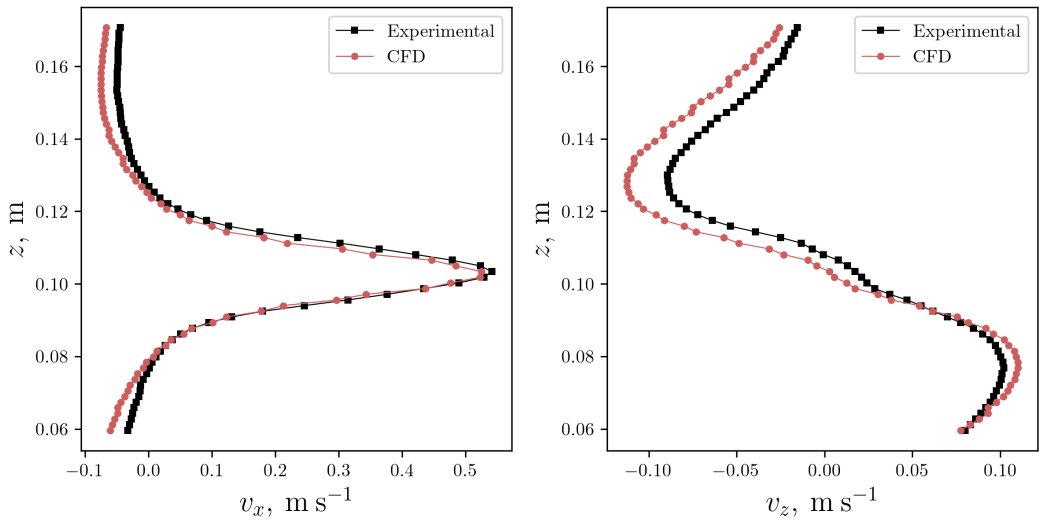

(a) Radial velocity profile.

(b) Axial velocity profile.

Fig. 5.18 Numerical and experimental velocity profiles for the P50M system with Re = 79.30 at radial coordinate of 0.061 m. Black squares are used for experimental values and red circles for numerical values.

for the tangential component close to the impeller, with a value that reaches 35 % of v_{tip}. The higher discrepancies are confirmed by the velocity profiles reported in Figure 5.20. For this system, the differences between the velocity values at different z coordinates are visibly more important. Moreover, the CFD profile seems slightly shifted in the axial direction by less than 0.02 m. As already discussed, a steady state simulation with a laminar model is not the most suited approach for such a Reynolds number. Hence, higher discrepancies between numerical and experimental data are expected in this case. Nonetheless, it must be noted that the general trend of the velocity profile is still captured with moderate errors.

5.3.3 CFD – GPR coupling for transient simulations

The assessment of the GPR viscosity model coupled with CFD is performed using a transient simulation of a system with a PL64 concentration of 50 % by mass in water. The impeller speed is set to 247 RPM, and the maximum Courant number in the domain is limited to one to ensure numerical stability. As discussed in the previous sections, the use of the MRF approach in combination with a coarse mesh was required by the high computational cost of transient simulations with the GPR

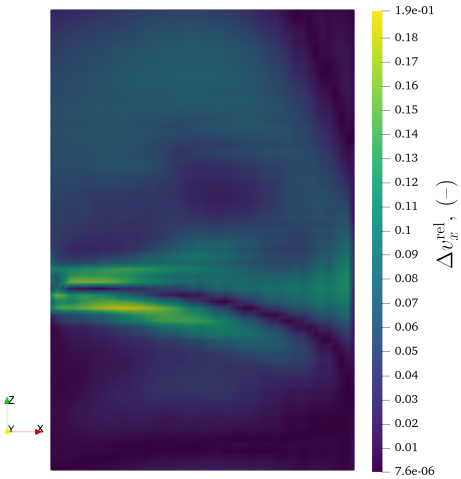

(a) Radial velocity component.

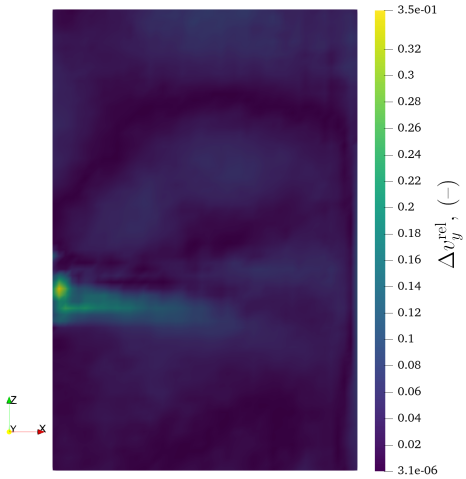

(b) Tangential velocity component.

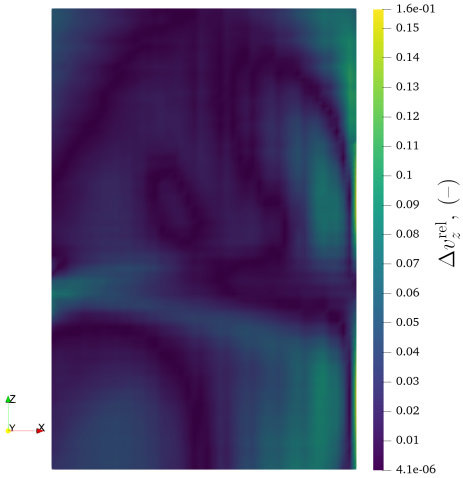

(c) Axial velocity component.

Fig. 5.19 Error between CFD and PIV velocity field normalised by $v_{\mathrm{tip}} = 1.42\,\mathrm{m\,s^{-1}}$. P40 blend at Re = 281.84.

viscosity model. For this reason, the present analysis is limited to a qualitative assessment of the results.

The effects of local composition and shear rate on mixture viscosity are presented in Figure 5.21 and Figure 5.22, respectively. Focusing on Figure 5.21, the effect of PL64 concentration is visible and consistent with the trends reported in Figure 5.4. The lowest viscosity values correspond to pure water, as observed near the bottom of the tank, while pure polymer exhibits an intermediate viscosity. The maximum

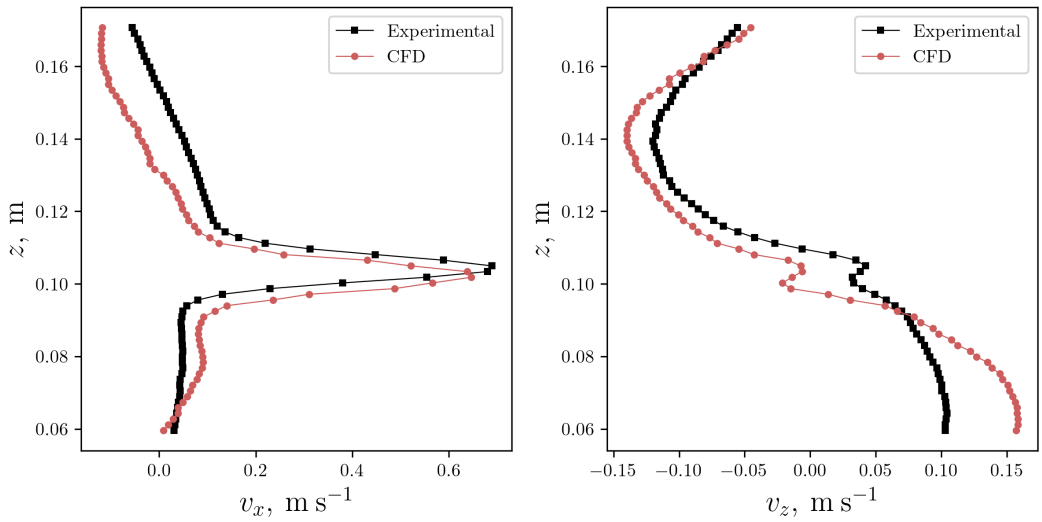

(a) Radial velocity profile.

(b) Axial velocity profile.

Fig. 5.20 Numerical and experimental velocity profiles for the P40 system with Re = 281.84 at radial coordinate of 0.061 m. Black squares are used for experimental values and red circles for numerical values.

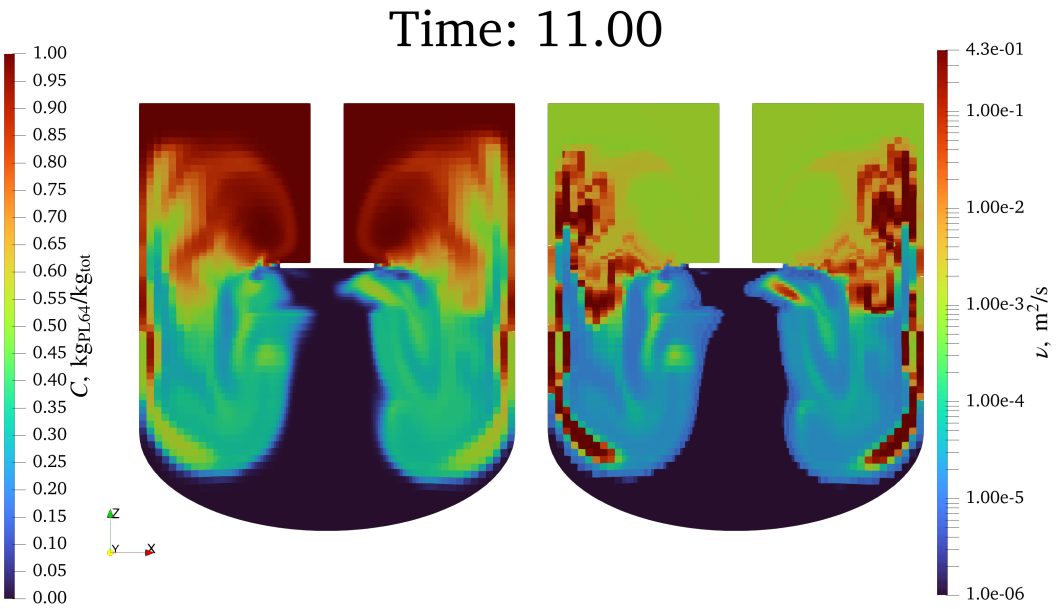

Fig. 5.21 Fields of concentration C (left) and kinematic viscosity ν (right) at $t = 11$ s after the start of a transient simulation using the GPR model. The total concentration of PL64 in water is 50 % by mass.

viscosity is reached for local concentration C between 0.45 and 0.6 $\mathrm{kg_{PL64}/kg_{tot}}$, where comparison with the rheometry and the phase diagram suggest a transition to

the hexagonal phase. The dependence of viscosity on shear rate in Figure 5.22 is less pronounced, as variations in $\dot{\gamma}$ induce more limited changes in the viscosity when compared to concentration. Nevertheless, the shear-rate dependence of viscosity becomes appreciable only in regions near the impeller where the strain rate varies greatly together with intermediate polymer concentrations, which correspond to higher viscosity and stronger non-Newtonian behaviour. From both contour plots,

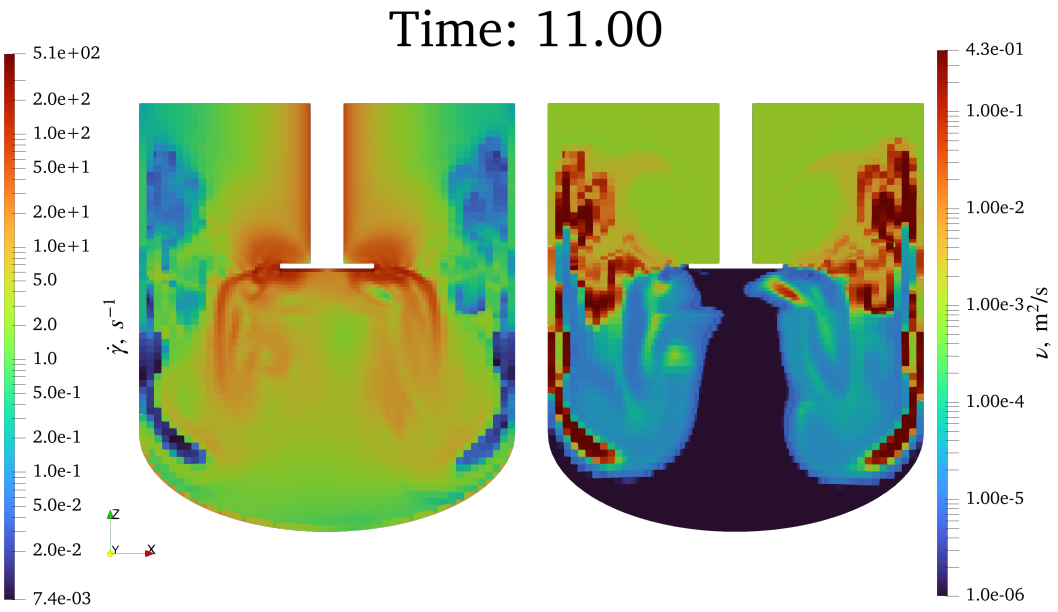

Fig. 5.22 Fields of shear rate $\dot{\gamma}$ (left) and viscosity ν (right) at $t = 11$ s after the start of a transient simulation using the GPR model. The total concentration of PL64 in water is 50 % by mass.

the low resolution of the mesh is evident. This choice was necessary to simulate a sufficiently long time interval to achieve appreciable mixing between the two fluids.

Finally, a comparison between the concentration scalar field in Figure 5.21 and that in Figure 5.10 highlights an additional modelling challenge associated with transient mixing. During the initial time steps, the impeller is surrounded by pure PL64, which is viscous enough to maintain the Re number low in every part of this region. As the simulation progresses, the impeller rotation generates an axial flow that entrains the two fluids, bringing pure water into this high-velocity region. As a result, the Reynolds number locally increases and the flow can no longer be considered fully laminar throughout the entire domain.

5.4 Conclusion

In this chapter, a Computational Fluid Dynamics model was developed and assessed for the modelling of unbaffled stirred tanks operating with viscous Newtonian and non-Newtonian Pluronic L64/water mixtures. The study combined different viscosity modelling techniques, and CFD simulations tailored to laminar flow regimes, with systematic comparison against experimental measurements.

The rheological behaviour of PL64 mixtures is strongly dependent on both concentration and temperature, with distinct phases leading to markedly different viscosity values and shear rate dependencies. Classical constitutive models, namely power-law and Bird–Carreau, were successfully employed to describe selected non-Newtonian blends, while Newtonian behaviour was confirmed for micellar phase mixtures at lower concentrations. In parallel, a Gaussian Process Regression model was developed to provide a continuous, data-driven description of viscosity as a function of both shear rate and polymer concentration. Although limited by the availability and distribution of rheometry data, this model showed potential in capturing phase transition driven trends and marking a flexible alternative to analytical constitutive laws.

The CFD model of the stirred tank, based on a Multiple Reference Frame approach and laminar flow assumptions, was carefully validated through a grid dependency study and applied over a wide range of Reynolds numbers by varying both impeller speed and fluid properties. Numerical predictions of the power number showed good agreement with experimental measurements for low and intermediate Reynolds numbers, with an average discrepancy of approximately 15 %. Deviations observed at higher Reynolds numbers, particularly for the least viscous mixture, highlighted the limitations of steady-state laminar modelling as the flow approaches the transitional regime.

Beyond integral quantities, the CFD simulations were able to reproduce the main features of the internal flow field. Comparisons with Particle Image Velocimetry data demonstrated a good agreement for velocity magnitudes, profiles, and recirculation patterns at low Reynolds numbers, with errors generally below 10 – 20 % of the impeller tip velocity. As expected, discrepancies increased for higher Reynolds numbers, especially for the tangential velocity component near the impeller, reflecting both the inadequacy of laminar assumptions under these conditions.

Finally, the coupling between CFD and the GPR based viscosity model was demonstrated through transient simulations of mixing between fluids of different composition. Although constrained by computational cost and coarse spatial resolution, these simulations qualitatively confirmed the ability of the proposed approach to account for local variations in viscosity driven by both composition and shear rate. The results also revealed the emergence of locally elevated Reynolds numbers during mixing, underscoring the additional modelling challenges associated with transient, composition dependent flows.

Overall, this chapter establishes a validated CFD framework for unbaffled stirred tanks operating with complex fluids and demonstrates the feasibility of integrating data-driven rheological models into CFD solvers. The insights gained here provide an initial basis for extending the methodology toward transient simulations and more comprehensive experimental datasets to further strengthen its predictive capability.

Chapter 6

Final conclusions and open questions

This thesis assessed a multiscale modelling strategy to predict the flow of complex fluids in mixing equipment, with the core objective of linking microstructure-driven rheology to macroscopic performance metrics. The work combined Dissipative Particle Dynamics (DPD) as a computational rheometer, Computational Fluid Dynamics (CFD) as the process-scale solver, and Gaussian Process Regression (GPR) as a surrogate layer to bridge scales. Across the case studies, the thesis addressed a central challenge in complex-fluid processing: mixing devices expose materials to broad, heterogeneous strain rate and composition fields, so constitutive models must be reliable over operating windows that are difficult to probe experimentally and computationally.

A first contribution is an automated coupling framework where the surrogate model's uncertainty actively guides which microscale simulations are needed. In the proposed loop, an initial CFD simulation provides the strain rate interval actually explored in the equipment. DPD simulations produce viscosity estimates at selected shear rates, which become training data for a GPR viscosity model. The GPR is then queried over the CFD strain rate interval, and new DPD runs are launched only where predictive uncertainty is highest, until a prescribed uncertainty threshold is reached. This strategy reduces the number of DPD simulations required to build a constitutive description in the relevant regime, addressing the dominant cost of multiscale workflows.

The multiscale approach was demonstrated on an industrial surfactant blend (Miraspec UB75) flowing through a Sulzer SMX static mixer. On the microscale side,

a DPD model for SLES/water was adopted from literature and extended to include CMEA using a parameterisation based on water/octanol partition coefficients. The model was qualitatively validated by reproducing microstructures consistent with the reported phase behaviour for water/SLES mixtures (micellar, hexagonal and lamellar regions) and by obtaining a lamellar structure for the UB75 formulation. Non-equilibrium DPD simulations were then used to build a shear-dependent viscosity curve, which was used to train the GPR model embedded in OpenFOAM. The resulting constitutive response was that of a shear thinning fluids and agreed well with available viscosity measurements. At the process scale, the model obtained realistic pressure drops when compared to the behaviour of similar blends in the same type of mixing device.

At the same time, the UB75 study highlighted a limitation of standard non-equilibrium DPD rheometry, which is the need for relatively high imposed shear rates to overcome thermal noise and obtain stable velocity profiles. This usually leads to shear rates that are not representative in physical units when using equilibrium-derived conversion factors. In practice, conversion factors were tuned to match the experimental viscosity obtained at a reference condition. While effective for engineering-level coupling, the approach motivates a more principled route to low shear rheology in DPD.

The second major contribution directly addresses this issue by adapting the Transient Time Correlation Function (TTCF) formalism to DPD. The thesis shows that TTCF enables viscosity estimation at arbitrarily low shear rates for a simple DPD fluid, with a precision that does not degrade as shear decreases. This contrast to what happen with direct averaging (DAV), whose uncertainty rapidly becomes prohibitive at low shear. A key methodological result is that standard TTCF mappings, commonly used to enforce zero initial dissipation, are not compatible with DPD because dissipative and random forces break the symmetry required for cancellation. The work adopts a covariance-based correction to the TTCF expression and uses bootstrapping to estimate uncertainty, yielding a practical TTCF workflow for DPD without mappings. Computationally, the approach remains embarrassingly parallel: many short non-equilibrium trajectories are simulated and post-processed, and bootstrapping adds negligible overhead relative to simulation time. This development opens the possibility of performing DPD rheology under experimentally relevant shear rates, thereby improving the consistency of the conversion to physical units.

The thesis also developed CFD models for unbaffled stirred tanks operating with viscous Newtonian and non-Newtonian Pluronic L64/water mixtures, linking macroscopic predictions to experimental measurements of power consumption and velocity fields. The work established a robust computational workflow in OpenFOAM using a Multiple Reference Frame (MRF) approach. Across a Reynolds number interval from 0.76 to 400, the laminar steady-state CFD model reproduced the measured power number trend well at low and intermediate Reynolds numbers, with an average discrepancy of about 15 % and a maximum around 30 % at low Re. Deviations at the highest Reynolds numbers for the least viscous mixture revealed the expected limits of a laminar model as the flow approaches transitional behaviour. Beyond integral performance, comparisons with PIV measurements showed that the CFD model captured the main flow structures and velocity magnitudes in the unbaffled vessel at low Reynolds numbers. For the P50M case (Re $\approx$ 80), errors in the velocity components were generally below 20 % of the impeller tip velocity, with the largest discrepancy in the tangential component near the impeller. At a higher Reynolds number (P40 at Re $\approx$ 282), errors increased, including profile shifts and larger tangential-component deviations, consistent with the growing inadequacy of the laminar assumption and the sensitivity of near-impeller flow to unsteady blade-induced structures.

Finally, the GPR rheology was extended to a two-variable model $\mu(\dot{\gamma}, C)$ for Pluronic L64, enabling composition-dependent viscosity in CFD simulations. Transient mixing simulations required a coarse mesh and qualitatively demonstrated the coupling's ability to produce spatially varying viscosity fields driven by both concentration and shear. Nonetheless, two critical modelling challenges emerged in the case of transient mixing in stirred tanks. The first is related to the computational time, due to restrictions on the Courant number. The second is related to variations in the local flow regime in the impeller region depending on the composition, meaning that a laminar modelling choice may become inconsistent during the evolution.

Several open questions follow naturally. The first one is the development of transferable DPD models that can be systematically validated and used for a variety of complex fluids. The second is the extension of the TTCF formalism to non-Newtonian DPD fluids, to enable low-shear rheology for structured systems. In this context, the long stress-relaxation times are the challenge to address, since decorrelation behaviour and sampling requirements may become severe for strongly structured systems. Lastly, transient mixing systems must be simulated with models that offer

reliable predictions in laminar, transitional, and turbulent regimes. While LES-based approaches could be considered for transitional and turbulent regimes, the time step requirements and the computational load could make this solution impractical for engineering applications. From this perspective, the development of surrogate models to accelerate flow field prediction could instead be a promising research direction.

References

Alcamo, R., Micale, G., Grisafi, F., Brucato, A., & Ciofalo, M. (2005). Large-eddy simulation of turbulent flow in an unbaffled stirred tank driven by a Rushton turbine. *Chemical Engineering Science*, *60*(8), 2303–2316. https://doi.org/10.1016/j.ces.2004.11.017

Alexandridis, P., & Alan Hatton, T. (1995). Poly(ethylene oxide)–poly(propylene oxide)–poly(ethylene oxide) block copolymer surfactants in aqueous solutions and at interfaces: Thermodynamics, structure, dynamics, and modeling. *Colloids and Surfaces A: Physicochemical and Engineering Aspects*, *96*(1), 1–46. https://doi.org/10.1016/0927-7757(94)03028-X

Alexandridis, P., Zhou, D., & Khan, A. (1996). Lyotropic Liquid Crystallinity in Amphiphilic Block Copolymers: Temperature Effects on Phase Behavior and Structure for Poly(ethylene oxide)-b-poly(propylene oxide)-b-poly(ethylene oxide) Copolymers of Different Composition. *Langmuir*, *12*(11), 2690–2700. https://doi.org/10.1021/la951025s

Allen, M. P., & Tildesley, D. J. (2017, August). *Computer Simulation of Liquids*. Oxford University Press.

Anderson, R. L., Bray, D. J., Del Regno, A., Seaton, M. A., Ferrante, A. S., & Warren, P. B. (2018). Micelle Formation in Alkyl Sulfate Surfactants Using Dissipative Particle Dynamics. *Journal of Chemical Theory and Computation*, *14*(5), 2633–2643. https://doi.org/10.1021/acs.jctc.8b00075

Anderson, R. L., Bray, D. J., Ferrante, A. S., Noro, M. G., Stott, I. P., & Warren, P. B. (2017). Dissipative particle dynamics: Systematic parametrization using water-octanol partition coefficients. *The Journal of Chemical Physics*, *147*(9), 094503. https://doi.org/10.1063/1.4992111

Assirelli, M., Bujalski, W., Eaglesham, A., & Nienow, A. W. (2008). Macro- and micromixing studies in an unbaffled vessel agitated by a Rushton turbine. *Chemical Engineering Science*, *63*(1), 35–46. https://doi.org/10.1016/j.ces.2007.07.074

Aubin, J., Fletcher, D. F., & Xuereb, C. (2004). Modeling turbulent flow in stirred tanks with CFD: The influence of the modeling approach, turbulence model and numerical scheme. *Experimental Thermal and Fluid Science*, *28*(5), 431–445. https://doi.org/10.1016/j.expthermflusci.2003.04.001

Bakker, A., Laroche, R. D., Wang, M. H., & Calabrese, R. V. (1997). Sliding Mesh Simulation of Laminar Flow in Stirred Reactors. *Chemical Engineering Research and Design*, *75*(1), 42–44. https://doi.org/10.1205/026387697523372

Boek, E. S., Coveney, P. V., & Lekkerkerker, H. N. W. (1996). Computer simulation of rheological phenomena in dense colloidal suspensions with dissipative particle dynamics. *Journal of Physics: Condensed Matter*, *8*(47), 9509. https://doi.org/10.1088/0953-8984/8/47/053

Boek, E. S., Coveney, P. V., Lekkerkerker, H. N. W., & van der Schoot, P. (1997). Simulating the rheology of dense colloidal suspensions using dissipative particle dynamics. *Physical Review E*, *55*(3), 3124–3133. https://doi.org/10.1103/PhysRevE.55.3124

Boromand, A., Jamali, S., & Maia, J. M. (2015). Viscosity measurement techniques in Dissipative Particle Dynamics. *Computer Physics Communications*, *196*, 149–160. https://doi.org/10.1016/j.cpc.2015.05.027

Borzsák, I., Cummings, P. T., & Evans, D. J. (2002). Shear viscosity of a simple fluid over a wide range of strain rates. *Molecular Physics*, *100*(16), 2735–2738. https://doi.org/10.1080/00268970210137275

Brucato, A., Ciofalo, M., Grisafi, F., & Micale, G. (1998). Numerical prediction of flow fields in baffled stirred vessels: A comparison of alternative modelling approaches. *Chemical Engineering Science*, *53*(21), 3653–3684. https://doi.org/10.1016/S0009-2509(98)00149-3

Busciglio, A., Caputo, G., & Scargiali, F. (2013). Free-surface shape in unbaffled stirred vessels: Experimental study via digital image analysis. *Chemical Engineering Science*, *104*, 868–880. https://doi.org/10.1016/j.ces.2013.10.019

Busciglio, A., Grisafi, F., Scargiali, F., & Brucato, A. (2014). Mixing dynamics in uncovered unbaffled stirred tanks. *Chemical Engineering Journal*, *254*, 210–219. https://doi.org/10.1016/j.cej.2014.05.084

Capaccio, A., Caserta, S., Guido, S., Rusciano, G., & Sasso, A. (2020). Dissolution of a surfactant-water lamellar phase investigated by combining time-lapse polarized light microscopy and confocal Raman spectroscopy. *Journal of Colloid and Interface Science*, *561*, 136–146. https://doi.org/10.1016/j.jcis.2019.11.092

Cardiff, P., Karač, A., Jaeger, P. D., Jasak, H., Nagy, J., Ivanković, A., & Tuković, Ž. (2018). An open-source finite volume toolbox for solid mechanics and fluid-solid interaction simulations. (arXiv:1808.10736). https://doi.org/10.48550/arXiv.1808.10736

Castaldo, R. I., Pasquino, R., Villone, M. M., Caserta, S., Gu, C., Grizzuti, N., Guido, S., Maffettone, P. L., & Guida, V. (2019). Dissolution of concentrated surfactant solutions: From microscopy imaging to rheological measurements through numerical simulations. *Soft Matter*, *15*(41), 8352–8360. https://doi.org/10.1039/C9SM01481K

Ciofalo, M., Brucato, A., Grisafi, F., & Torraca, N. (1996). Turbulent flow in closed and free-surface unbaffled tanks stirred by radial impellers. *Chemical Engineering Science*, *51*(14), 3557–3573. https://doi.org/10.1016/0009-2509(96)00004-8

Cohu, O., & Magnin, A. (1995). Rheometry of paints with regard to roll coating process. *Journal of Rheology*, *39*(4), 767–785. https://doi.org/10.1122/1.550656

De Roma, F., Marchisio, D., Boccardo, G., Bouaifi, M., & Buffo, A. (2024). Application of a multiscale approach for modeling the rheology of complex fluids in industrial mixing equipment. *Physics of Fluids*, *36*(2), 023119. https://doi.org/10.1063/5.0185471

De Roma, F., Maffioli, L., Smith, E. R., & Buffo, A. (2026). Study of Arbitrarily Low Shear Rate Rheology Using Dissipative Particle Dynamics. *Journal of Chemical Theory and Computation*, *22*(8), 3779–3795. https://doi.org/10.1021/acs.jctc.5c01825

Del Regno, A., Warren, P. B., Bray, D. J., & Anderson, R. L. (2021). Critical Micelle Concentrations in Surfactant Mixtures and Blends by Simulation. *The Journal of Physical Chemistry B*, *125*(22), 5983–5990. https://doi.org/10.1021/acs.jpcb.1c00893

Di Spirito, N. A., Grizzuti, N., & Pasquino, R. (2024). Self-assembly of Pluronics: A critical review and relevant applications. *Physics of Fluids*, *36*(11), 111302. https://doi.org/10.1063/5.0238690

Doi, M., & Edwards, S. F. (1988, November). *The Theory of Polymer Dynamics*. Oxford University Press.

Droghetti, H., Pagonabarraga, I., Carbone, P., Asinari, P., & Marchisio, D. (2018). Dissipative particle dynamics simulations of tri-block co-polymer and water: Phase diagram validation and microstructure identification. *The Journal of Chemical Physics*, *149*(18), 184903. https://doi.org/10.1063/1.5049641

Efron, B. (1979). Bootstrap Methods: Another Look at the Jackknife. *The Annals of Statistics*, *7*(1), 1–26. https://doi.org/10.1214/aos/1176344552

Ernst, M. H., & Brito, R. (2005). Generalized Green-Kubo formulas for fluids with impulsive, dissipative, stochastic, and conservative interactions. *Physical Review E*, *72*(6), 061102. https://doi.org/10.1103/PhysRevE.72.061102

Español, P., & Warren, P. (1995). Statistical mechanics of dissipative particle dynamics. *Europhysics Letters (EPL)*, *30*(4), 191–196. https://doi.org/10.1209/0295-5075/30/4/001

Español, P., & Warren, P. B. (2017). Perspective: Dissipative particle dynamics. *The Journal of Chemical Physics*, *146*(15), 150901. https://doi.org/10.1063/1.4979514

Etchells, A. W., & Hesketh, R. P. (2023). Blending in unbaffled and baffled mechanically agitated vessels – Effect of Reynolds number and liquid height. *Chemical Engineering Research and Design*, *196*, 599–605. https://doi.org/10.1016/j.cherd.2023.06.025

Etchells III, A. W., & Meyer, C. F. (2003). Mixing in Pipelines. In *Handbook of Industrial Mixing* (pp. 391–477). John Wiley & Sons, Ltd. https://doi.org/10.1002/0471451452.ch7

Evans, D. J., & Morriss, G. P. (1988). Transient-time-correlation functions and the rheology of fluids. *Physical Review A*, *38*(8), 4142–4148. https://doi.org/10.1103/PhysRevA.38.4142

Evans, D. J., Searles, D. J., & Williams, S. R. (2016, July). *Fundamentals of Classical Statistical Thermodynamics: Dissipation, Relaxation, and Fluctuation Theorems*. John Wiley & Sons.

Evans, D., & Morriss, G. (1990). *Statistical mechanics of nonequilibrium liquids*. Academic Press.

Ferrari, M., Boccardo, G., Buffo, A., Vanni, M., & Marchisio, D. L. (2023a). CFD simulation of a high-shear mixer for food emulsion production. *Journal of Food Engineering*, *358*, 111655. https://doi.org/10.1016/j.jfoodeng.2023.111655

Ferrari, M., Boccardo, G., Marchisio, D. L., & Buffo, A. (2023b). Application of dissipative particle dynamics to interfacial systems: Parameterization and scaling. *AIP Advances*, *13*(3), 035324. https://doi.org/10.1063/5.0139275

Ferrari, M., Handgraaf, J.-W., Boccardo, G., Buffo, A., Vanni, M., & Marchisio, D. L. (2022). Molecular modeling of the interface of an egg yolk protein-based

emulsion. *Physics of Fluids*, *34*(2), 021903. https://doi.org/10.1063/5.0079883

Fraaije, J. G. E. M., van Male, J., Becherer, P., & Serral Gracià, R. (2016). Coarse-Grained Models for Automated Fragmentation and Parametrization of Molecular Databases. *Journal of Chemical Information and Modeling*, *56*(12), 2361–2377. https://doi.org/10.1021/acs.jcim.6b00003

Frenkel, D., & Smit, B. (2023, July). *Understanding Molecular Simulation*.

González-Melchor, M., Mayoral, E., Velázquez, M. E., & Alejandre, J. (2006). Electrostatic interactions in dissipative particle dynamics using the Ewald sums. *The Journal of Chemical Physics*, *125*(22), 224107. https://doi.org/10.1063/1.2400223

Good, P. I. (1999). *Resampling Methods: A Practical Guide to Data Analysis*. Birkhäuser.

Green, M. S. (1954). Markoff Random Processes and the Statistical Mechanics of Time-Dependent Phenomena. II. Irreversible Processes in Fluids. *The Journal of Chemical Physics*, *22*(3), 398–413. https://doi.org/10.1063/1.1740082

Groot, R. D. (2003). Electrostatic interactions in dissipative particle dynamics—simulation of polyelectrolytes and anionic surfactants. *The Journal of Chemical Physics*, *118*(24), 11265–11277. https://doi.org/10.1063/1.1574800

Groot, R. D., & Rabone, K. L. (2001). Mesoscopic Simulation of Cell Membrane Damage, Morphology Change and Rupture by Nonionic Surfactants. *Biophysical Journal*, *81*(2), 725–736. https://doi.org/10.1016/S0006-3495(01)75737-2

Groot, R. D. (2000). Mesoscopic Simulation of Polymer-Surfactant Aggregation. *Langmuir*, *16*(19), 7493–7502. https://doi.org/10.1021/la000010d

Groot, R. D., & Warren, P. B. (1997). Dissipative particle dynamics: Bridging the gap between atomistic and mesoscopic simulation. *The Journal of Chemical Physics*, *107*(11), 4423–4435. https://doi.org/10.1063/1.474784

Hartkamp, R., Bernardi, S., & Todd, B. D. (2012). Transient-time correlation function applied to mixed shear and elongational flows. *The Journal of Chemical Physics*, *136*(6), 064105. https://doi.org/10.1063/1.3684753

Hekmat, D., Hebel, D., Schmid, H., & Weuster-Botz, D. (2007). Crystallization of lysozyme: From vapor diffusion experiments to batch crystallization in agitated ml-scale vessels. *Process Biochemistry*, *42*(12), 1649–1654. https://doi.org/10.1016/j.procbio.2007.10.001

Helfand, E. (1960). Transport Coefficients from Dissipation in a Canonical Ensemble. *Physical Review*, *119*(1), 1–9. https://doi.org/10.1103/PhysRev.119.1

Hemrajani, R. R., & Tatterson, G. B. (2003). Mechanically Stirred Vessels. In *Handbook of Industrial Mixing* (pp. 345–390). John Wiley & Sons, Ltd. https://doi.org/10.1002/0471451452.ch6

Hendrikse, R., Bayly, A., & Jimack, P. (2023). Anionic surfactant solutions under shear using dissipative particle dynamics. *Journal of Chemical Physics*.

Hirschberg, S., Koubek, R., F.Moser, & Schöck, J. (2009). An improvement of the Sulzer SMX™ static mixer significantly reducing the pressure drop. *Chemical Engineering Research and Design*, *87*(4), 524–532. https://doi.org/10.1016/j.cherd.2008.12.021

Jung, G., & Schmid, F. (2016). Computing bulk and shear viscosities from simulations of fluids with dissipative and stochastic interactions. *The Journal of Chemical Physics*, *144*(20), 204104. https://doi.org/10.1063/1.4950760

Junghans, C., Praprotnik, M., & Kremer, K. (2007). Transport properties controlled by a thermostat: An extended dissipative particle dynamics thermostat. *Soft Matter*, *4*(1), 156–161. https://doi.org/10.1039/B713568H

Kabanov, A. V., Batrakova, E. V., & Alakhov, V. Y. (2002). Pluronic® block copolymers as novel polymer therapeutics for drug and gene delivery. *Journal of Controlled Release*, *82*(2), 189–212. https://doi.org/10.1016/S0168-3659(02)00009-3

Kagoshima, M., & Mann, R. (2006). Development of a networks-of-zones fluid mixing model for an unbaffled stirred vessel used for precipitation. *Chemical Engineering Science*, *61*(9), 2852–2863. https://doi.org/10.1016/j.ces.2005.11.054

Khimani, M., Patel, H., Patel, V., Parekh, P., & Vekariya, R. L. (2020). Self-assembly of stimuli-responsive block copolymers in aqueous solutions: An overview. *Polymer Bulletin*, *77*(11), 5783–5810. https://doi.org/10.1007/s00289-019-03046-w

Kilara, A., & Sharkasi, T. (1994). Microstructure and Processing of Ice Cream. *MRS Bulletin*, *19*(7), 51–55. https://doi.org/10.1557/S0883769400047564

Klein, K., & Palefsky, I. (2007). C.2 - Shampoo Formulation. In I. Johansson & P. Somasundaran (Eds.), *Handbook for Cleaning/Decontamination of Surfaces* (pp. 277–304). Elsevier Science B.V. https://doi.org/10.1016/B978-044451664-0/50008-5

Koelman, J. M. V. A., & Hoogerbrugge, P. J. (1993). Dynamic Simulations of Hard-Sphere Suspensions Under Steady Shear. *Europhysics Letters*, *21*(3), 363. https://doi.org/10.1209/0295-5075/21/3/018

Kong, Y., Manke, C., Madden, W., & Schlijper, A. (1997). Modeling the rheology of polymer solutions by dissipative particle dynamics. *Tribology Letters*, *3*(1), 133–138. https://doi.org/10.1023/A:1019196014223

Kubo, R. (1957). Statistical-mechanical theory of irreversible processes. i. general theory and simple applications to magnetic and conduction problems. *Journal of the physical society of Japan*, *12*(6), 570–586. https://doi.org/10.1143/JPSJ.12.570

Laba, D. (1993). *Rheological properties of cosmetics and toiletries*. Dekker.

Lamberto, D. J., Alvarez, M. M., & Muzzio, F. J. (1999). Experimental and computational investigation of the laminar flow structure in a stirred tank. *Chemical Engineering Science*, *54*(7), 919–942. https://doi.org/10.1016/S0009-2509(98)00275-9

Larson, R. G. (1999, January). *The Structure and Rheology of Complex Fluids*. Oxford University Press.

Lauriello, N., Boccardo, G., Marchisio, D., Lísal, M., & Buffo, A. (2023). Development of an automated reliable method to compute transport properties from DPD equilibrium simulations: Application to simple fluids. *Computer Physics Communications*, *291*, 108843. https://doi.org/10.1016/j.cpc.2023.108843

Lauriello, N., Kondracki, J., Buffo, A., Boccardo, G., Bouaifi, M., Lisal, M., & Marchisio, D. (2021). Simulation of high Schmidt number fluids with dissipative particle dynamics: Parameter identification and robust viscosity evaluation. *Physics of Fluids*, *33*(7), 073106. https://doi.org/10.1063/5.0055344

Lees, A. W., & Edwards, S. F. (1972). The computer study of transport processes under extreme conditions. *Journal of Physics C: Solid State Physics*, *5*(15), 1921–1928. https://doi.org/10.1088/0022-3719/5/15/006

Li, C., Fu, X., Zhong, W., & Liu, J. (2019). Dissipative Particle Dynamics Simulations of a Protein-Directed Self-Assembly of Nanoparticles. *ACS Omega*, *4*(6), 10216–10224. https://doi.org/10.1021/acsomega.9b01078

Li, H., Dang, L., Yang, S., Li, J., & Wei, H. (2016). The study of phase behavior and rheological properties of lyotropic liquid crystals in the LAS/AES/H2O system. *Colloids and Surfaces A: Physicochemical and Engineering Aspects*, *495*, 221–228. https://doi.org/10.1016/j.colsurfa.2016.01.055

Liu, S., Hrymak, A. N., & Wood, P. E. (2006). Laminar mixing of shear thinning fluids in a SMX static mixer. *Chemical Engineering Science*, *61*(6), 1753–1759. https://doi.org/10.1016/j.ces.2005.10.026

Lowe, C. P. (1999). An alternative approach to dissipative particle dynamics. *Europhysics Letters*, *47*(2), 145. https://doi.org/10.1209/epl/i1999-00365-x

Maffioli, L., Ewen, J., Smith, E., Varghese, S., Daivis, P., Dini, D., & Todd, B. (2024, January). Ttcf4lammps: A Toolkit for Simulation of the Non-Equilibrium Behaviour of Molecular Fluids at Experimentally Accessible Shear Rates. https://doi.org/10.2139/ssrn.4686202

Marsh, C. A., Backx, G., & Ernst, M. H. (1997). Static and dynamic properties of dissipative particle dynamics. *Physical Review E*, *56*(2), 1676–1691. https://doi.org/10.1103/PhysRevE.56.1676

Meng, S., Zhang, J., Wang, Y., Li, X., Wu, C., Hou, T., Xiao, L., & Lu, G. (2015). Simulating the rheology of surfactant solution using dissipative particle dynamics. *Molecular Simulation*, *41*(9), 772–778. https://doi.org/10.1080/08927022.2014.935373

Metzner, A. B., & Reed, J. C. (1955). Flow of non-newtonian fluids—correlation of the laminar, transition, and turbulent-flow regions. *AIChE Journal*, *1*(4), 434–440. https://doi.org/10.1002/aic.690010409

Metzner, A. B., & Taylor, J. S. (1960). Flow patterns in agitated vessels. *AIChE Journal*, *6*(1), 109–114. https://doi.org/10.1002/aic.690060121

Mewis, J., & Wagner, N. J. (2011). *Colloidal Suspension Rheology*. Cambridge University Press. https://doi.org/10.1017/CBO9780511977978

Montante, G., Lee, K. C., Brucato, A., & Yianneskis, M. (2001). Numerical simulations of the dependency of flow pattern on impeller clearance in stirred vessels. *Chemical Engineering Science*, *56*(12), 3751–3770. https://doi.org/10.1016/S0009-2509(01)00089-6

Nafar Sefiddashti, M. H., Boudaghi-Khajehnobar, M., Edwards, B. J., & Khomami, B. (2020). High-fidelity scaling relationships for determining dissipative particle dynamics parameters from atomistic molecular dynamics simulations of polymeric liquids. *Scientific Reports*, *10*(1), 4458. https://doi.org/10.1038/s41598-020-61374-8

Nagata, S., Nishikawa, M., Inoue, A., & Okamoto, Y. (1975). Turbulence in non-baffled mixing vessel. *Journal of Chemical Engineering of Japan*, *8*(3), 243–248.

Nyande, B. W., Mathew Thomas, K., & Lakerveld, R. (2021). CFD Analysis of a Kenics Static Mixer with a Low Pressure Drop under Laminar Flow Conditions. *Industrial & Engineering Chemistry Research*, *60*(14), 5264–5277. https://doi.org/10.1021/acs.iecr.1c00135

Pan, G., & McCabe, C. (2006). Prediction of viscosity for molecular fluids at experimentally accessible shear rates using the transient time correlation function formalism. *The Journal of Chemical Physics*, *125*(19), 194527. https://doi.org/10.1063/1.2364899

Pandya, N., Rajput, G., Janni, D. S., Subramanyam, G., Ray, D., Aswal, V., & Varade, D. (2021). SLES/CMEA mixed surfactant system: Effect of electrolyte on interfacial behavior and microstructures in aqueous media. *Journal of Molecular Liquids*, *325*, 115096. https://doi.org/10.1016/j.molliq.2020.115096

Panoukidou, M., R. Wand, C., & Carbone, P. (2021). Comparison of equilibrium techniques for the viscosity calculation from DPD simulations. *Soft Matter*, *17*(36), 8343–8353. https://doi.org/10.1039/D1SM00891A

Panoukidou, M., Wand, C. R., Del Regno, A., Anderson, R. L., & Carbone, P. (2019). Constructing the phase diagram of sodium laurylethoxysulfate using dissipative particle dynamics. *Journal of Colloid and Interface Science*, *557*, 34–44. https://doi.org/10.1016/j.jcis.2019.08.091

Parker, E. N. (1954). Tensor Virial Equations. *Physical Review*, *96*(6), 1686–1689. https://doi.org/10.1103/PhysRev.96.1686

Pasquino, R., Droghetti, H., Carbone, P., Mirzaagha, S., Grizzuti, N., & Marchisio, D. (2019). An experimental rheological phase diagram of a tri-block co-polymer in water validated against dissipative particle dynamics simulations. *Soft Matter*, *15*(6), 1396–1404. https://doi.org/10.1039/C8SM01959B

Pedregosa, F., Varoquaux, G., Gramfort, A., Michel, V., Thirion, B., Grisel, O., Blondel, M., Prettenhofer, P., Weiss, R., Dubourg, V., Vanderplas, J., Passos, A., Cournapeau, D., Brucher, M., Perrot, M., & Duchesnay, É. (2011). Scikit-learn: Machine Learning in Python. *Journal of Machine Learning Research*, *12*(85), 2825–2830.

Pianko-Oprych, P., & Jaworski, Z. (2009). CFD modelling of two-phase liquid-liquid flow in a SMX static mixer. *Polish Journal of Chemical Technology*, *11*(3), 41–49. https://doi.org/10.2478/v10026-009-0034-x

Pieczywek, P. M., Płaziński, W., & Zdunek, A. (2020). Dissipative particle dynamics model of homogalacturonan based on molecular dynamics simulations.

Scientific Reports, *10*(1), 14691. https://doi.org/10.1038/s41598-020-71820-2

Prhashanna, A., Khan, S. A., & Chen, S. B. (2015). Co-Micellization Behavior in Poloxamers: Dissipative Particle Dynamics Study. *The Journal of Physical Chemistry B*, *119*(2), 572–582. https://doi.org/10.1021/jp509237r

Prhashanna, A., Khan, S. A., & Chen, S. B. (2016). Micelle morphology and chain conformation of triblock copolymers under shear: LA-DPD study. *Colloids and Surfaces A: Physicochemical and Engineering Aspects*, *506*, 457–466. https://doi.org/10.1016/j.colsurfa.2016.07.003

Rasmussen, C. E., & Williams, C. K. I. (2005, November). *Gaussian Processes for Machine Learning*. https://doi.org/10.7551/mitpress/3206.001.0001

Rodriguez, S., & Cardiff, P. (2022). A general approach for running Python codes in OpenFOAM using an embedded pybind11 Python interpreter. (arXiv:2203.16394). https://doi.org/10.48550/arXiv.2203.16394

Rushton, J. H., Costich, W., E., & Everett, J., H. (1950). Characteristics of Mixing Impellers Part1 and Part2. *Chemical Engineering Progres*, *46*, 467–476.

Sanderson, S., & Searles, D. J. (2025). On the importance of numerical integration details for homogeneous flow simulation. (arXiv:2512.01318). https://doi.org/10.48550/arXiv.2512.01318

Santo, K. P., Vishnyakov, A., Kumar, R., & Neimark, A. V. (2018). Elucidating the Effects of Metal Complexation on Morphological and Rheological Properties of Polymer Solutions by a Dissipative Particle Dynamics Model. *Macromolecules*, *51*(14), 4987–5000. https://doi.org/10.1021/acs.macromol.8b00493

Scargiali, F., Busciglio, A., Grisafi, F., & Brucato, A. (2014). Mass transfer and hydrodynamic characteristics of unbaffled stirred bio-reactors: Influence of impeller design. *Biochemical Engineering Journal*, *82*, 41–47. https://doi.org/10.1016/j.bej.2013.11.009

Scargiali, F., Tamburini, A., Caputo, G., & Micale, G. (2017). On the assessment of power consumption and critical impeller speed in vortexing unbaffled stirred tanks. *Chemical Engineering Research and Design*, *123*, 99–110. https://doi.org/10.1016/j.cherd.2017.04.035

Scargiali, F., Busciglio, A., Grisafi, F., Tamburini, A., Micale, G., & Brucato, A. (2013). Power Consumption in Uncovered Unbaffled Stirred Tanks: Influence of the Viscosity and Flow Regime. *Industrial & Engineering Chemistry Research*, *52*(42), 14998–15005. https://doi.org/10.1021/ie402466w

Son, G. E., Sugartseren, N., Yoon, W.-B., & Kwak, S. K. (2014). Phase Behavior of Ternary Mixtures of Water–Vanillin–Ethanol for Vanillin Extraction via Dissipative Particle Dynamics. *Journal of Chemical & Engineering Data*, *59*(10), 3036–3040. https://doi.org/10.1021/je5001186

Štern, P., Valentová, H., & Pokorný, J. (2001). Rheological properties and sensory texture of mayonnaise. *European Journal of Lipid Science and Technology*, *103*(1), 23–28. https://doi.org/10.1002/1438-9312(200101)103:1<23::AID-EJLT23>3.0.CO;2-P

Stobiac, V., Fradette, L., Tanguy, P. A., & Bertrand, F. (2014). Pumping characterisation of the maxblend impeller for Newtonian and strongly non-Newtonian fluids. *The Canadian Journal of Chemical Engineering*, *92*(4), 729–741. https://doi.org/10.1002/cjce.21906

Stoyanov, S. D., & Groot, R. D. (2005). From molecular dynamics to hydrodynamics: A novel Galilean invariant thermostat. *The Journal of Chemical Physics*, *122*(11), 114112. https://doi.org/10.1063/1.1870892

Tamburini, A., Gagliano, G., Micale, G., Brucato, A., Scargiali, F., & Ciofalo, M. (2018). Direct numerical simulations of creeping to early turbulent flow in unbaffled and baffled stirred tanks. *Chemical Engineering Science*, *192*, 161–175. https://doi.org/10.1016/j.ces.2018.07.023

Tamburini, A., Gagliano, G., Scargiali, F., Micale, G., Brucato, A., & Ciofalo, M. (2019). CFD Simulation of Radially Stirred Baffled and Unbaffled Stirred Tanks. *Chemical Engineering Transactions*, *74*, 1033–1038. https://doi.org/10.3303/CET1974173

Thompson, A. P., Aktulga, H. M., Berger, R., Bolintineanu, D. S., Brown, W. M., Crozier, P. S., in 't Veld, P. J., Kohlmeyer, A., Moore, S. G., Nguyen, T. D., Shan, R., Stevens, M. J., Tranchida, J., Trott, C., & Plimpton, S. J. (2022). LAMMPS - a flexible simulation tool for particle-based materials modeling at the atomic, meso, and continuum scales. *Computer Physics Communications*, *271*, 108171. https://doi.org/10.1016/j.cpc.2021.108171

Todd, B. D., & Daivis, P. J. (2017). *Nonequilibrium Molecular Dynamics: Theory, Algorithms and Applications*. Cambridge University Press. https://doi.org/10.1017/9781139017848

W. Jakob, J. Rhinelander, D. Moldovan and others. (2017). pybind11 – seamless operability between c++11 and python.

Wand, C. R., Panoukidou, M., Del Regno, A., Anderson, R. L., & Carbone, P. (2020). The Relationship between Wormlike Micelle Scission Free Energy and Micellar Composition: The Case of Sodium Lauryl Ether Sulfate and

Cocamidopropyl Betaine. *Langmuir*, *36*(41), 12288–12298. https://doi.org/10.1021/acs.langmuir.0c02210

Wang, J. (2023). An Intuitive Tutorial to Gaussian Process Regression. *Computing in Science & Engineering*, *25*(4), 4–11. https://doi.org/10.1109/MCSE.2023.3342149

Weeks, J. D., Chandler, D., & Andersen, H. C. (1971). Role of Repulsive Forces in Determining the Equilibrium Structure of Simple Liquids. *The Journal of Chemical Physics*, *54*(12), 5237–5247. https://doi.org/10.1063/1.1674820

Yuan, S.-L., Cai, Z.-T., Xu, G.-Y., & Jiang, Y.-S. (2002). Mesoscopic simulation study on phase diagram of the system oil/water/aerosol OT. *Chemical Physics Letters*, *365*(3), 347–353. https://doi.org/10.1016/S0009-2614(02)01494-X

Zhao, L., Li, Z., Caswell, B., Ouyang, J., & Karniadakis, G. E. (2018). Active learning of constitutive relation from mesoscopic dynamics for macroscopic modeling of non-Newtonian flows. *Journal of Computational Physics*, *363*, 116–127. https://doi.org/10.1016/j.jcp.2018.02.039

Zhao, L., Li, Z., Wang, Z., Caswell, B., Ouyang, J., & Karniadakis, G. E. (2021). Active- and transfer-learning applied to microscale-macroscale coupling to simulate viscoelastic flows. *Journal of Computational Physics*, *427*, 110069. https://doi.org/10.1016/j.jcp.2020.110069

Appendix A

Parameter for the UB75 DPD model

Table A.1 List of conservative repulsive parameter a_{ij} and cutoff radius $r_{c,ij}$ for each pair of beads.

Bead i	Bead j	conservative coefficient a_{ij}	cutoff radius $r_{c,ij}$
$[H_2O]$	$[H_2O]$	25.0	1.000
$[CH_3]$	$[CH_3]$	24.0	0.955
$[CH_2CH_2]$	$[CH_2CH_2]$	22.0	1.074
$[CH_2OCH_2]$	$[CH_2OCH_2]$	25.5	1.116
$[CH_2OSO_3^-]$	$[CH_2OSO_3^-]$	13.30	1.234
[Na]	[Na]	25.00	1.000
$[CH_3CH_2]$	$[CH_3CH_2]$	22.00	1.098
$[CH_2CONHCH_2]$	$[CH_2CONHCH_2]$	22.00	1.218
$[CH_2OH]$	$[CH_2OH]$	14.00	0.980
$[H_2O]$	$[CH_3]$	45.00	0.977
$[H_2O]$	$[CH_2CH_2]$	45.00	1.037
$[H_2O]$	$[CH_3]$	24.00	1.058
$[H_2O]$	$[CH_2OCH_2]$	17.90	1.117
$[H_2O]$	$[CH_2OSO_3^-]$	25.00	1.000
$[H_2O]$	[Na]	45.00	1.049
$[H_2O]$	$[CH_3CH_2]$	19.00	1.109
$[H_2O]$	$[CH_2OH]$	14.50	0.990
$[CH_3]$	$[CH_2CH_2]$	23.00	1.014

Table A.1 (continued): List of conservative repulsive parameter a_{ij} and cutoff radius $r_{c,ij}$ for each pair of beads.

Bead i	Bead j	conservative coefficient a_{ij}	cut-off radius $r_{c,ij}$
$[CH_3]$	$[CH_2OCH_2]$	28.50	1.020
$[CH_3]$	$[CH_2OSO_3^-]$	28.50	1.071
$[CH_3]$	[Na]	45.00	0.962
$[CH_3]$	$[CH_3CH_2]$	23.00	1.026
$[CH_3]$	$[CH_2CONHCH_2]$	32.00	1.086
$[CH_3]$	$[CH_2OH]$	26.00	0.967
$[CH_2CH_2]$	$[CH_2OCH_2]$	28.50	1.095
$[CH_2CH_2]$	$[CH_2OSO_3^-]$	28.50	1.154
$[CH_2CH_2]$	[Na]	45.50	1.037
$[CH_2CH_2]$	$[CH_3CH_2]$	22.00	1.086
$[CH_2CH_2]$	$[CH_2CONHCH_2]$	32.00	1.146
$[CH_2CH_2]$	$[CH_2OH]$	26.00	1.027
$[CH_2OCH_2]$	$[CH_2OSO_3^-]$	15.50	1.175
$[CH_2OCH_2]$	[Na]	24.00	1.058
$[CH_2OCH_2]$	$[CH_3CH_2]$	28.50	1.107
$[CH_2OCH_2]$	$[CH_2CONHCH_2]$	15.73	1.167
$[CH_2OCH_2]$	$[CH_2OH]$	25.00	1.059
$[CH_2OSO_3^-]$	[Na]	17.90	1.117
$[CH_2OSO_3^-]$	$[CH_3CH_2]$	28.50	1.166
$[CH_2OSO_3^-]$	$[CH_2CONHCH_2]$	13.57	1.226
$[CH_2OSO_3^-]$	$[CH_2OH]$	21.70	1.048
[Na]	$[CH_3CH_2]$	45.00	1.049
[Na]	$[CH_2CONHCH_2]$	18.33	1.109
[Na]	$[CH_2OH]$	25.80	0.990
$[CH_3CH_2]$	$[CH_2CONHCH_2]$	32.00	1.158
$[CH_3CH_2]$	$[CH_2OH]$	26.00	1.038
$[CH_2CONHCH_2]$	$[CH_2OH]$	26.00	1.099

Appendix B

Mappings with the DPD force field

As reported in Section 4.2, the dissipation function at time zero, $\langle\Omega(0)\rangle$, must be equal to zero to use the TTCF in non-equilibrium simulations. For a system with simple shear applied in the xy plane, Ω is described by Equation (4.3), here repeated:

$$\Omega = -\frac{\dot{\gamma}V}{k_B T} P_{xy}. \tag{B.1}$$

Consequently, to have $\langle\Omega(0)\rangle = 0$, it must be true that $\langle P_{xy}(0)\rangle = 0$. This condition is verified for a physical system, since $t = 0$ corresponds to an equilibrium condition, but it is practically impossible to obtain by averaging a finite number of samples. In Lennard-Jones systems, this issue can be resolved by using the following mappings:

$$\mathbf{\Gamma}_i = (\mathbf{x}, \mathbf{y}, \mathbf{z}, \mathbf{p}_x, \mathbf{p}_y, \mathbf{p}_z) \tag{B.2}$$

$$\mathbf{\Gamma}_i^{\mathrm{I}} = (\mathbf{x}, \mathbf{y}, \mathbf{z}, -\mathbf{p}_x, -\mathbf{p}_y, -\mathbf{p}_z) \tag{B.3}$$

$$\mathbf{\Gamma}_i^{\mathrm{II}} = (-\mathbf{x}, \mathbf{y}, \mathbf{z}, -\mathbf{p}_x, \mathbf{p}_y, \mathbf{p}_z) \tag{B.4}$$

$$\mathbf{\Gamma}_i^{\mathrm{III}} = (-\mathbf{x}, \mathbf{y}, \mathbf{z}, \mathbf{p}_x, -\mathbf{p}_y, -\mathbf{p}_z), \tag{B.5}$$

which generate values of $P_{yx}(0)$ equal in modulus and opposite in sign for the mapped trajectories, giving zero as a result. It is possible to show that these mappings are not suitable for DPD systems, due to the presence of the dissipative and random forces. In LAMMPS, the pressure tensor $\mathbf{P}$ is calculated using the Irving-Kirkwood formula and is always considered symmetric. Hence, the $P_{yx} = P_{xy}$ element of the pressure

tensor is computed as Thompson et al., 2022:

$$P_{xy} = \frac{1}{V}\sum_{k=1}^{N} m_k c_{k,x} c_{k,y} + \frac{1}{V}\sum_{k=1}^{N'} r_{kx} f_{ky}, \tag{B.6}$$

where the subscript k refers to the k-th particle, and $N \neq N'$ due to periodic boundary conditions and communications between processors. The first sum in Equation (B.6) is the kinetic contribution, while the second is the configurational contribution, or the virial term. The value of P_{xy} is equal to zero at a certain time if both contributions are equal to zero. Using the mappings of Equation (4.6), the kinetic terms of the mapped trajectories are:

$$(p_{k,x}, p_{k,y}, p_{k,z}) \rightarrow \sum_{k=1}^{N} m_k c_{k,x} c_{k,y} \tag{B.7}$$

$$(-p_{k,x}, -p_{k,y}, -p_{k,z}) \rightarrow \sum_{k=1}^{N} m_k (-c_{k,x})(-c_{k,y}) = \sum_{k=1}^{N} m_k c_{k,x} c_{k,y} \tag{B.8}$$

$$(-p_{k,x}, p_{k,y}, p_{k,z}) \rightarrow \sum_{k=1}^{N} m_k (-c_{k,x}) c_{k,y} = -\sum_{k=1}^{N} m_k c_{k,x} c_{k,y} \tag{B.9}$$

$$(-p_{k,x}, -p_{k,y}, -p_{k,z}) \rightarrow \sum_{k=1}^{N} m_k c_{k,x} (-c_{k,y}) = -\sum_{k=1}^{N} m_k c_{k,x} c_{k,y}, \tag{B.10}$$

leading to a zero averaged value for the kinetic contribution to P_{xy}. The contribution of the configurational part can be studied by considering the forces acting on a single bead k. Indeed, for the mappings to work, the sum of the virial terms obtained with the different mappings must be zero for every particle. To simplify the problem, the following consider the interaction of the bead k with only one bead l.

The conservative (Equation (2.16)) and random (Equation (2.18)) forces depend only on the relative position, hence the focus can be put on the transformation of the positions:

$$\mathbf{\Gamma}_i = (\mathbf{x}, \mathbf{y}, \mathbf{z}) \tag{B.11}$$

$$\mathbf{\Gamma}_i^{\mathrm{I}} = (\mathbf{x}, \mathbf{y}, \mathbf{z}) \tag{B.12}$$

$$\mathbf{\Gamma}_i^{\mathrm{II}} = (-\mathbf{x}, \mathbf{y}, \mathbf{z}) \tag{B.13}$$

$$\mathbf{\Gamma}_i^{\mathrm{III}} = (-\mathbf{x}, \mathbf{y}, \mathbf{z}) \tag{B.14}$$

Having only one type of bead, the conservative force between beads k and l is:

$$\mathbf{f}_{kl}^{C} = a w_C(r_{kl}) \hat{\mathbf{r}}_{kl}. \tag{B.15}$$

From this equation, r_{kl} and $\hat{\mathbf{r}}_{kl}$ can be expressed in an explicit form:

$$\mathbf{r}_k = (x_k, y_k, z_k), \tag{B.16}$$

$$\mathbf{r}_l = (x_l, y_l, z_l), \tag{B.17}$$

$$\mathbf{r}_{kl} = (x_k - x_l, y_k - y_l, z_k - z_l) = (x_{kl}, y_{kl}, z_{kl}), \tag{B.18}$$

$$r_{kl} = |\mathbf{r}_{kl}| = \sqrt{x_{kl}^2 + y_{kl}^2 + z_{kl}^2}, \tag{B.19}$$

$$\hat{\mathbf{r}}_{kl} = \frac{\mathbf{r}_{kl}}{r_{kl}} = \left(\frac{x_k - x_l}{r_{kl}}, \frac{y_k - y_l}{r_{kl}}, \frac{z_k - z_l}{r_{kl}} \right). \tag{B.20}$$

Then, the weight function w_C, for $r_{kl} \leq r_c$, is:

$$w_C(r_{kl}) = \left(1 - \frac{r_{kl}}{r_c} \right) = \left(1 - \frac{\sqrt{(x_k - x_l)^2 + (y_k - y_l)^2 + (z_k - z_l)^2}}{r_c} \right). \tag{B.21}$$

When comparing Equation (B.21) with the mapping in Equation (B.11), it is possible to notice that the weight function $w_C(r_{kl})$ does not depend on the mappings, since it contains only squared differences. The results from mappings I and II are identical and equal to the following:

$$\mathbf{f}_{kl}^{C,\mathrm{I,II}} = a w_C(r_{kl}) \left(\frac{x_k - x_l}{r_{kl}}, \frac{y_k - y_l}{r_{kl}}, \frac{z_k - z_l}{r_{kl}} \right). \tag{B.22}$$

In the case of mappings III and IV, the conservative force on bead k due to the interaction with bead l is:

$$\mathbf{f}_{kl}^{C,\mathrm{III,IV}} = a w_C(r_{kl}) \left(\frac{-x_k + x_l}{r_{kl}}, \frac{y_k - y_l}{r_{kl}}, \frac{z_k - z_l}{r_{kl}} \right). \tag{B.23}$$

From Equation (B.6), the virial term is calculated as the sum of the products of the x component of the position vector times the y component of the force. The latter force is the same for all the mappings:

$$f_{kl,y}^{C} = f_{k,y}^{C} = a w_C(r_{kl}) \left(\frac{y_k - y_l}{r_{kl}} \right), \tag{B.24}$$

and the sum is:

$$\begin{aligned}\sum_{\text{mappings}} r_{k,x} f^C_{k,y} &= f^C_{k,y} \sum_{\text{mappings}} r_{k,x} \\ &= f^C_{k,y}(r^{\text{I}}_{k,x} + r^{\text{II}}_{k,x} + r^{\text{III}}_{k,x} + r^{\text{IV}}_{k,x}) \\ &= f^C_{k,y}(x_k + x_k - x_k - x_k) \\ &= 0.\end{aligned} \tag{B.25}$$

The same argument can be applied to the random force, which has the same weight function as the conservative force, so that what was said for Equation (B.21) is also valid in this case.

$$\mathbf{f}^R_{kl} = \sigma w_R(r_{kl}) \frac{\xi_{kl}}{\sqrt{\Delta t}} \hat{\mathbf{r}}_{kl} \tag{B.26}$$

In this case, an additional condition must be imposed on the generation of the random numbers. In order for the forces to cancel out in the sum, the value of ξ_{kl} must be the same for all the mapped trajectories. If the generated random number ξ_{kl} is correctly set in all mapped trajectories, the random force has identical values for mapping I and II:

$$\mathbf{f}^{R,\text{I,II}}_{kl} = \sigma w_R(r_{kl}) \frac{\xi_{kl}}{\sqrt{\Delta t}} \left(\frac{x_k - x_l}{r_{kl}}, \frac{y_k - y_l}{r_{kl}}, \frac{z_k - z_l}{r_{kl}} \right), \tag{B.27}$$

and for mappings III and IV:

$$\mathbf{f}^{R,\text{III,IV}}_{kl} = \sigma w_R(r_{kl}) \frac{\xi_{kl}}{\sqrt{\Delta t}} \left(\frac{-x_k + x_l}{r_{kl}}, \frac{y_k - y_l}{r_{kl}}, \frac{z_k - z_l}{r_{kl}} \right). \tag{B.28}$$

In addition, the calculation for the virial term is identical to the one in Equation (B.25), since the y component of the force is the same for all mappings:

$$f^R_{kl,y} = f^R_{k,y} = a w_R(r_{kl}) \left(\frac{y_k - y_l}{r_{kl}} \right), \tag{B.29}$$

$$\begin{aligned}\sum_{\text{mappings}} r_{k,x} f^R_{k,y} &= f^R_{k,y} \sum_{\text{mappings}} r_{k,x} \\ &= f^R_{k,y}(r^{\text{I}}_{k,x} + r^{\text{II}}_{k,x} + r^{\text{III}}_{k,x} + r^{\text{IV}}_{k,x}) \\ &= f^C_{k,y}(x_k + x_k - x_k - x_k) \\ &= 0.\end{aligned} \tag{B.30}$$

Unlike the conservative and random forces, the dissipative force depends on the relative velocity between the two beads:

$$\mathbf{f}_{kl}^{D} = -\gamma w_D(r_{kl})(\hat{\mathbf{r}}_{kl} \cdot \mathbf{v}_{kl})\hat{\mathbf{r}}_{kl}. \tag{B.31}$$

For this expression, it is possible to show that the mappings work as expected for a system at equilibrium, with no velocity field imposed. When a shear is applied to the box, the velocity profile breaks the symmetry imposed by the mappings, and the elements in the sum for virial term do not cancel out. In the nonequilibrium simulation, the velocity $\mathbf{v}$ of a bead will be the sum of the streaming velocity $\mathbf{u}(y)$, the consequence of the shear imposition, and the peculiar velocity $\mathbf{c}$. For a bead k:

$$\mathbf{v}_k = \mathbf{c}_k + \mathbf{u}_k(y), \tag{B.32}$$

or, in component form:

$$(v_{k,x}, v_{k,y}, v_{k,z}) = (c_{k,x}, c_{k,y}, c_{k,z}) + (\dot{\gamma} y_k, 0, 0) = (c_{k,x} + \dot{\gamma} y_k, c_{k,y}, c_{k,z}) \tag{B.33}$$

From this definition, the relative velocity $\mathbf{v}_{kl}$ between beads k and l can be calculated:

$$\mathbf{v}_k = (c_{k,x} + \dot{\gamma} y_k, c_{k,y}, c_{k,z}), \tag{B.34}$$

$$\mathbf{v}_l = (c_{l,x} + \dot{\gamma} y_l, c_{l,y}, c_{l,z}), \tag{B.35}$$

$$\mathbf{v}_{kl} = (c_{k,x} + \dot{\gamma} y_k - c_{l,x} - \dot{\gamma} y_l, c_{k,y} - c_{l,y}, c_{k,z} - c_{l,z}) \tag{B.36}$$

As for conservative and random forces, r_{kl} is not affected by the position transform, and the weight function $w_D(r_{kl})$ has the same value for all mappings. The next step is the evaluation of the dot product $(\hat{\mathbf{r}}_{kl} \cdot \mathbf{v}_{kl})$, which must be carried out for each mapping. It should be noted that only the peculiar velocity $\mathbf{c}_k$ is affected by the transformations, since the mappings are applied to the equilibrium system before imposing the shear.

In the case of the original equilibrium trajectory, that is, mapping I ($\mathbf{x}, \mathbf{y}, \mathbf{z}, \mathbf{p}_x, \mathbf{p}_y, \mathbf{p}_z$):

$$
\begin{aligned}
\hat{\mathbf{r}}_{kl} \cdot \mathbf{v}_{kl} &= \\
&= \left(\frac{x_k - x_l}{r_{kl}}, \frac{y_k - y_l}{r_{kl}}, \frac{z_k - z_l}{r_{kl}} \right) \\
&\quad \cdot \left(c_{k,x} + \dot{\gamma} y_k - c_{l,x} - \dot{\gamma} y_l, c_{k,y} - c_{l,y}, c_{k,z} - c_{l,z} \right) \\
&= \frac{1}{r_{kl}} \left[(x_k - x_l)(c_{k,x} + \dot{\gamma} y_k - c_{l,x} - \dot{\gamma} y_l) \right. \\
&\quad \left. + (y_k - y_l)(c_{k,y} - c_{l,y}) + (z_k - z_l)(c_{k,z} - c_{l,z}) \right] \\
&= \frac{1}{r_{kl}} \left[(x_k - x_l)(c_{k,x} - c_{l,x}) + \dot{\gamma}(x_k - x_l)(y_k - y_l) + \mathcal{D}_y + \mathcal{D}_z \right] \\
&= \frac{1}{r_{kl}} (\mathcal{D}_x + \mathcal{D}_y + \mathcal{D}_z) + \frac{\dot{\gamma}(x_k - x_l)(y_k - y_l)}{r_{kl}} \\
&= \mathcal{D} + \frac{\dot{\gamma}(x_k - x_l)(y_k - y_l)}{r_{kl}} \\
&= \mathcal{D} + \mathcal{A}.
\end{aligned}
\tag{B.37}
$$

To simplify the notation, the groups $\mathcal{D}_i$, with $i = x, y, z$, $\mathcal{D}$, and $\mathcal{A}$ are introduced:

$$\mathcal{D}_i = (i_k - i_l)(u_k - u_l), \tag{B.38}$$

$$\mathcal{D} = \frac{\mathcal{D}_x + \mathcal{D}_y + \mathcal{D}_z}{r_{kl}}, \tag{B.39}$$

$$\mathcal{A} = \frac{\dot{\gamma}(x_k - x_l)(y_k - y_l)}{r_{kl}}. \tag{B.40}$$

For mapping II ($\mathbf{x}, \mathbf{y}, \mathbf{z}, -\mathbf{p}_x, -\mathbf{p}_y, -\mathbf{p}_z$):

$$
\begin{aligned}
\hat{\mathbf{r}}_{kl} \cdot \mathbf{v}_{kl} &= \\
&= \left(\frac{x_k - x_l}{r_{kl}}, \frac{y_k - y_l}{r_{kl}}, \frac{z_k - z_l}{r_{kl}} \right) \\
&\quad \cdot \left(-c_{k,x} + \dot{\gamma} y_k + c_{l,x} - \dot{\gamma} y_l, -c_{k,y} + c_{l,y}, -c_{k,z} + c_{l,z} \right) \\
&= \frac{1}{r_{kl}} \left(-\mathcal{D}_x - \mathcal{D}_y - \mathcal{D}_z \right) + \frac{\dot{\gamma}(x_k - x_l)(y_k - y_l)}{r_{kl}} \\
&= -\mathcal{D} + \mathcal{A}
\end{aligned}
\tag{B.41}
$$

Appling mapping III $(-\mathbf{x}, \mathbf{y}, \mathbf{z}, -\mathbf{p}_x, \mathbf{p}_y, \mathbf{p}_z)$:

$$\begin{aligned}\hat{\mathbf{r}}_{kl} \cdot \mathbf{v}_{kl} = & \\ &= \left(\frac{-x_k + x_l}{r_{kl}}, \frac{y_k - y_l}{r_{kl}}, \frac{z_k - z_l}{r_{kl}}\right) \\ &\quad \cdot \left(-c_{k,x} + \dot{\gamma} y_k + c_{l,x} - \dot{\gamma} y_l, c_{k,y} - c_{l,y}, c_{k,z} - c_{l,z}\right) \\ &= \frac{1}{r_{kl}}(\mathcal{D}_x + \mathcal{D}_y + \mathcal{D}_z) - \frac{\dot{\gamma}(x_k - x_l)(y_k - y_l)}{r_{kl}} \\ &= \mathcal{D} - \mathcal{A}\end{aligned} \tag{B.42}$$

With mapping IV $(-\mathbf{x}, \mathbf{y}, \mathbf{z}, \mathbf{p}_x, -\mathbf{p}_y, -\mathbf{p}_z)$:

$$\begin{aligned}\hat{\mathbf{r}}_{kl} \cdot \mathbf{v}_{kl} = & \\ &= \left(\frac{-x_k + x_l}{r_{kl}}, \frac{y_k - y_l}{r_{kl}}, \frac{z_k - z_l}{r_{kl}}\right) \\ &\quad \cdot \left(c_{k,x} + \dot{\gamma} y_k - c_{l,x} - \dot{\gamma} y_l, -c_{k,y} + c_{l,y}, -c_{k,z} + c_{l,z}\right) \\ &= \frac{1}{r_{kl}}(-\mathcal{D}_x - \mathcal{D}_y - \mathcal{D}_z) - \frac{\dot{\gamma}(x_k - x_l)(y_k - y_l)}{r_{kl}} \\ &= -\mathcal{D} - \mathcal{A}\end{aligned} \tag{B.43}$$

Writing explicitly the dissipative force for every mapping:

$$\mathbf{f}_{jk}^{D,\mathrm{I}} = -\gamma w_D(r_{kl})(\mathcal{D} + \mathcal{A}) \left(\frac{x_k - x_l}{r_{kl}}, \frac{y_k - y_l}{r_{kl}}, \frac{z_k - z_l}{r_{kl}}\right) \tag{B.44}$$

$$\mathbf{f}_{jk}^{D,\mathrm{II}} = -\gamma w_D(r_{kl})(-\mathcal{D} + \mathcal{A}) \left(\frac{x_k - x_l}{r_{kl}}, \frac{y_k - y_l}{r_{kl}}, \frac{z_k - z_l}{r_{kl}}\right) \tag{B.45}$$

$$\mathbf{f}_{jk}^{D,\mathrm{III}} = -\gamma w_D(r_{kl})(\mathcal{D} - \mathcal{A}) \left(\frac{-x_k + x_l}{r_{kl}}, \frac{y_k - y_l}{r_{kl}}, \frac{z_k - z_l}{r_{kl}}\right) \tag{B.46}$$

$$\mathbf{f}_{jk}^{D,\mathrm{IV}} = -\gamma w_D(r_{kl})(-\mathcal{D} - \mathcal{A}) \left(\frac{-x_k + x_l}{r_{kl}}, \frac{y_k - y_l}{r_{kl}}, \frac{z_k - z_l}{r_{kl}}\right) \tag{B.47}$$

The calculation of the virial term requires the y component of the force, which is not equal for all mappings, and assumes this form:

$$f_{kl,y}^{D} = f_{k,y}^{D} = -\gamma w_D(r_{kl})(\pm\mathcal{D} \pm \mathcal{A}) \left(\frac{y_k - y_l}{r_{kl}}\right). \tag{B.48}$$

To easily identify the terms that cancel out and write the sum in a more compact form, the group $\mathcal{A}$ is refactored and $\mathcal{B}$ is introduced:

$$\mathcal{A} = \frac{\dot{\gamma}(x_k - x_l)(y_k - y_l)}{r_{kl}} = \dot{\gamma}(x_k - x_l)\frac{(y_k - y_l)}{r_{kl}} = \mathcal{B}\frac{(y_k - y_l)}{r_{kl}}, \tag{B.49}$$

The result of the sum for the virial term is:

$$\begin{aligned}
\sum_{\text{mappings}} r_{k,x} f^D_{k,y} &= r^{\mathrm{I}}_{k,x} f^{D,\mathrm{I}}_{k,y} + r^{\mathrm{II}}_{k,x} f^{D,\mathrm{II}}_{k,y} + r^{\mathrm{III}}_{k,x} f^{D,\mathrm{III}}_{k,y} + r^{\mathrm{IV}}_{k,x} f^{D,\mathrm{IV}}_{k,y} \\
&= x_k \left[-\gamma w^D(r_{kl})(\mathcal{D} + \mathcal{A}) \left(\frac{y_k - y_l}{r_{kl}} \right) \right] \\
&\quad + x_k \left[-\gamma w^D(r_{kl})(-\mathcal{D} + \mathcal{A}) \left(\frac{y_k - y_l}{r_{kl}} \right) \right] \\
&\quad - x_k \left[-\gamma w^D(r_{kl})(\mathcal{D} - \mathcal{A}) \left(\frac{y_k - y_l}{r_{kl}} \right) \right] \\
&\quad - x_k \left[-\gamma w^D(r_{kl})(-\mathcal{D} - \mathcal{A}) \left(\frac{y_k - y_l}{r_{kl}} \right) \right] \\
&= -\gamma w^D(r_{kl}) \left(\frac{y_k - y_l}{r_{kl}} \right)^2 x_k \\
&\quad \cdot [(\mathcal{D} + \mathcal{B}) + (-\mathcal{D} + \mathcal{B}) - (\mathcal{D} - \mathcal{B}) - (-\mathcal{D} - \mathcal{B})] \\
&= -\gamma w^D(r_{kl}) \left(\frac{y_k - y_l}{r_{kl}} \right)^2 x_k [\mathcal{B} + \mathcal{B} + \mathcal{B} + \mathcal{B}] \\
&= -\gamma w^D(r_{kl}) \left(\frac{y_k - y_l}{r_{kl}} \right)^2 x_k 4\dot{\gamma}(x_k - x_l) \\
&= -4\gamma\dot{\gamma} w^D(r_{kl}) \left(\frac{y_k - y_l}{r_{kl}} \right)^2 x_k (x_k - x_l) \neq 0
\end{aligned} \tag{B.50}$$

The contribution to the configurational term of the dissipative force is different than zero, therefore the mappings are not sufficient to enforce the condition of $\langle P_{xy}(0) \rangle = 0$. Moreover, it is clear that the sum in Equation (B.50) is proportional to the value of the shear rate $\dot{\gamma}$, supporting the results reported in Figure 4.1.

Appendix C

Velocity field for P40

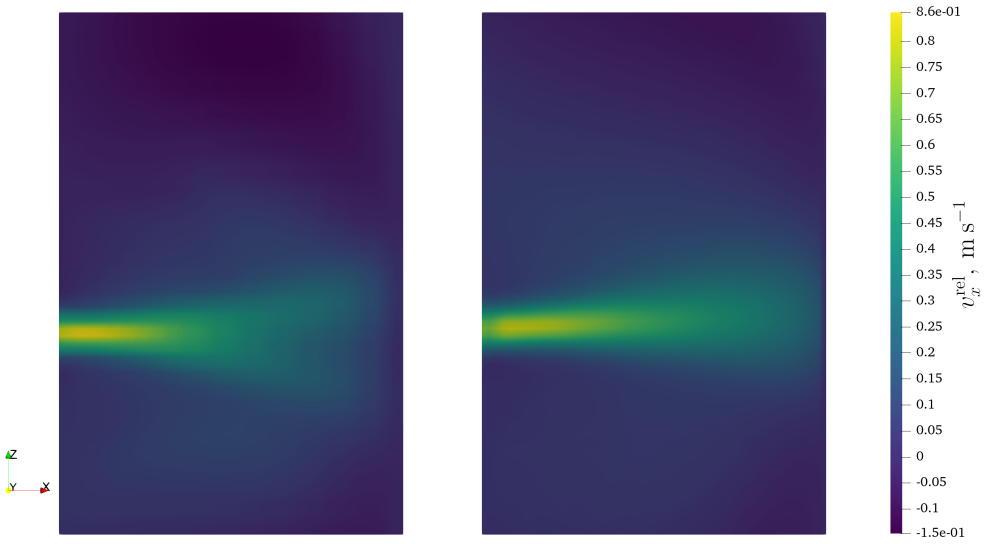

Fig. C.1 Comparison of the radial velocity obtained from CFD (left) and experiments (right) for the P40 blend at Re = 2.81.84.

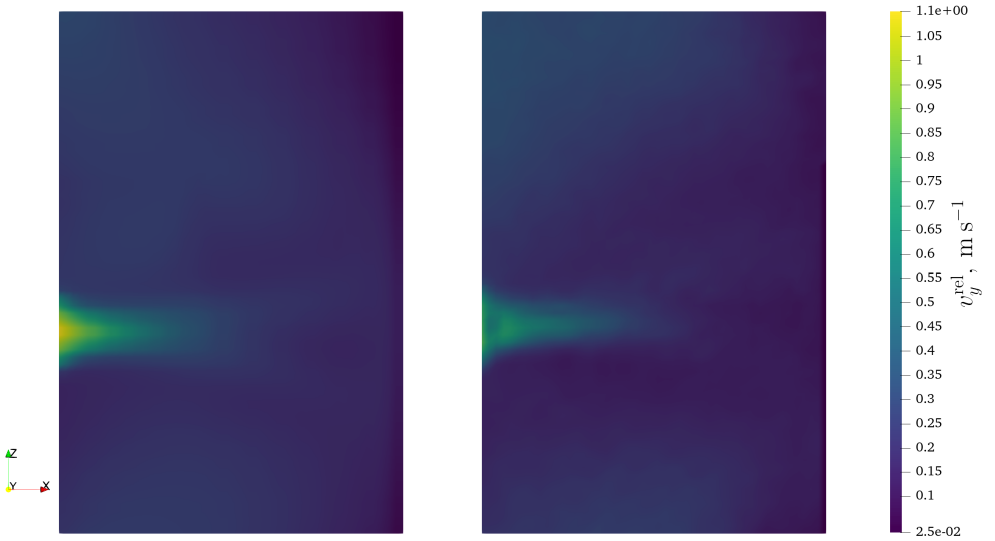

Fig. C.2 Comparison of the tangential velocity obtained from CFD (left) and experiments (right) for the P40 blend at Re = 2.81.84.

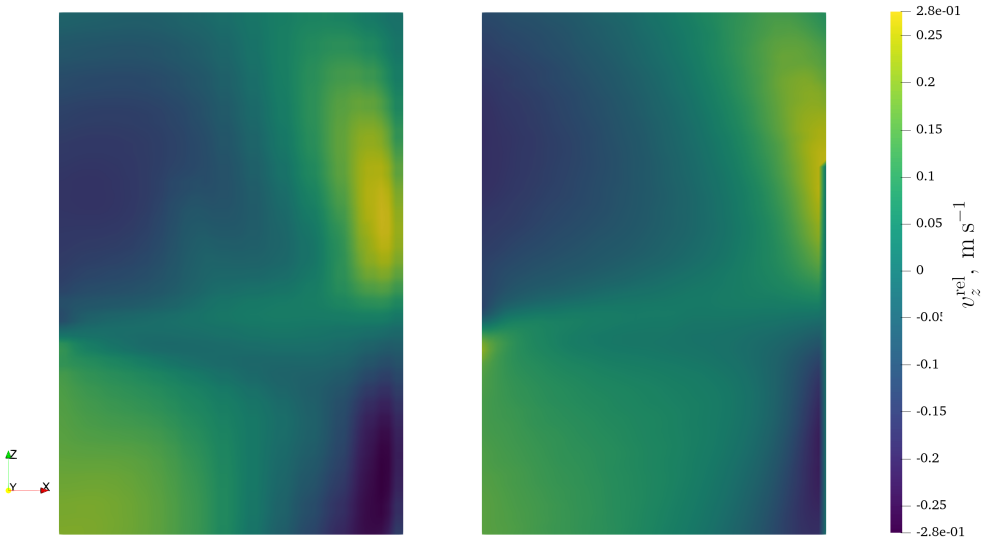

Fig. C.3 Comparison of the axial velocity obtained from CFD (left) and experiments (right) for the P40 blend at Re = 2.81.84.

Appendix D

Identifying simulation length for TTCF calculations

As shown in Figure 4.7a, the standard error of the TTCF method increases in time, so a longer simulation result in lower precision. Under these conditions, the optimal approach would be to set a simulation time exactly equal to the decorrelation time of the stresses in the system studied. Oftentimes, it is not possible to identify an exact value for the decorrelation time, and increasing the simulation length seem the safest option. Once the stress are decorrelated, the integral in Equation (4.4) will give a null contribution, and the value of P_{yx} will remain constant in time. In practice, the value of $\langle P_{yx}(0)P_{yx}(t)\rangle$ oscillates around zero after the decorrelation, resulting in small variations of the shear pressure. This behavior, together with the increase in the TTCF's standard error and computational costs, make undesiderable to use simulations time much longer than the stress decorrelation time.

An optimal choice of the simulation length probably requires some test in non-equilibrium conditions, to evaluate the best approximation of the stress decorrelation time. Such workflow could increase dramatically the computational cost, due to the high number of daughter trajectories required. An alternative approach, used in the present work, consist in evaluating the stress auto-correlation function from an equilibrium simulation to get an initial guess. The results of this procedure for a simple DPD fluid are reported in Figure D.1, which showed a fast decorrelation and allowed the choice of an appropriate simulation time. This time value is shown as a

vertical red line in Figure D.1 and avoided a counterproductively long simulation, even though it cannot be considered an optimal value.

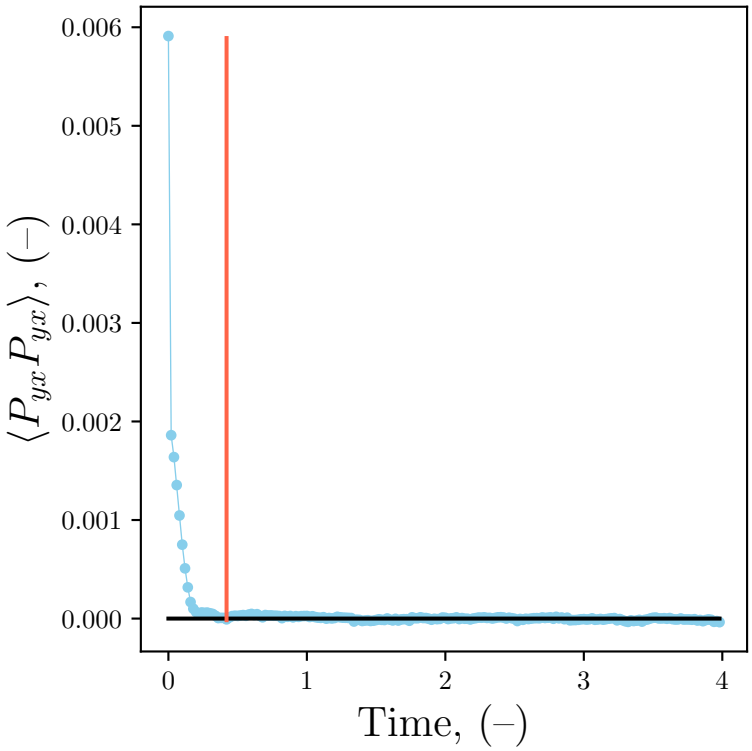

Fig. D.1 Auto-correlation function for the P_{yx} element of the pressure tensor, calculated from an equilibrium DPD simulation. The horizontal black line indicates the value of zero, while the vertical red line identifies the time length of the non-equilibrium simulations performed in this work.

Appendix E

Influence of timestep on DPD simulations

The value of the timestep Δt heavily affect the results of a DPD simulation. The random force $\boldsymbol{F}_{ij}^{R}$ depends explicitly on Δt, as reported in Equation (2.18), differently from many other force fields. In atomistic simulations, usually a smaller Δt allow ot reach a higher accuracy and to capture better the dynamnics of the system. As explained by Groot and Warren (1997), decreasing the timestep increases the variance of the random force, and, consequently, the noise in the simulation. An example of this phenomena is reported in figure Figure E.1, where more noisy and oscillating $P_{yx}(t)$ curves are the result of lower timesteps.

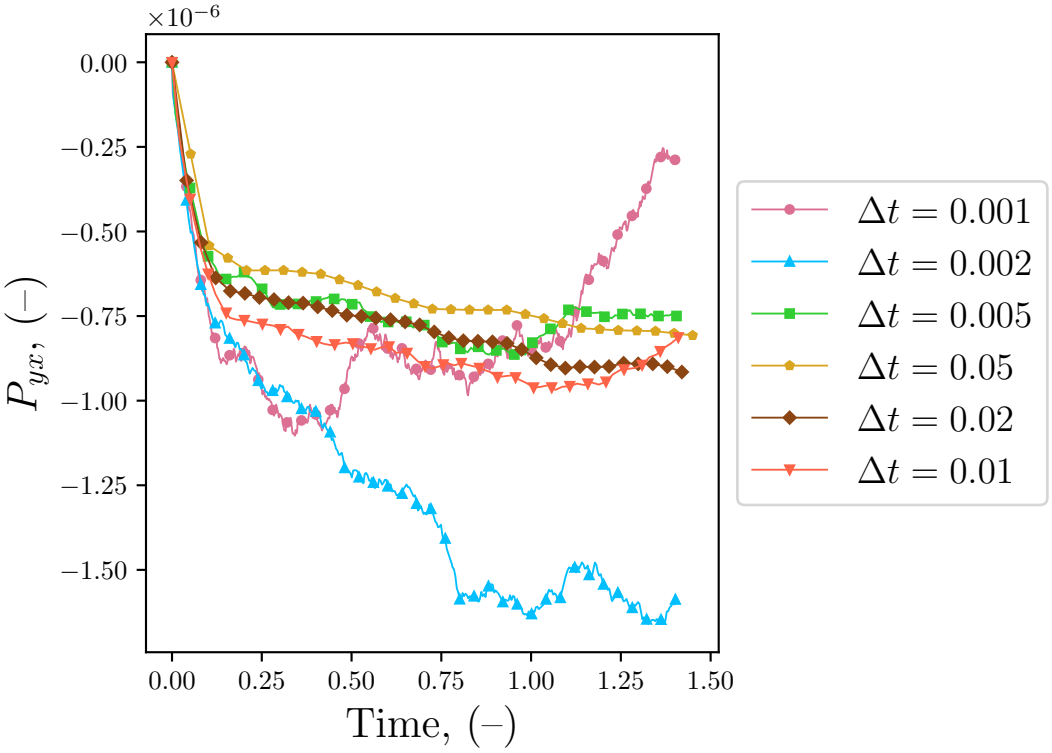

Fig. E.1 Time evolution of the shear pressure P_{yx} for different values of the timestep Δt in DPD simulations. All values are obtained using the TTCF method, with a shear rate of $\dot{\gamma} = 10^{-6}$ and 2×10^5 daughter trajectories.

The results in Figure E.1 helped in the choice of the timestep used in this work, which is equal to 0.01. This is a common value in DPD simulations involving simple fluids and is it the lowest still exhibiting a limited noise, according to the data in the plot.

Appendix F

Discretization schemes for CFD simulations

This appendix reports the numerical setup of the CFD simulations performed in the works described in the thesis.

F.1 SMX static mixer simulation

The governing equations were solved under using the `simpleFoam` solver, since only steady-state simulations were performed. The solver employs the consistent SIMPLE (Semi-Implicit Method for Pressure Linked Equations), or SIMPLEC, pressure–velocity coupling algorithm.

The discretization schemes adopted are summarised below:

- **Gradient scheme:** `Gauss linear` – Gaussian integration with linear interpolation for the computation of gradients.
- **Divergence scheme:** `bounded Gauss linearUpwindV grad(U)` – bounded Gaussian integration with linear upwind interpolation for the momentum equation.
- **Laplacian scheme:** `Gauss linear corrected` – Gaussian integration with linear interpolation and non-orthogonality correction for diffusive terms.

F.2 Stirred tanks simulation

The governing equations were solved under using the `simpleFoam` solver for the steady-state simulations. The solver employs the consistent SIMPLE (Semi-Implicit Method for Pressure Linked Equations), or SIMPLEC, pressure–velocity coupling algorithm.

The discretization schemes adopted are summarised below:

- **Gradient scheme:** `Gauss linear` – Gaussian integration with linear interpolation for the computation of gradients.
- **Divergence scheme:** `bounded Gauss linearUpwindV grad(U)` – bounded Gaussian integration with linear upwind interpolation for the momentum equation.
- **Laplacian scheme:** `Gauss linear corrected` – Gaussian integration with linear interpolation and non-orthogonality correction for diffusive terms.

For the transient simulation including the scalar transport equation, the `pimpleFoam` solver has been modified to read viscosity values from the GPR routine in Python. The solver employs the PISO (Pressure-Implicit with Splitting of Operators) pressure–velocity coupling algorithm.

The following discretization scheme were used for the scalar transport equation:

- **Time scheme:** `backward` – second order implicit backward differencing
- **Gradient scheme:** for the scalar field a limited gradient was adopted (`grad(C) cellLimited Gauss linear 1`) in order to improve boundedness in the presence of steep concentration gradients.
- **Divergence scheme:** for the scalar transport equation, a higher order bounded scheme was employed `div(phi,C): Gauss vanLeer` – Gaussian integration with van Leer flux limiter.